

Hydrodynamic modelling of wave overtopping over a block-covered dike



MSc Thesis

L. Barendse | April 2021

UNIVERSITY OF TWENTE.

hillblock

Hydrodynamic modelling of wave overtopping over a block-covered dike

by

L. Barendse

to obtain the degree of Master of Science

at the University of Twente

to be defended on April 23, 2021

Graduation committee

UNIVERSITY OF TWENTE.

Prof. dr. S.J.M.H. Hulscher

Dr. J.J. Warmink

V.M. van Bergeijk (MSc)

W. Chen (MSc)

hillblock

A. Mughal (MSc)

D. Hill (MA)

Preface

This thesis forms the finishing of my Master of Science in River and Coastal Engineering. This graduation research was carried out at the department of Water Engineering and Management at the University of Twente in combination with Hillblock BV from Rotterdam. I could not have done this without the help and feedback of several people.

Firstly, I want to express my gratitude to my daily supervisors Vera van Bergeijk and Weiqiu Chen for their feedback on the model set-up and critical reflections on the academic writing in this report.

Secondly, I would like to thank Aroen Mughal and Dorian Hill for their input on behalf of Hillblock. Their feedback gave insight into the practical side of the test and the block revetments, which was of great importance for this research. Also I would like to thank Paul van Steeg from Deltares for his input on the physical test at the Delta flume.

Furthermore, I want to thank Jord Warmink and Suzanne Hulscher for their critical view to increase the scientific value and academic level of this research.

Finally, I want to thank my family, friends and fellow students who supported me during my life as a student and during this research.

Luuk Barendse

Abstract

Wave overtopping is one of the main failure mechanisms of a dike. It is defined as the amount of water flowing over the crest of a coastal structure due to wave action. The water that overtops the dike reaches the landward slope of the dike, where it can cause erosion due to high flow velocities and turbulence that causes high stresses on the cover. Therefore, innovative block revetments such as Grassblocks have been developed by Hillblock to protect the subsoil of the dike against erosion and are installed between the grass and subsoil of the dike. The blocks have a permeable function which reduces the flow velocity and pressures along the landward slope.

The performance of these blocks are assessed in physical tests, which provides insights into the stability of the blocks, but are also expensive and have limitations in their measurements due to highly turbulent conditions. Numerical models can provide the flow conditions on any location and the dike geometry and wave conditions can be easily adjusted. Therefore, the goal of this study was to determine the hydrodynamic conditions on the dike cover caused by the wave run-up on the seaward slope and by the overtopping flow over the crest and landward slope.

The geometry and wave conditions from the physical test at the Delta flume of Deltares has been implemented in OpenFOAM, a Reynolds-Averaged Navier-Stokes based Computational Fluid Dynamics software package. Using the solver porousWaveFoam, which is included in the waves2Foam toolbox, a porous layer on the crest and landward slope has been implemented which represents the permeable function of the Grassblocks. The flow resistance F_p of this porous layer largely depends on the resistance coefficients α [-] and β [-]. The model has been run using different combinations of the resistance coefficients based on research by Van Gent (1995) [$\alpha = 1000$, $\beta = 1.1$], Jensen et al. (2014) [$\alpha = 500$, $\beta = 2.0$] and Losada et al. (2008) [$\alpha = 200$, $\beta = 0.8$].

The model has then been calibrated based on these three different sets of resistance coefficients. Comparing the modelled and observed peak pressures and peak flow velocities of every overtopping waves showed that the resistance coefficients as introduced by Jensen et al. (2014) performed best for the peak flow velocities (NSE = 0.315) and peak pressures (NSE = 0.266). The validation also proved that the model works relatively well for the peak flow velocities (NSE = 0.606) and peak pressures (NSE = 0.154).

The validated model then has been used to determine the hydrodynamic conditions on the landward slope. Video analysis of the physical test showed that the Grassblocks collapsed at the toe of the landward slope after 300 s. The hydrodynamic conditions presented that especially the pressure at this specific location was time was highest, which was caused by a large flow thickness and high flow velocity. Eventually the model has been used to determine which block specifications can reduce the hydrodynamic conditions the most. A sensitivity analysis showed that a porosity of $n = 0.6$ and the porous layer thickness of 36 mm reduced the pressure the most.

Contents

Preface	i
Abstract	ii
List of Figures	v
List of Tables	ix
List of Abbreviations	x
List of Symbols	xi
1 Introduction	1
1.1 Context	1
1.2 Problem definition	2
1.3 Objective and research questions	3
1.4 Thesis outline	3
2 Theoretical background	4
2.1 Wave action on a dike	4
2.2 Dike covers	8
2.3 Block revetment stability	10
3 Physical Test Delta Flume	11
3.1 Scaling	11
3.2 Model set-up	12
3.3 Performed measurements	13
3.4 Test program	15
4 Methodology	17
4.1 Coupling of hydrodynamic model	17

4.2	Implementation of block revetments	23
4.3	Hydrodynamic conditions on block revetments	27
5	Results	30
5.1	Coupling of hydrodynamic model	30
5.2	Implementation of block revetments	36
5.3	Hydrodynamic conditions on block revetments	40
6	Discussion	46
6.1	Physical Test Data	46
6.2	Methodology	47
6.3	Performance of the model	48
6.4	Application of the model	49
7	Conclusion	51
8	Recommendations	53
8.1	3D model	53
8.2	Infiltration	53
8.3	Physical testing	53
8.4	Computational Fluid Dynamics course	54
	Bibliography	55
A	Wave characteristics	59
B	Model validation	60
C	Calibration	64
D	Validation	68
E	Specifications of Paddle Wheel	74
F	Specifications of Pressure Sensor	76
G	Dimensions of scaled Grassblock	78
H	Dimensions of scaled Hillblock 2.0	80
I	Specifications of Geotextile	82

List of Figures

1.1	Wave-structure interaction processes (Schüttrumpf and Oumeraci, 2005).	2
2.1	Types of breaking on a slope (Van der Meer et al., 2018).	4
2.2	Wave run-up height on a smooth impermeable slope (Schüttrumpf et al., 2009).	6
2.3	Sawtooth shape of flow thickness (h), flow velocity (u) and specific discharge (q) as a function of time with the overtopping duration T_0	8
2.4	Overview of multiple layers on dike. Adapted from Bezuijen et al. (1987).	9
2.5	Different types of block revetments	10
3.1	Overview of test setup with wave paddle located at $X = 0$ m, water level $h = 6.9$ m and wave height meters located at $X = 108.5, 114.5, 117.5$ m.	12
3.2	Cross section of the test set-up in the Delta Flume adapted from Van Steeg (2017)	12
3.3	Grassblocks installed on crest and inner slope in the Delta flume.	13
3.4	Set-up of measuring equipment. Marked in red the paddle wheel, marked in yellow the pressure sensor.	14
3.5	Pressure sensors as used in the Grassblocks test (Van Steeg, 2017).	15
3.6	Wave overtopping and damage on Grassblocks during tests (Van Steeg, 2017).	16
4.1	Overview of OceanWave3D and OpenFOAM domain.	18
4.2	A section of generated mesh in OpenFOAM.	18
4.3	Generated waves of Test03 in OpenFOAM.	20
4.4	Measuring points P1-P3 on waterside slope of the dike.	21
4.5	Run-up velocity and flow thickness exceeded by 2% of the up-rushing waves calculated using the run-up equations (Eqs. (2.7) and (2.8)). The vertical lines represent the locations of P1, P2 and P3.	22
4.6	Section of the adapted dike geometry, shaded in red is the porosityZone.	25
4.7	Section of the adapted generated mesh on dike geometry in OpenFOAM.	25
4.8	Impression of the occurrence of damage during Test T03, the red dashed circle indicates the location where damage occurred first (Van Steeg, 2017)	27
4.9	Location of occurrence of damage on block revetments (circled in red)	28

5.1	Free surface elevation of incoming waves at $X=108.5$ m from $t = 200 - 250$ s in Test01.	31
5.2	Free surface elevation of incoming waves at $X=108.5$ m from $t = 200 - 250$ s in Test03.	31
5.3	Energy density spectrum of incoming waves at $X=108.5$ m in Test01	32
5.4	Energy density spectrum of incoming waves at $X=108.5$ m in Test03	32
5.5	Modelled flow velocity and flow thickness between $t = 200 - 300$ s and empirical 2% values according to Schüttrumpf and Oumeraci (2005) at P3 in Test03.	33
5.6	Modelled against empirical 2% value of flow thickness $h_{A,2\%}$ and run-up flow velocity $u_{A,2\%}$ on the waterside slope.	34
5.7	Pressure on the dike crest at location of PS1 between $t = 350 - 380$ s in Test01.	35
5.8	Pressure on the dike crest at location of PS1 between $t = 30 - 60$ s in Test03.	35
5.9	Flow velocity at PW1 and pressure at PS3 between $t = 150 - 170$ s in Test03 using resistance coefficients of Van Gent (1995); Jensen et al. (2014); Losada et al. (2008).	37
5.10	Modelled against observed peak flow velocity u and peak pressure P per overtopping wave during $t = 0 - 170$ s in Test03.	38
5.11	Modelled against observed peak flow velocity u and peak pressure P per overtopping wave during $t = 170 - 350$ s in Test03 using $\alpha = 500$ and $\beta = 2.0$	39
5.12	Modelled flow velocity, shear stress, flow thickness and pressure at toe of landward slope ($X = 200.79$ m, $Z = 6.2$ m) using Grassblocks during Test03.	41
5.13	Relative change in peak values of the hydrodynamic conditions [%] against the relative change in porosity n and porous layer thickness [%]. The peak values are based on the moving averaged time series between 290-310 s, as displayed in Figs. 5.14 and 5.15	43
5.14	Modelled flow velocity, shear stress, flow thickness and pressure at toe of landward slope ($X = 200.79$ m, $Z = 6.2$ m) between $t = 290 - 310$ s in Test03 using various values of the porosity n	44
5.15	Modelled flow velocity, shear stress, flow thickness and pressure at toe of landward slope ($X = 200.79$ m, $Z = 6.2$ m) between $t = 290 - 310$ s in Test03 using various porous layer thicknesses.	45
6.1	Observed flow velocity at PW1 (blue) and observed pressure at PS3 (red) between $t = 0 - 500$ s in Test01.	46
6.2	Observed flow velocity at PW1 (blue) and observed pressure at PS3 (red) between $t = 0 - 500$ s in Test02B.	47
6.3	Observed flow velocity at PW2 (blue) and observed pressure at PS5 (red) between $t = 0 - 350$ s in Test03.	49
A.1	Free surface elevation of incoming waves at $X=108.5$ m in Test01.	59
A.2	Free surface elevation of incoming waves at $X=108.5$ m in Test03.	59

B.1	Run-up flow velocity u [m/s] (blue solid line) and 2% run-up flow velocity $v_{A,2\%}$ (red dash-dot line) along the water side slope measured at three locations P1-P3 in Test01.	60
B.2	Run-up flow velocity u [m/s] (blue solid line) and 2% run-up flow velocity $v_{A,2\%}$ (red dash-dot line) along the water side slope measured at three locations P1-P3 in Test03.	61
B.3	Run-up flow thickness h [m] (blue solid line) and 2% run-up flow thickness $h_{A,2\%}$ (red dash-dot line) along the water side slope measured at three locations P1-P3 in Test01.	61
B.4	Run-up flow thickness h [m] (blue solid line) and 2% run-up flow thickness $h_{A,2\%}$ (red dash-dot line) along the water side slope measured at three locations P1-P3 in Test03.	62
B.5	Pressure on the dike crest as function of time at location of PS1 in Test01.	62
B.6	Pressure on the dike crest as function of time at location of PS1 in Test03.	63
C.1	Flow velocity on the landward slope at PW1 in Test03 using resistance coefficients of Van Gent (1995); Jensen et al. (2014); Losada et al. (2008).	64
C.2	Flow velocity on the landward slope at PW2 in Test03 using resistance coefficients of Van Gent (1995); Jensen et al. (2014); Losada et al. (2008).	65
C.3	Pressure on the landward slope at PS2 in Test03 using resistance coefficients of Van Gent (1995); Jensen et al. (2014); Losada et al. (2008).	65
C.4	Pressure on the landward slope at PS3 in Test03 using resistance coefficients of Van Gent (1995); Jensen et al. (2014); Losada et al. (2008).	66
C.5	Pressure on the landward slope at PS4 in Test03 using resistance coefficients of Van Gent (1995); Jensen et al. (2014); Losada et al. (2008).	66
C.6	Pressure on the landward slope at PS5 in Test03 using resistance coefficients of Van Gent (1995); Jensen et al. (2014); Losada et al. (2008).	67
D.1	Flow velocity on the landward slope at PW1 in Test03 using resistance coefficients of Jensen et al. (2014).	68
D.2	Flow velocity on the landward slope at PW2 in Test03 using resistance coefficients of Jensen et al. (2014).	69
D.3	Pressure on the landward slope at PS2 in Test03 using resistance coefficients of Jensen et al. (2014).	69
D.4	Pressure on the landward slope at PS3 in Test03 using resistance coefficients of Jensen et al. (2014).	70
D.5	Pressure on the landward slope at PS4 in Test03 using resistance coefficients of Jensen et al. (2014).	70
D.6	Pressure on the landward slope at PS5 in Test03 using resistance coefficients of Jensen et al. (2014).	71
D.7	Pressure on the landward slope at PS2 in Test01 using resistance coefficients of Jensen et al. (2014).	71

D.8 Pressure on the landward slope at PS3 in Test01 using resistance coefficients of Jensen et al. (2014). 72

D.9 Pressure on the landward slope at PS4 in Test01 using resistance coefficients of Jensen et al. (2014). 72

D.10 Pressure on the landward slope at PS5 in Test01 using resistance coefficients of Jensen et al. (2014). 73

List of Tables

2.1	Classification of mean overtopping discharges (Van der Meer et al., 2018)	7
2.2	Surface roughness factors for typical embankment factors	9
3.1	Location of measuring equipment; Wave Height Meter (WHM), Pressure Sensor (PS) and Paddle Wheel (PW).	13
3.2	The wave characteristics during the four tests	16
4.1	Wavelengths in physical test	18
4.2	Location of measuring points P1 - P3.	21
4.3	Resistance coefficients.	24
4.4	Porosity n used for sensitivity analysis.	29
4.5	Porous layer thicknesses used for sensitivity analysis.	29
5.1	Significant wave height and spectral wave period of physical test and OpenFOAM model for Test01 and 03	30
5.2	Performance indicators of u	38
5.3	Performance indicators of P	38
5.4	Performance indicators of u	39
5.5	Performance indicators of P	39
5.6	Peak flow characteristics for Grassblock in Test03 with the time t , flow velocity u , shear stress τ_s , flow thickness h and pressure P	40
B.1	Run-up velocity $u_{A,2\%}$ and flow thickness $h_{A,2\%}$ exceeded by 2% of the up-rushing waves calculated at three locations using Eqs. (2.7) and (2.8).	60

List of Abbreviations

CFD	Computational Fluid Dynamics
DNS	Direct Numerical Simulation
LES	Large Eddy Simulation
NLSW	Non Linear Shallow Water
NSE	Nash-Sutcliffe Efficiency
OpenFOAM	Open-source Field Operation And Manipulation
PS	Pressure Sensor
PW	Paddle Wheel
RANS	Reynolds-Averaged Navier-Stokes
RMSE	Root Mean Square Error
SPH	Smoothed Particle Hydrodynamics
SST	Shear Stress Transport
VOF	Volume of Fluid
WHM	Wave Height Meter

List of Symbols

α	Linear resistance coefficient	—
α	Outer dike slope	°
β	Non-linear resistance coefficient	—
γ_β	Influence factor for oblique wave attack	—
γ_b	Influence factor for a berm	—
γ_f	Influence factor for the permeability and roughness of or on the slope	—
γ_p	Closure coefficient	—
λ	Scaling factor	—
λ_1	Stress limiter	—
λ_2	Effective potential flow threshold	—
μ_{tot}	Total dynamic viscosity	Pa/s
ν	Kinematic viscosity	m ² /s
ω	Specific rate of dissipation of turbulent kinetic energy	1/s
ρ_w	Density of the fluid	kg/m ³
τ_n	Normal stress	m ² /s ²
τ_s	Shear stress	m ² /s ²
ε	Rate of dissipation of turbulent kinetic energy	m ² /s ³
ξ	Surf similarity parameter	—
a	Resistance coefficient due to linear flow resistance	—
b	Resistance coefficient due to non-linear flow resistance	—
C	Courant number	—
c	Wave celerity	m/s
C_m	Mass coefficient	—

d_{50}	Nominal diameter of the porous material	m
F_p	Flow resistance	—
Fr	Froude number	—
g	Gravitational acceleration	m/s ²
h	Flow thickness	m
h	Water depth	m
H_{m0}	Significant wave height	m
H_{max}	Maximum wave height	m
$h_{A,2\%}$	2%-value of flow thickness at location A on the seaward slope	m
k	Turbulent kinetic energy	m ² /s ²
KC	Keulegan-Carpenter number	—
L	Wave length	m
L_0	Deep water wave length	m
m_n	n^{th} moment of spectral density	m ² /s ⁿ
N	Amount of waves	—
n	Porosity	—
p	Pressure	kPa
p_0	Total pressure	kPa
p_d	Hydrodynamic pressure	kPa
p_s	Hydrostatic pressure	kPa
q	Average wave overtopping discharge	m ² /s
R_c	Free crest height above still water line	m
$R_{u2\%}$	Run-up level exceeded by 2% of incident waves	m
Re_p	Reynolds number in porous media	—
s	Wave steepness	—
T	Wave period	s
t	Time	s
T_m	Average wave period	s
T_p	Peak wave period	s

$T_{m-1,0}$	Spectral wave period	s
u	Flow velocity	m/s
u_p	Pore velocity	m/s
$v_{A,2\%}$	2%-value of run-up velocity at location A on the seaward slope	m/s
X	Horizontal position	m
Z	Vertical position	m
z_A	Location on the seaward slope, measured vertically from SWL	m

1 | Introduction

1.1 Context

Dikes can fail due to different failure mechanisms. One of the main failure mechanisms is wave overtopping (Van der Meer et al., 2018). During storm surges, the waves can overtop over the dikes (Fig. 1.1). This process can be divided in three phases; wave impact, wave run-up and wave overtopping. The water that overtops the dike reaches the landward slope of the dike, where it can cause erosion due to high flow velocities and turbulence that causes high stresses on the cover. Erosion of earthen spillways occurs if the maximum overtopping flow velocity exceeds the critical flow velocity of the dike (Van Bergeijk et al., 2019).

Innovative covers have been developed to strengthen the earthen dike cover against the erosion caused by overtopping waves. Hillblock BV, a company from Rotterdam, has developed several types of innovative blocks. One of their blocks is called the Grassblock, which is placed underneath the grass cover of the dike. When the grass cover erodes during extreme storm events, the Grassblocks will still protect the clay cover of the dike against overtopping waves. To assess the performance of these blocks, physical overtopping tests have been performed in the Delta flume of Deltares (Van Steeg, 2017). These physical tests provide insights into the stability of the blocks, but are also expensive. Furthermore, due to the highly turbulent conditions, it is difficult to measure the flow conditions and the number of measuring locations is limited.

Numerical models can provide the flow characteristics, such as flow velocity, pressure, shear stress and flow thickness on any location, which can provide more insight into the flow conditions and the limits of the dike cover. Hydrodynamic models are developed to get insight into the forces that occur on a dike due to wave overtopping. These models can be divided in three types. The first type are Smoothed Particle Hydrodynamics (SPH) models, which do not require complex meshes but are very computationally expensive (Altomare et al., 2015; Khayyer et al., 2018). The second type are Non Linear Shallow Water (NLSW) models, which are based on simplified Navier-Stokes equations (Hu et al., 2000) and are computationally efficient and practically flexible. However, the detailed structure of the wave breaking is ignored in the NLSW models. The third type of hydrodynamic models are Reynolds-Averaged Navier-Stokes (RANS) models, which are more accurate than NLSW models and more computationally efficient than SPH models. Because of these reasons a RANS based model called OpenFOAM is applied in this study. OpenFOAM is open-source and is becoming increasingly popular in the coastal engineering field. Previous research (Jacobsen et al., 2012; Van Bergeijk et al., 2020; Chen et al., 2020a,b) has shown the capability of OpenFOAM in simulating wave overtopping. Most studies on wave overtopping in OpenFOAM are focused on the waterside slope (Jacobsen et al., 2015; Losada et al., 2008; Gruwez et al., 2020) or the crest (Jacobsen et al., 2018).

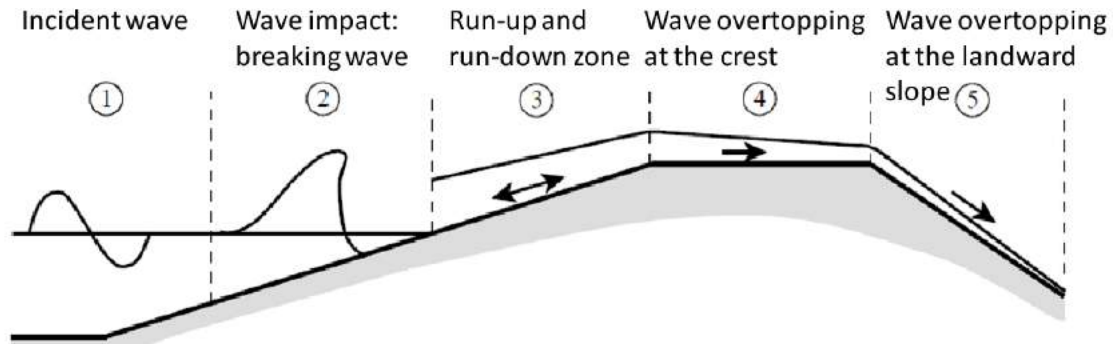


Figure 1.1: Wave-structure interaction processes (Schüttrumpf and Oumeraci, 2005).

1.2 Problem definition

Dike cover erosion due to wave loads by overtopping waves could eventually lead to dike breaching, which can result in severe losses of properties and lives. Therefore, accurate estimations of these wave loads are important for dike safety assessment. There are two ways to get accurate estimations of the hydraulic loads, by physical model testing or numerical modelling.

Experiments (Klein Breteler, 2016; Klein Breteler et al., 2018) have shown that erosion on dikes is mainly caused by wave loads such as pressure, normal stress, shear stress and flow velocities. However, it is difficult to measure these wave loads in the physical tests. Furthermore, the prototype tests are expensive and it takes weeks to prepare for physical models. Additionally, it is hard to change the dike configurations in the physical tests. Therefore, hydrodynamic models have been developed to assess wave run-up and/or wave overtopping on hydraulic structures. These include SPH models of the wave impact on breakwaters (Altomare et al., 2015; Khayyer et al., 2018) and NSW models of wave overtopping on coastal structures (Hu et al., 2000). However, these models mostly focused on hard structures such as breakwaters and seawalls.

To gain a better understanding of the wave overtopping flow and the erosion due to wave overtopping, two PhD researchers in the Water Engineering and Management group of the University of Twente have both developed a model in OpenFOAM for the overtopping flow. Chen et al. (2021) simulated small scale overtopping tests to determine the average overtopping discharge for different configurations of the waterside slope. This model includes wave generation at the boundary and wave overtopping over different roughness elements. The model of Van Bergeijk et al. (2020) simulated the flow over the dike crest and landward slope and can be used to determine the hydrodynamic loads along the crest and landward slope of grass-covered dikes. However, a hydrodynamic numerical model that can simulate the hydrodynamic conditions due to wave overtopping over the waterside slope, block covered crest and landward slope does not exist yet. This model can provide the flow conditions on any location on the dike cover and can give insight into the hydrodynamic flow conditions that cause the permeable block revetments to collapse.

1.3 Objective and research questions

The objective of this study is

To determine the hydrodynamic conditions on the dike cover caused by the wave run-up on the waterside slope and by the overtopping flow over the crest and landward slope.

This can be done using a hydrodynamic model in OpenFOAM that determines the hydrodynamic flow conditions on the cover along the entire dike profile. Subsequently, a method should be found to include innovative covers in this hydrodynamic model. Using data of large scale flume tests for calibration and validation finally leads to a model that is able to determine the hydrodynamic conditions on innovative covers along the entire dike profile. This model can then be applied to determine which hydrodynamic loads caused the dike cover blocks to fail and which block revetment properties can reduce these hydrodynamic loads the most.

Several research questions have to be answered to meet this objective;

1. How can the wave overtopping over the seaward slope, crest and landward slope be coupled into one hydrodynamic model?
2. To what extent can a 2D vertical hydrodynamic model simulate the flow over a 3D block cover?
3. What are the hydrodynamic conditions leading to failure of the block revetments?

1.4 Thesis outline

First the theoretical background is explained in Chapter 2. Subsequently the physical test that this research is based on is described in Chapter 3. Then the methodology for this project is described in Chapter 4, where each section consists of the methodology that has been used to answer a research question. In Section 4.1 the coupling of the hydrodynamic model is explained, Section 4.2 describes the implementation of the block revetments and Section 4.3 describes the methodology to determine the hydrodynamic conditions that led to the failure of the block revetments. Furthermore, the effect of the porosity and porous layer thickness on the hydrodynamic conditions have been determined. The results that follow from this methodology are displayed in Chapter 5, where Section 5.1, 5.2 and 5.3 each correspond to the results of the sections from the Methodology. The test data, methodology, performance and application of the model are discussed in Chapter 6, followed by the conclusion in Chapter 7 and the recommendations in Chapter 8.

2 | Theoretical background

2.1 Wave action on a dike

Wave impact

When waves reach the dike, they will often break onto the outer slope, which causes an impact on the outer slope. The location on the outer slope where the waves impact is called the impact zone. The breaking of waves on dikes is determined by the orbital velocity (u_b) and the wave celerity (c). When the orbital velocity exceeds the wave celerity, the wave breaks.

The type of wave breaking depends on the outer slope (α) and on the wave steepness (H/L_0) and is estimated by using the surf similarity parameter, also called the Iribarren number (Eq. (2.1)) (Stanczak et al., 2009). Breaking waves can be distinguished in four types (Fig. 2.1). A rule of thumb is that for $\xi < 2$ waves are considered to be breaking and for $\xi > 2$ they are not breaking. Surging waves are non-breaking waves, whereas plunging waves are waves with steep and overhanging fronts. Collapsing waves are a transition between plunging and surging waves.

$$\xi = \frac{\tan \alpha}{\sqrt{\frac{H}{L_0}}} \text{ with } L_0 = \frac{gT^2}{2\pi} \quad (2.1)$$

The forces caused by the wave impact are generally described by the impact pressure, $p_{2\%}$, which describes the impact pressure that is exceeded by 2% of the waves or p_{max} , which describes the maximum impact pressure. The maximum pressure is considered as the most relevant parameter with respect to the erosion on the waterside slope of grass dikes (Van Steeg et al., 2014).

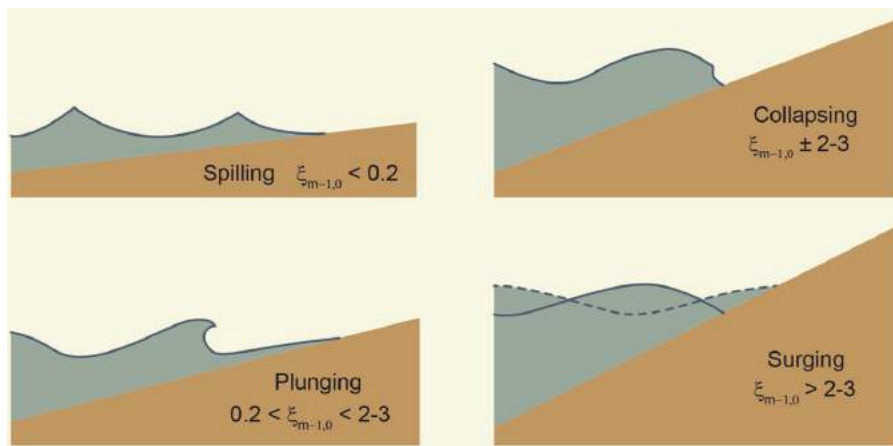


Figure 2.1: Types of breaking on a slope (Van der Meer et al., 2018).

Wave run-up

After the wave impact, the horizontal forces of the wave lead to wave run-up. Wave run-up is defined as the maximum vertical extent of wave uprush on a beach or structure above the still water level (SWL). The wave run-up level exceeded by 2% of incident waves is calculated according to Van der Meer et al. (2018) with Eqs. (2.2a) and (2.2b). Fig. 2.2 shows a graphical explanation of the different parameters used, i.a. $R_{u2\%}$ and H_{m0} . The freeboard R_C is the vertical distance between the Still Water Level and the crest height.

$$\frac{R_{u2\%}}{H_{m0}} = 1.65 \cdot \gamma_b \cdot \gamma_f \cdot \gamma_\beta \cdot \xi_{m-1,0} \quad (2.2a)$$

with a maximum of;

$$\frac{R_{u2\%}}{H_{m0}} = 1.0 \cdot \gamma_f \cdot \gamma_\beta \left(4 - \frac{1.5}{\sqrt{\gamma_b \cdot \xi_{m-1,0}}} \right) \quad (2.2b)$$

$R_{u2\%}$ = run-up level exceeded by 2% of incident waves [m]

H_{m0} = estimate of significant wave height from spectral analysis [m]

$\xi_{m-1,0}$ = breaker parameter [-]

γ_b = influence factor for a berm [-]

γ_f = influence factor for the permeability and roughness of or on the slope [-]

γ_β = influence factor for oblique wave attack [-]

Furthermore, Van Gent (2001) derived his own equations, where Eq. (2.3) is used for plunging waves and Eq. (2.4) for surging waves. Based on physical model tests, he derived optimal values for the parameters $c_0 = 1.35$ and $c_1 = 4.0$, which leads to $c_2 = 2.963$ and $p = 1.482$ (Schüttrumpf and Van Gent, 2003). In these equations the reduction factor γ takes the effects of roughness into account.

$$\frac{R_{u2\%}}{\gamma H_{m0}} = c_0 \cdot \xi_{m-1,0} \quad \text{for} \quad \xi_{m-1,0} \leq p \quad (2.3)$$

$$\frac{R_{u2\%}}{\gamma H_{m0}} = c_1 - \frac{c_2}{\xi_{m-1,0}} \quad \text{for} \quad \xi_{m-1,0} \geq p \quad (2.4)$$

$$c_2 = 0.25 \frac{c_1^2}{c_0}; \quad p = 0.5 \frac{c_1}{c_0}$$

The formulas in Van der Meer et al. (2018) are based on Schüttrumpf and Van Gent (2003) and wave basin tests by Lorke et al. (2012) and include the flow velocity (Eq. (2.5)) and flow thickness (Eq. (2.6)). From wave overtopping tests (Van der Meer et al., 2018) it is known that the run-up velocity is the governing parameter in initiating damage to a grassed slope.

$$v_{A,2\%} = c_{v2\%} \cdot \sqrt{g(R_{u2\%} - z_A)} \quad (2.5)$$

$$h_{A,2\%} = c_{h2\%} \cdot (R_{u2\%} - z_A) \quad (2.6)$$

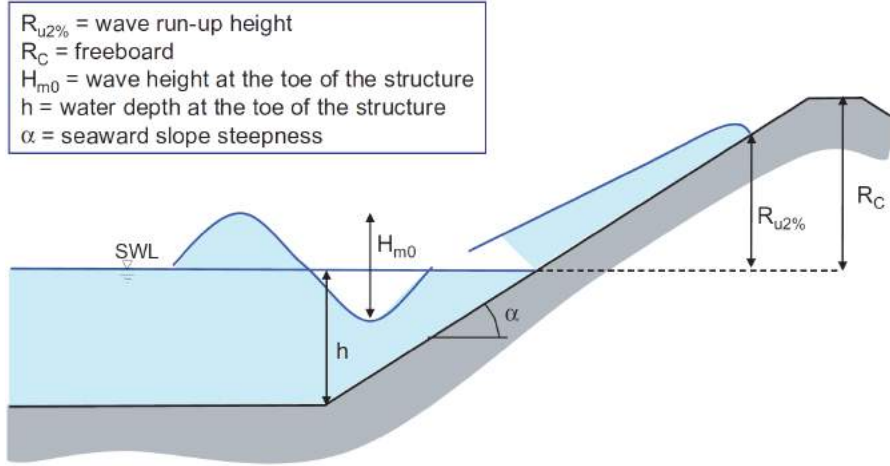


Figure 2.2: Wave run-up height on a smooth impermeable slope (Schüttrumpf et al., 2009).

Schüttrumpf and Oumeraci (2005) derived Eqs. (2.7) and (2.8) for the 2%-exceedance flow velocity and flow thickness based on small scale model tests.

$$\frac{v_{A,2\%}}{\sqrt{gH_{m0}}} = c_{A,u} \cdot \sqrt{\frac{R_{u2\%} - z_A}{H_{m0}}} \quad (2.7)$$

$$\frac{h_{A,2\%}}{H_{m0}} = c_{A,h} \cdot \left(\frac{R_{u2\%} - z_A}{H_{m0}} \right) \quad (2.8)$$

- g = acceleration due to gravity [m/s²]
- z_A = location on the seaward slope, measured vertically from SWL [m]
- c = empirical coefficients [-]
- $c_{v2\%}$ = 1.4-1.5 (for slopes between 1:3 and 1:6)
- $c_{h2\%}$ = 0.20 (for slopes between 1:3 and 1:4)
- $c_{A,u}$ = 1.37
- $c_{A,h}$ = 0.33

Wave overtopping

Wave overtopping is defined as the amount of water flowing over the crest of a coastal structure (such as a seawall, a dike or a breakwater) due to wave action. It occurs when the wave run-up height exceeds the crest height. Overtopping of coastal structures and inundation of coastal regions by waves is a constant hazard and the effects can be disastrous. A number of circumstances can contribute to such an event, including a high tide, a storm surge, large waves (due to swell or wind) or a tsunami, as well as the failure of some form of sea defence (Hubbard and Dodd, 2002).

There are two different approaches to measure and assess wave overtopping. The first approach uses the individual volume of each overtopping wave, also called V in l or m³. The second approach is the most commonly used approach, which uses the mean discharge q over a certain time interval and over a certain section of the structure. This is generally averaged over 1000 waves and is expressed in l/s/m or m³/s/m. Because wave action is an irregular

process, it is difficult to predict the average wave overtopping discharges at structures. However, empirical formulae can be utilized to provide an approximation of the wave overtopping discharge (Geeraerts et al., 2007). The average overtopping discharge can be calculated using the empirical formulae of Van der Meer et al. (2018) based on several overtopping studies in Europe (Eqs. (2.9a) and (2.9b)).

$$\frac{q}{\sqrt{g \cdot H_{m0}^3}} = \frac{0.023}{\sqrt{\tan \alpha}} \gamma_b \cdot \xi_{m-1,0} \cdot \exp \left[- \left(2.7 \frac{R_c}{\xi_{m-1,0} \cdot H_{m0} \cdot \gamma_b \cdot \gamma_f \cdot \gamma_\beta \cdot \gamma_v} \right)^{1.3} \right] \quad (2.9a)$$

with a maximum of

$$\frac{q}{\sqrt{g \cdot H_{m0}^3}} = 0.09 \cdot \exp \left[- \left(1.5 \frac{R_c}{H_{m0} \cdot \gamma_f \cdot \gamma_\beta \cdot \gamma^*} \right)^{1.3} \right] \quad (2.9b)$$

- q = average wave overtopping discharge [m³/s/m]
- g = acceleration due to gravity [m/s²]
- H_{m0} = significant wave height at toe of dike [m]
- ξ_0 = breaker parameter [-]
- $\tan \alpha$ = slope of waterside slope [-]
- R_c = free crest height above still water line [m]
- γ = influence factors of berm, roughness elements, angle of wave attack, vertical wall

In case of large overtopping discharges, the dike cover can erode. Therefore the overtopping discharge should be limited according to Table 2.1 or the dike cover should be protected by a hard revetment.

Table 2.1: Classification of mean overtopping discharges (Van der Meer et al., 2018)

q [l/s/m]	Classification
<0.1	Insignificant with respect to strength of crest and rear of a structure.
1	On crest and landward slopes bad grass covers or clay may start to erode.
10	Significant overtopping for dikes, embankments.
100	Crest and inner slopes of dikes have to be protected by asphalt or concrete.

The wave overtopping flow is characterized by three physical quantities; the overtopping flow velocity u [m/s], the flow thickness h [m] and the specific discharge q [m³/s/m]. Fig. 2.3 shows that these quantities all follow the same shape pattern of a sawtooth shape, where the maximum flow thickness, maximum flow velocity and maximum specific discharge all occur approximately at the same time (Van Bergeijk et al., 2019).

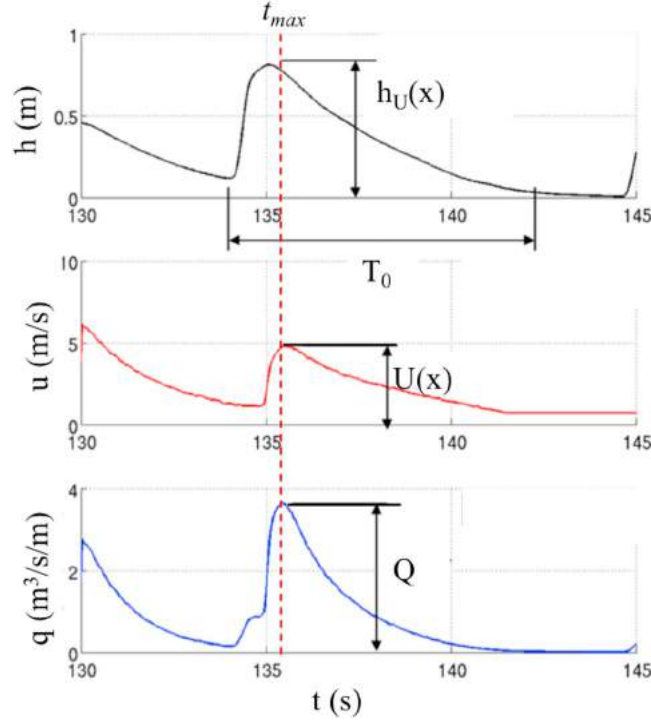


Figure 2.3: Sawtooth shape of flow thickness (h), flow velocity (u) and specific discharge (q) as a function of time with the overtopping duration T_0 . The maximum flow velocity $U(x)$ occurs at time $t = t_{max}(x)$ simultaneously with the momentary flow thickness $h_U(x)$ and the momentary discharge Q (Van Bergeijk et al., 2019).

When the hydraulic load of the cover layer exceeds the strength of the cover, it will erode. These high hydraulic loads can be caused by three processes; (1) high flow velocities at the wave front, (2) wave impact at geometric changes and (3) turbulence that leads to high stresses on the cover (Van Bergeijk et al., 2020). Therefore, the most relevant parameters for wave overtopping are flow velocity u [m/s], flow thickness h [m], pressure p [kPa], shear stress τ_s [m^2/s^2] and normal stress τ_n [m^2/s^2].

2.2 Dike covers

The cover on the water side slope consists typically of grass, asphalt, concrete or natural block revetments. Van der Meer et al. (2018) have shown that roughness has significant influence on the wave overtopping and therefore on the required crest height. By adding blocks or ribs on the smooth surface of the seaward side, the roughness can be artificially increased. Therefore, in the past twenty years, a lot of research (Van der Meer, 2002; Capel, 2015; Chen et al., 2020a) has been done on the effect of block shapes on the roughness, as well as the permeability. The effect of the roughness on the overtopping discharge can be described as γ_f , the influence factor for roughness elements on a slope (Table 2.2).

Table 2.2: Surface roughness factors for typical embankment factors

Reference type	γ_f
Concrete	1.0
Asphalt	1.0
Closed concrete blocks	1.0
Grass	1.0
Basalton	0.9
Placed revetment blocks	0.9

These roughness factors have been determined based on physical tests. Due to scaling effects, it is preferable to have the scale of the physical test closest to the prototype scale (Van der Meer et al., 2018). A filter layer is generally applied between the revetment blocks and the dike (Fig. 2.4). This prevents the loss of embankment soil from the dike body under the impact of waves and seepage flows. Furthermore the filter layer reduces the generation of uplift pressures in the foundation soil layer. The filter layers can be divided in granular filter layers and geotextile filter layers.

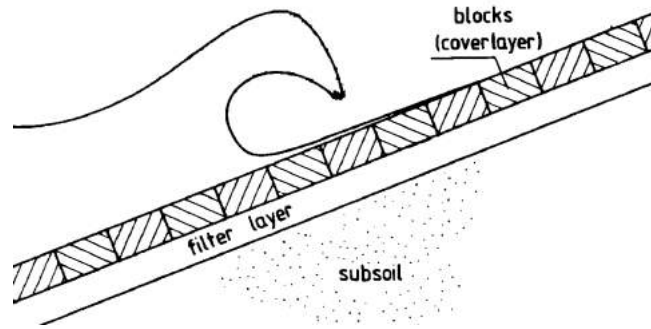


Figure 2.4: Overview of multiple layers on dike. Adapted from Bezuijen et al. (1987).

Innovative block revetments such as the Grassblock (Fig. 3.3b) are placed underneath the grass cover of the dike. When the grass cover erodes during extreme storm events, the Grassblocks will still protect the clay cover of the dike against erosion caused by overtopping waves. A new development of porosity based revetment systems like the Hillblock 2.0 (Fig. 2.5b), uses an open volume between the blocks to absorb the up- and down-rushing water and dissipate the wave energy. This open volume per square meter defines the porosity of the system and is characterised as $d_{channel}$. A lower roughness factor γ_f leads to less wave run-up and wave overtopping.



(a) Grassblock (Van Steeg, 2017)



(b) Hillblock 2.0 (Van Steeg, 2016)

Figure 2.5: Different types of block revetments

2.3 Block revetment stability

According to Klein Breteler et al. (2018), the stability of block revetments is governed by the hydraulic load, the weight of the blocks, and the interaction between the blocks. The hydraulic load on block revetments is caused by the shear forces on the cover layer as the result of wave run-up and run-down on the revetment surface. Furthermore, the hydraulic load is influenced by the dynamic pressure forces caused by wave impact. Additionally, pressure forces on the cover layer caused by the difference between the pore pressures in the filter layer and the wave pressures on the revetment cause a hydraulic load. This pressure difference depends on the wave conditions and the permeability of the dike (Bezuijen et al., 1987). The hydraulic stability of a revetment also depends on the critical shear stress τ_{cr} [N/m²] and the critical velocity U_{cr} [m/s] (CIRIA; CUR; CETMEF, 2007).

According to Klein Breteler et al. (2018), the filter layer underneath the cover layer functions as a damping layer of the pressure distribution caused by the wave impact. The pressure transmission through this filter layer is governed by the leakage length Λ , as displayed in Eq. (2.10).

$$\Lambda = \sqrt{\frac{nDb}{n'}} \quad (2.10)$$

Here n and n' are the permeability of respectively the filter layer and the top layer [m/s]. The parameters b and D represent the thickness of respectively the filter layer and top layer [m]. A calculation tool called 'Steentoets' has been developed for the design of new block revetments and the assessment of the stability of existing block revetments. This calculation tool is based on the leakage length theory. It also assesses the characteristic pressure distribution on the slope and the permeability of the cover and filter layer. The stability is then assessed by comparing the uplift pressure with the weight of the block and the interaction of the blocks. The interaction of the blocks is the most difficult to predict. In physical tests this is mostly done by determining the significant wave height at which damage to the revetment occurs (Klein Breteler et al., 2018). The stability parameter is then quantified using $SF = H_{max}/\Delta D$, where SF is the stability factor [-], H_{max} the largest significant wave height at which no damage occurs [m], Δ the relative density [-] and D the thickness of block [m].

3 | Physical Test Delta Flume

Physical models are a reliable method to measure the wave overtopping discharges over a certain coastal structure. These models are typically scaled, varying from 1:2 up to 1:50. The physical models can represent the coastal structure in 2D (wave flume) or 3D (wave basin) (Van der Meer et al., 2018). Van Steeg (2017) performed flume tests on a scale of 1:2 to determine the stability of Grassblocks on the crest and inner slope. These tests have been performed in the Delta flume of Deltares, which has a length of 291 m, a width of 5.0 m and a height of 9.5 m.

3.1 Scaling

The Delta flume has a wave generator that can generate regular and irregular waves. Furthermore, the wave generator has a system that prevents wave reflection and can generate irregular waves with a significant wave height up to $H_s \approx 2.0$ m depending on the water depth and wave period (Van Gent, 2014). However, along the Dutch coast the waves are significantly higher (De Winter et al., 2012). Therefore, the experiments are scaled with a factor 2. Using this scale, the test can simulate waves with a maximum significant wave height of $H_s \approx 4.0$ m in reality (Van Steeg, 2017). Froude scaling is generally applied for hydraulic structures that involve processes in which inertia and gravity play a dominant role (Pfister and Chanson, 2014). The Froude number Fr is calculated using Eq. (3.1).

$$Fr^2 = \frac{u^2}{gL} \quad (3.1)$$

u = velocity [m/s]

g = gravitational constant [m/s²]

L = length [m]

From the length scale $\lambda = L_F/L_M = 2$, the following relation can be derived using Eq. (3.1), where Fr_M (model) is set equal to Fr_F (full scale).

$$\frac{u_M}{\sqrt{gL_M}} = \frac{u_F}{\sqrt{gL_F}} \Rightarrow u_F = u_M \sqrt{\frac{L_F}{L_M}} = u_M \sqrt{\lambda} \quad (3.2)$$

From the physical units of time [s], wave height [m] and overtopping discharge [m²/s], the following scaling relations can be derived;

$$\begin{aligned}
\text{Time scale} &= \sqrt{\lambda} = \sqrt{2} \\
\text{Wave height scale} &= \lambda = 2 \\
\text{Overtopping discharge scale} &= \lambda^{3/2} = 2\sqrt{2}
\end{aligned}$$

3.2 Model set-up

The test set-up is graphically displayed in Fig. 3.1. This shows the location of the wave generator paddle, the dike, the wave height meters and the sensors. The toe of the dike structure is located at $X = 164.19$ m. A schematic section view is displayed in Fig. 3.2. The first section of the dike consists of concrete, followed by a section of Grassblocks (see Fig. 3.3) which starts at $X = 190.29$ m at a height of $Z = 8.95$ m on the outer slope covering the crest until the inner slope at $X = 201.79$ m at a height of $Z = 6.20$ m. The Grassblocks have been installed on a layer of geotextile with a clay layer of 0.4 m underneath (Van Steeg, 2017).

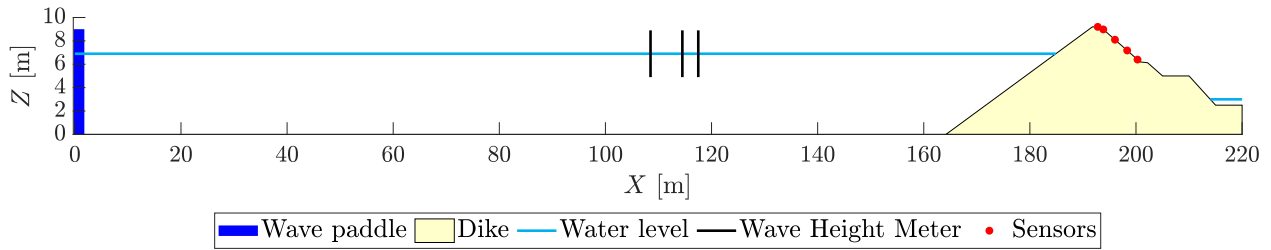


Figure 3.1: Overview of test setup with wave paddle located at $X = 0$ m, water level $h = 6.9$ m and wave height meters located at $X = 108.5, 114.5, 117.5$ m.

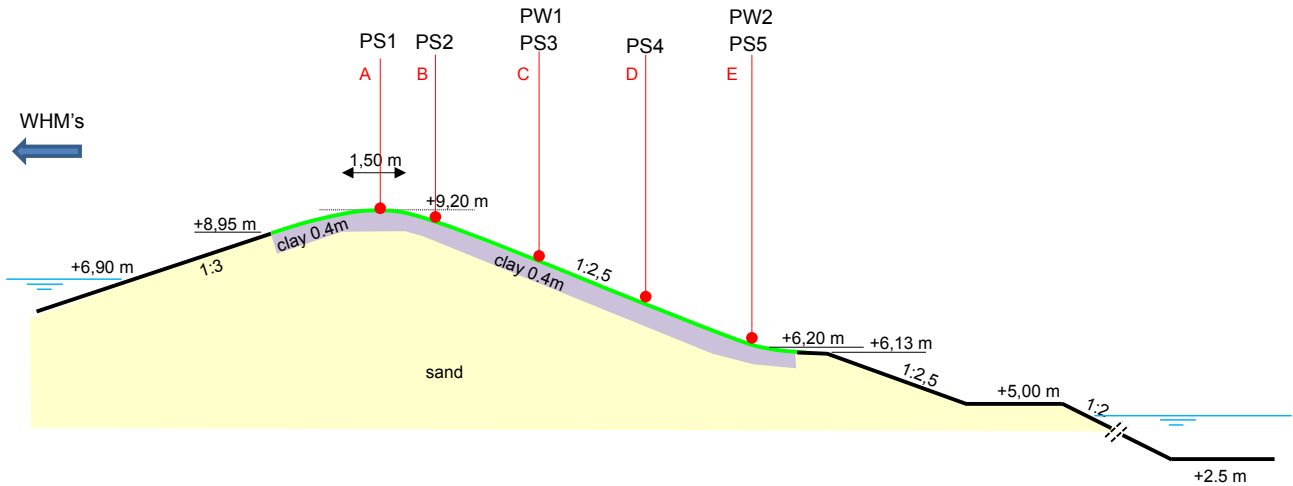


Figure 3.2: Cross section of the test set-up in the Delta Flume adapted from Van Steeg (2017). Exact locations of Wave Height Meter (WHM), Pressure Sensor (PS) and Paddle Wheel (PW) are displayed in Table 3.1.

Table 3.1: Location of measuring equipment; Wave Height Meter (WHM), Pressure Sensor (PS) and Paddle Wheel (PW).

Equipment	X-location [m]	Z-Location [m]
WHM1	108.50	6.90
WHM2	114.50	6.90
WHM3	117.50	6.90
PS1	192.79	9.20
PS2	193.84	8.98
PS3	196.04	8.10
PW1	196.04	8.10
PS4	198.34	7.18
PS5	200.29	6.40
PW2	200.29	6.40



(a) Grassblocks on crest and inner slope (Van Steeg, 2017).

(b) Grassblock (Van Steeg, 2017).

Figure 3.3: Grassblocks installed on crest and inner slope in the Delta flume.

3.3 Performed measurements

Fig. 3.2 shows the measuring equipment used in the physical overtopping test. During the test, the following variables were measured;

- Free surface elevation

The waves have been measured with three wave height meters located at respectively 108.5 m, 114.5 m and 117.5 m from the wave generator. The incoming and reflected waves have been separated based on the method of Mansard and Funke (1980) using the measurements of the wave height meters. The wave conditions during the test can be determined using this method.

- Velocity

The flow velocity has been measured with a Paddle Wheel (PW), as displayed in Fig. 3.4. The paddle wheel type is FLS F3.00.P.01 (Appendix E). The specifications show that these

flow sensors have a flow rate range of 0.15 to 8 m/s. Two paddle wheels have been installed on the landside slope of the dike. This gives the flow velocity with a frequency of 100 Hz. The center of the paddle wheel is located at 27 mm above the top of the Grassblocks. Their location on the dike is displayed in Table 3.1 and Fig. 3.2.

- Pressure

The pressure is measured with Pressure Sensors (PS). These sensors give the pressure with a frequency of 100 Hz. The pressure sensor type is Kulite HKM-375 (Appendix F). Images of the pressure sensors are displayed in Fig. 3.5 and their location on the dike is displayed in Table 3.1 and Fig. 3.2. The only purpose of Pressure Sensor 1 (Fig. 3.5a) is to observe whether there is water on the crest of the dike or not. Therefore, the pressures as measured by PS1 are not used, whereas the pressures measured by PS2, PS3, PS4 and PS5 are used. The pressure at PS2 - PS5 (Fig. 3.5b) is measured at 8 mm above the top of the Grassblocks. PS1 has been installed at 7.5 cm from the wall of the flume. PS2 - PS5 have been installed at 30 cm from the wall of the flume.

- Wave overtopping discharge

The wave overtopping discharge has been determined by measuring the change of volume at the end of the outer slope of the dike. The average wave overtopping discharge can then be determined by dividing the total change of volume at the end of the outer slope of the dike with the total time of the test.

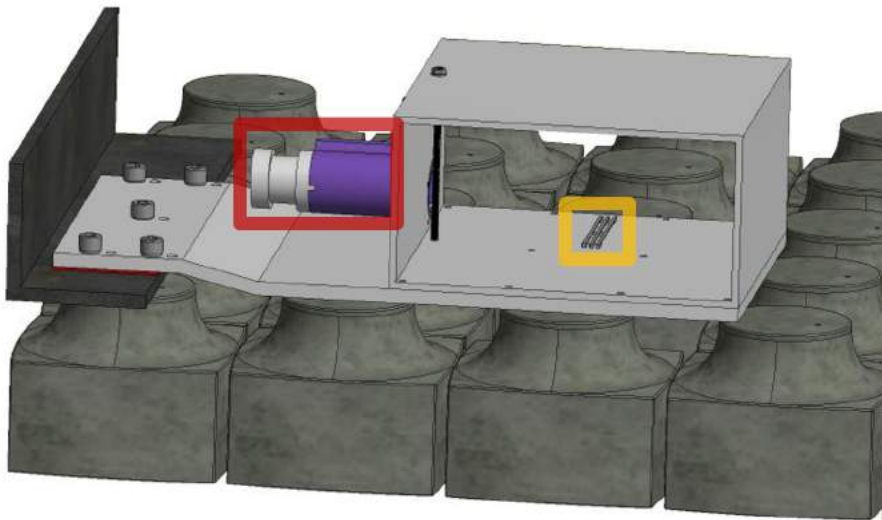


Figure 3.4: Set-up of measuring equipment. Marked in red the paddle wheel, marked in yellow the pressure sensor.



(a) Pressure sensor 1 located on the crest.

(b) Pressure sensors 2 - 5 located on inner slope.

Figure 3.5: Pressure sensors as used in the Grassblocks test (Van Steeg, 2017).

3.4 Test program

The test program consisted of four different tests in which the wave overtopping is increased with each test. This has been done by increasing the wave height or reducing the wave steepness. During the tests, water is lost from the flume due to wave overtopping. Therefore water is being pumped from the Delta flume reservoir into the Delta flume to keep the water level in the Delta flume on a constant level. An overview of the different tests is displayed in Table 3.2.

- Test01

No damage was observed on the Grassblocks after Test01. The only forces on the blocks were caused by layers of water flowing over the blocks. There was no overtopping water that came loose from the inner slope. Furthermore it was noticed that the blocks interlocked well. Unfortunately the paddle wheels did not function properly in Test01. As a result the flow velocity measurements could not be used for this research. Only the pressure measurements of Test01 can be used.
- Test02A

Test02A was aborted after 171 waves due to technical issues with the wave paddle. Due to this technical issue, the generated waves did not show any correlation with the simulated waves in OpenFOAM, which will be explained in Section 4.1.4. Therefore, this test could not be used for this research.
- Test02B

No damage was noticed on the Grassblocks after Test02B and the blocks interlocked well. The forces on the blocks were mostly caused by layers of water flowing over the blocks. Furthermore, sometimes the overtopped water came loose at the top of the inner slope. For this test, the generated waves did also not show any correlation with the simulated

waves in OpenFOAM (see Section 4.1.4). This could occur due to the issues with the wave paddle from Test02A and also led to this test not being usable for the research.

- Test03

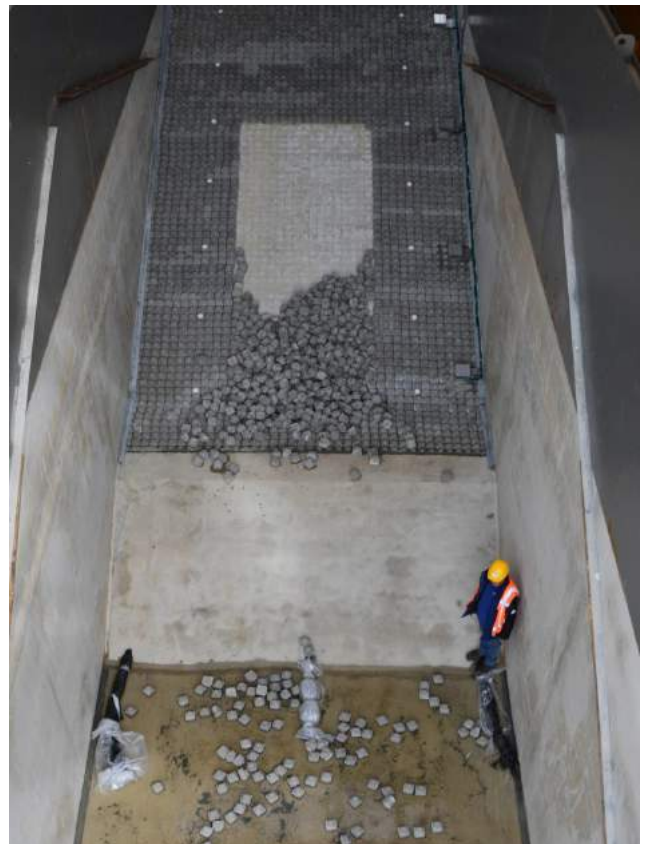
At Test03 the Grassblocks collapsed after which this test was also aborted. The damage on the blocks started at the toe of the inner slope and then the formation of the blocks collapsed. Fig. 3.6b shows the damage after the blocks have collapsed.

Table 3.2: The wave characteristics during the four tests with the water depth h , significant wave height H_{m0} , maximum wave height H_{max} , peak wave period T_p , average wave period T_m , spectral wave period $T_{m-1,0}$, amount of waves N , wave steepness s_p , $s_{m-1,0}$ and specific overtopping discharge q .

Test	h [m]	H_{m0} [m]	H_{max} [m]	T_p [s]	T_m [s]	$T_{m-1,0}$ [s]	N [-]	s_p [-]	$s_{m-1,0}$ [-]	q [l/s/m]
Test01	6.9	1.48	2.66	4.89	4.02	4.54	1032	0.040	0.046	9.3
Test02A	6.9	1.69	2.49	5.11	4.54	4.81	171	0.041	0.047	19.7
Test02B	6.9	1.68	2.65	5.23	4.36	4.87	989	0.039	0.045	23.2
Test03	6.9	1.63	2.36	7.23	5.98	6.53	54	0.020	0.024	34.2



(a) Wave overtopping during the test.



(b) Damage on the Grassblocks after Test03.

Figure 3.6: Wave overtopping and damage on Grassblocks during tests (Van Steeg, 2017).

4 | Methodology

4.1 Coupling of hydrodynamic model

4.1.1 OpenFOAM model

OpenFOAM (Open-source Field Operation And Manipulation) is a C++ based open source software mainly used for Computational Fluid Dynamics. OpenFOAM currently consists of three different branches. The original OpenFOAM has been released in 2004 by OpenCFD Ltd (OpenCFD Ltd., 2020). A variant of OpenFOAM called FOAM-Extend has been released in 2009 by Wikki Ltd. In 2012 another variant was released called OpenFOAM Foundation Inc.

For this research OpenFOAM 1712 (released in December 2017) from OpenCFD Ltd is used. This version has been chosen because it is the latest version that is compatible with the porousWaveFoam solver, a solver that can specify one or more permeable layers (Jensen et al., 2014). This solver is part of the waves2Foam toolbox, created by Jacobsen et al. (2012) for the generation and absorption of free surface waves. In combination with the third-party software OceanWave3D (Engsig-Karup et al., 2009), it can evaluate fully non-linear wave propagation. Waves2Foam has been coupled with OceanWave3D by Paulsen et al. (2014).

4.1.2 Computational Domain and Mesh

The first step is implementing the dike geometry into OpenFOAM. This has been done using blockMesh, a utility within OpenFOAM that decomposes the domain geometry into a set of one or more three-dimensional, hexahedral blocks. The dimensions as displayed in Figs. 3.1 and 3.2 have been used to implement the Delta wave flume and dike geometry in OpenFOAM, as can be seen in Fig. 4.1. The flume in OpenFOAM starts at 42.5 m from the wave generator up to 206 m. The height is 12.1 m, which is 2.8 m higher than the crest of the dike. This is also where the inlet relaxation zone is implemented.

The relaxation zone creates a boundary condition that avoids internally reflecting waves at the wave generating boundary. According to Miquel et al. (2018) the length of the relaxation zone should be one wavelength. Based on the implicit relation in Eq. (4.1) and the spectral wave period $T_{m-1,0}$ as shown in Table 3.2, the wavelength L for each test has been calculated (Table 4.1). The outlet zone has been set behind the dike structure and therefore does not influence the model.

$$L = L_0 \tanh \frac{2\pi h}{L}, \text{ with } L_0 = \frac{gT^2}{2\pi} \quad (4.1)$$

Table 4.1: Wavelengths in physical test

	L_0 [m]	L [m]
Test01	32.17	29.54
Test02	37.02	33.13
Test03	66.55	47.49

In this geometry, a mesh has been generated (Fig. 4.2). According to Pedersen et al. (2017) and Jacobsen et al. (2012), maintaining an aspect ratio of $\Delta x/\Delta z = 1$ throughout the entire computational domain improves the accuracy and numerical stability of the model. Using a grid size of $30\text{ cm} \times 30\text{ cm}$ leads to 40 cells in the vertical direction. Because the amount of vertical cells stay the same along the whole profile, the grid cells get smaller along the dike slope. The grid size on the crest and landward slope is $7\text{ cm} \times 7\text{ cm}$. Similar to the research by Chen et al. (2021), a wall function has been used in the boundary layer near the bottom surface of the whole flume. The mesh has been refined here using 10 cells with a height of 1 cm to simulate the vertical velocity profile accurately.

Windt et al. (2019) have shown that 10 layers of cells per wave height are needed to resolve the wave height accurately. As displayed in Table 3.2, the significant wave heights vary from 1.48 m up to 1.69 m. With a minimum of 10 vertical layers per wave height, this would require a grid size of $15\text{ cm} \times 15\text{ cm}$. Therefore using the OpenFOAM tool snappyHexMesh, the grid has been locally refined near the water surface, which is at 6.9 m with an offset of $\pm 2.0\text{ m}$ ($Z = 4.9\text{ m} - 8.9\text{ m}$). In horizontal direction the grid is refined at the start of the flume until the start of the slope ($X = 42.5\text{ m} - 164.19\text{ m}$). The grid refinement can be seen on the left side of Fig. 4.2.

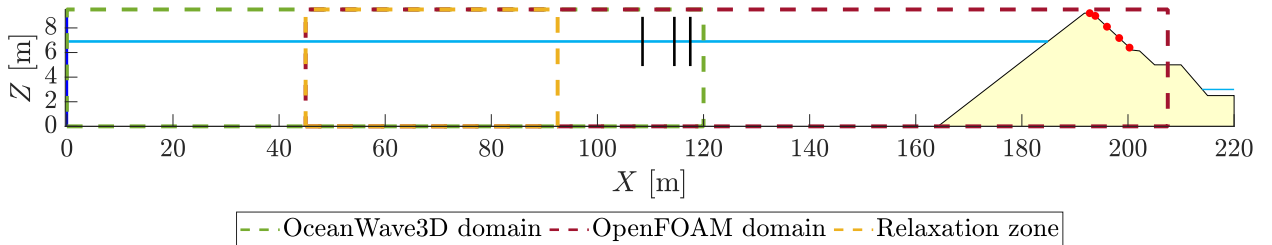


Figure 4.1: Overview of OceanWave3D and OpenFOAM domain.

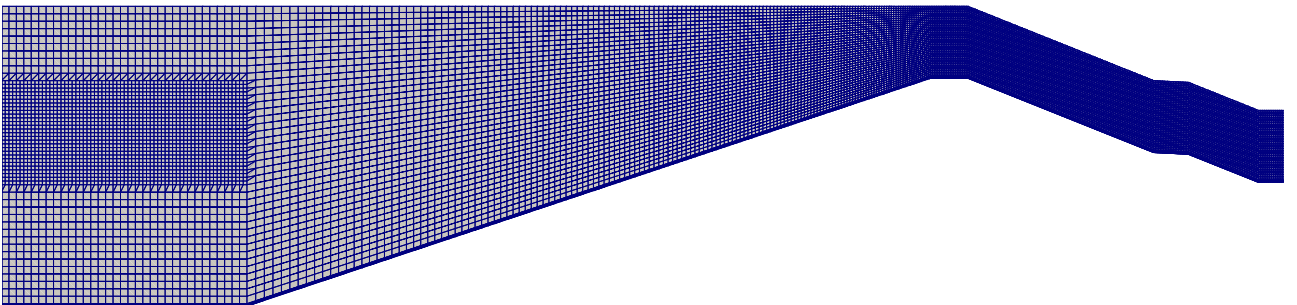


Figure 4.2: A section of generated mesh in OpenFOAM.

The adaptive time steps of the model are controlled by a predefined maximum Courant number, defined as `maxCo` in OpenFOAM. Using a maximum Courant number in Eq. (4.2), with a known spacing of grid leads to a certain adjustable time step, depending on the magnitude of the velocity. Convergence analysis by Gruwez et al. (2020) has shown that at $C = 0.45$ numerical instabilities occurred, whereas $C = 0.25$ showed a good balance between accuracy and computational costs. Therefore, the `maxCo` for this research has been set to 0.25.

$$C = \frac{u\Delta t}{\Delta x} \quad (4.2)$$

C = Courant number [-]
 u = magnitude of velocity [m/s]
 Δt = time step [s]
 Δx = spacing of grid [m]

4.1.3 Turbulence model

Turbulence models are used in CFD to include the effect of turbulence in the simulation of fluid flows. In turbulent flow, the speed of a fluid at a point is constantly undergoing changes in magnitude and direction. Including the effect of turbulence can be done by Direct Numerical Simulation (DNS) or Large Eddy Simulation (LES), which both require a high resolution of spatial dimensions (Larsen and Fuhrman, 2018).

A more efficient alternative are equations based on Reynolds-Averaged Navier-Stokes (RANS), which require a separate closure model for describing the effects of the turbulence on the mean flow (Larsen and Fuhrman, 2018). This is generally done using one of the two main equation models ($k - \varepsilon$ and $k - \omega$) that describe the turbulence by two transport equations (partial differential equations). Here k is the turbulent kinetic energy [m^2/s^2], ε rate of dissipation of turbulent kinetic energy [m^2/s^3] and ω the specific rate of dissipation of turbulent kinetic energy.

However, $k - \varepsilon$ models have the disadvantage of not accurately modeling the viscous sub-layer near the wall. Furthermore, they tend to under-perform under adverse pressure gradients. $k - \omega$ models perform better near walls and in cases of adverse pressure gradient (Wilcox, 2006). Another type of turbulence model is the Shear Stress Transport (SST) model, which is a combination of the $k - \varepsilon$ and $k - \omega$ model and aims to combine the $k - \omega$ model for near wall treatment and the $k - \varepsilon$ in the free stream (Menter, 1993).

Larsen and Fuhrman (2018) showed that these two types of turbulence models are unconditionally unstable and tend to overestimate the turbulence levels. Therefore, they have provided stabilized versions of these turbulence models. The turbulence model has a stress limiter λ_1 and an effective potential flow threshold λ_2 . Larsen and Fuhrman (2018) suggested a value of $\lambda_2 = 0.05$. For λ_1 either 0.2 and 0.875 are mentioned. Chen et al. (2021) showed that $\lambda_1 = 0.2$ performed best in a $k - \omega$ model for wave overtopping. Therefore the $k - \omega$ model with $\lambda_1 = 0.2$ and $\lambda_1 = 0.05$ has been used for this experiment.

4.1.4 Wave Generation

The movement of the wave paddle at the Delta flume is controlled by a steering file. Deltares has provided these steering files, which have then been used to translate the movement of

the wave paddle into the OpenFOAM environment. This has been done using OceanWave3D (Engsig-Karup et al., 2009), a tool used for simulation of non-linear and dispersive free surface waves, which has been coupled with waves2Foam (Paulsen et al., 2014). Fig. 4.3 shows the generated waves in the OpenFOAM domain. The generated waves then had to be calibrated to ensure that they accurately represent the waves from the physical experiment. Wave height meters have been defined in OpenFOAM at the same location (see Table 3.1) as used in the physical experiment. Using the wave separation method of Mansard and Funke (1980), the spectral density of the free surface elevation could be determined. Based on this, the m_0 and m_{-1} moment of the spectral density have been calculated. Using these moments of spectral density, an estimate of the significant wave height $H_{m0} = 4\sqrt{m_0}$ and spectral wave period $T_{m-1,0} = m_0/m_1$ has been made. The waves have then been calibrated by comparing H_{m0} and $T_{m-1,0}$ of the OpenFOAM generated waves and the physical test waves. The solver used for this calibration is porousWaveFoam, a solver that can solve porous layers which is used later in this research. Using the same solver in the process of calibrating the waves ensures that the waves are calibrated accurately further in the project as well.

Furthermore, there was also a time lag between the measured data and the simulated data. The generated waves in the experiment required a run-up time. After this run-up time the measuring equipment was turned on. Using cross-correlation analysis, the time lag could be determined between both time series for each test. This gave a time lag of 73.57 s for Test01 and 61.07 s for Test03. However, using the same method for Test02A and Test02B, no correlation could be found between the measured wave heights and the simulated wave heights. This could occur due to the wave paddle having technical issues in this test, as described in Section 3.4.



Figure 4.3: Generated waves of Test03 in OpenFOAM.

4.1.5 Validation

The model has been validated by comparing the empirical formulae for run-up flow velocity and run-up flow thickness along the water side slope with the measured values in OpenFOAM. The empirical values for run-up velocity and flow thickness have been calculated according to Eqs. (2.7) and (2.8) on three locations along the waterside slope (Fig. 4.4 and Table 4.2). Fig. 4.5 shows the run-up flow velocity and flow thickness along the waterside slope of the dike, calculated using the empirical equations Eqs. (2.7) and (2.8). The exact values are displayed in Table B.1. These empirical values have been compared to the modelled values.

The flow thickness h has been determined with probes that are installed orthogonal from the waterside slope on an interval of 8 cm. Each of these probes gives an outcome for the α_{water} , a variable that defines the ratio of water within a cell. This value is measured on a frequency of 100 Hz. Using a minimum value for $\alpha_{water} = 0.6$, the flow thickness could be determined. Subsequently, the 2% values have been calculated according to the amount of waves N . For Test01, with $T_m = 4.02$ s and a simulation time of 500 s, this leads to $N \approx 124$ waves. Therefore the 2% highest wave is the 2nd highest wave. For Test03, $T_m = 5.98$ s in 350 s gives $N \approx 58$

waves. This makes the highest wave in this period also the 2% highest wave, leading to the 2% flow thickness.

The flow velocity u has been determined in the direction parallel to the waterside slope. The flow velocities have been depth-averaged, using the cells required for the flow thickness calculation. They have been measured with a frequency of 100 Hz. OpenFOAM provides the velocities in three directions; X, Y and Z-direction. Using a rotation matrix, the flow velocity along the slope has been determined. Subsequently, the 2% flow velocities have been calculated using the same method as for the 2% flow thickness.

Lastly, the pressures measured by PS1 (see Fig. 3.5a) on a frequency of 100 Hz have also been used to validate the timing of the overtopping. The pressure has been measured at the lowest cell on the same location at $[X=192.79 \text{ m}, Z=9.2 \text{ m}]$ as in the physical test (Table 3.1). This pressure sensor only observes whether there is water on the crest of the dike or not. Therefore, the quantity of the modelled and observed pressures have not been compared. However, it can be used to verify whether the timing of the overtopping in the OpenFOAM model matches with the physical test. The pressure is defined as the total pressure p_0 [Pa], which is calculated in OpenFOAM according to $p_0 = p_s + \frac{1}{2}\rho|\mathbf{u}|^2$ for incompressible fluids. Here p_s is the static pressure [Pa], ρ the density of water [1000 kg/m^3] and u the flow velocity [m/s].

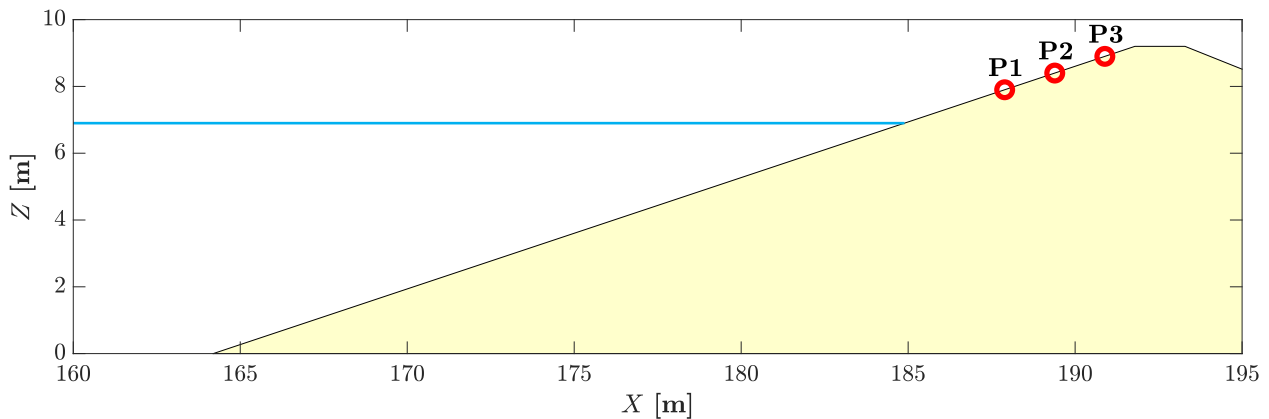
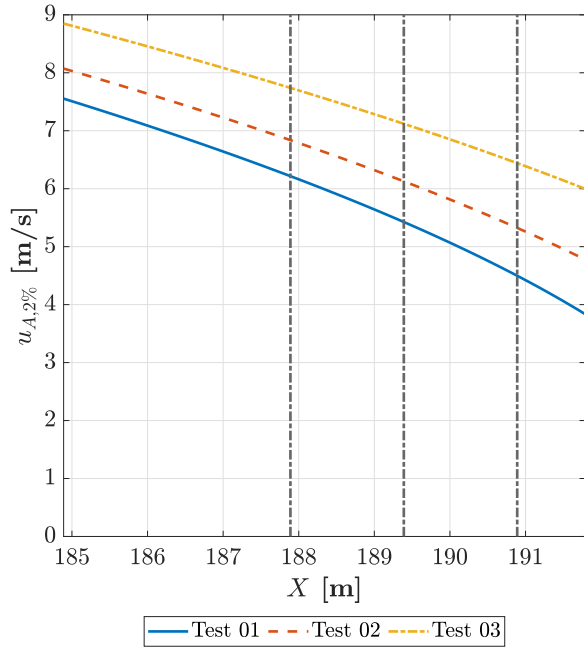


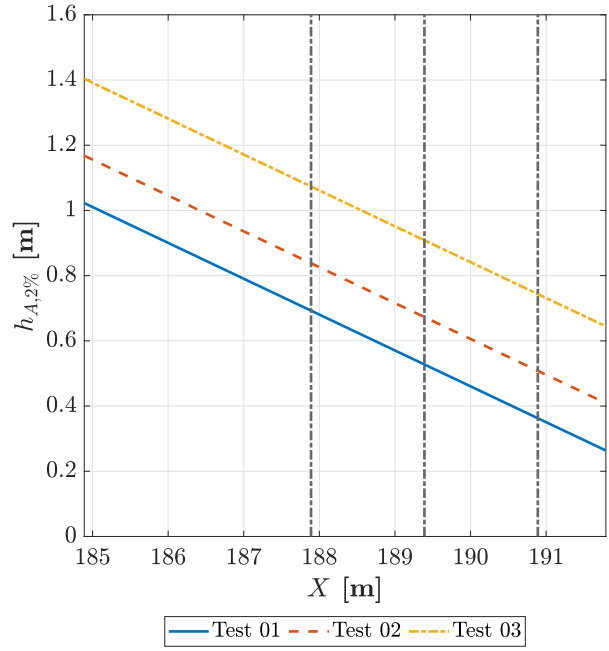
Figure 4.4: Measuring points P1-P3 on waterside slope of the dike.

Table 4.2: Location of measuring points P1 - P3.

	X-location [m]	Z-location [m]
P1	187.9	7.9
P2	189.4	8.4
P3	190.9	8.9



(a) Run-up velocity $u_{A,2\%}$ [m/s] over the horizontal position X [m] along the water side slope.



(b) Run-up flow thickness $h_{A,2\%}$ [m] over the horizontal position height X [m] along the water side slope.

Figure 4.5: Run-up velocity and flow thickness exceeded by 2% of the up-rushing waves calculated using the run-up equations (Eqs. (2.7) and (2.8)). The vertical lines represent the locations of P1, P2 and P3.

4.2 Implementation of block revetments

4.2.1 Porous solver

For permeable structures, Jensen et al. (2014) developed the porousWaveFoam solver, which is an adaptation of the waveFoam solver. The waveFoam solver solves the Reynolds-Averaged Navier-Stokes (RANS) equations with a tracking of the free surface with a Volume of Fluid (VOF) approach.

The velocity inside the porous layer is defined as the filter velocity. This filter velocity u is related to the pore velocity u_p through the porosity n (Eq. (4.3)).

$$\mathbf{u} = n\mathbf{u}_p \quad (4.3)$$

According to Jensen et al. (2014), a physical correct representation will be the divergence of the filter velocity $\bar{\mathbf{u}}$ being zero. This leads to the incompressible continuity equation (Eq. (4.4)).

$$\nabla \cdot \langle \bar{\mathbf{u}} \rangle = 0 \quad (4.4)$$

The momentum equation as used by the porousWaveFoam solver is displayed in Eq. (4.5), where ρ is the density of the fluid, \mathbf{u} is the velocity vector in Cartesian coordinates, t is time, $\nabla = (\partial/\partial x, \partial/\partial y, \partial/\partial z)$ is the differential operator, \mathbf{g} is the vector of acceleration due to gravity, $\mathbf{x} = (x, y, z)$ is the Cartesian coordinate vector, $p^* = p - \rho \mathbf{g} \cdot \mathbf{x}$ is the excess pressure, \mathbf{x}_r is a reference location (defined at sea level) and μ_{tot} is the total dynamic viscosity (Jensen et al., 2014).

$$(1 + C_m) \frac{\partial \rho \mathbf{u}}{\partial t} \frac{1}{n} + \frac{1}{n} \nabla \cdot \frac{\rho}{n} \mathbf{u} \mathbf{u}^T = -\nabla p^* + \mathbf{g} \cdot (\mathbf{x} - \mathbf{x}_r) \nabla \rho + \frac{1}{n} \nabla \cdot \mu_{tot} \nabla \mathbf{u} - \mathbf{F}_p \quad (4.5)$$

The added mass coefficient is defined as C_m , where γ_p is a closure coefficient and is set to 0.34.

$$C_m = \gamma_p \frac{1 - n}{n} \quad (4.6)$$

The flow resistance \mathbf{F}_p is described by the Darcy-Forchheimer resistance equation (Eq. (4.7)).

$$\mathbf{F}_p = a\mathbf{u} + b\rho \|\mathbf{u}\|_2 \mathbf{u} \quad (4.7)$$

$$a = \alpha \frac{(1 - n)^2}{n^3} \frac{\nu}{d_{50}^2}, \quad b = \beta \left(1 + \frac{7.5}{KC} \right) \frac{1 - n}{n^3} \frac{1}{d_{50}} \quad (4.8)$$

a and b are resistance terms as displayed in Eq. (4.8), defined by Van Gent (1995). Here ν is the kinematic viscosity and d_{50} is the nominal diameter of the porous material. The first term dominates the linear flow regimes, whereas the second term dominates the turbulent regimes. α and β are called the resistance coefficients.

$$KC = \frac{H_{m0}}{2} \sqrt{\frac{g}{h}} \frac{1.1 T_{m-1,0}}{d_{50}} \quad (4.9)$$

KC is the Keulegan-Carpenter number and describes the relative importance of the drag forces over inertia forces in an oscillatory fluid flow. For small KC numbers the inertia dominates, whereas for large KC number the turbulent drag forces dominate. According to Jacobsen et al. (2015), the KC number for the blocks is not an easy parameter to estimate. Ideally the KC number should be used with a temporal and spatial distribution with a temporal variation to account for the changing hydrodynamics during an irregular time series. Because this is not feasible in OpenFOAM, the KC number is based on the incident wave field and shallow water wave theory, as shown in Eq. (4.9). Using the significant wave height H_{m0} , spectral wave period $T_{m-1,0}$ and water depth h from Table 3.2 and $d_{50} = 0.125$ m (diameter of Grassblocks) gives $KC = 35.25$ for Test01 and $KC = 55.83$ for Test03.

4.2.2 Resistance Coefficients

The resistance coefficients have been originally introduced by Van Gent (1995). Based on experiments where he measured the permeability to study porous flow, he proposed $\alpha = 1000$ and $\beta = 1.1$ as resistance coefficients in Eq. (4.8). These values have also been used in research by Jacobsen et al. (2015).

Losada et al. (2008) explained that the resistance coefficients depend on parameters such as the Reynolds number, the shape of the stones, the grade of the porous material, the permeability and the flow characteristics. However, the precise descriptions of the α and β coefficients are still not fully understood for oscillatory flows and waves propagating over slopes or breaking. For these conditions, the values as proposed in earlier literature may not be valid since the experimental conditions for obtaining those formulae were not considering these effects. Based on a comparison of experimental data and numerical results, he proposed $\alpha = 200$ and $\beta = 0.8$ as the best-fit parameters in his research.

Furthermore Jensen et al. (2014) compared experimental data with numerical outcomes. Based on research by Burcharth and Andersen (1995) the Reynolds number in porous media can be determined using Eq. (4.10), where ν is the kinematic viscosity of water [m²/s].

$$Re_p = \frac{\langle \bar{u} \rangle d_{50}}{n\nu} \quad (4.10)$$

Based on this Reynolds number, a distinction has been made for different kinds of flow regimes. The first is a non-linear flow regime, also described as the Forchheimer flow regime, ($10 < Re_p < 150$). The second is an unsteady laminar flow regime, also called the transitional flow regime ($150 < Re_p < 300$). The last one is the fully turbulent flow regime, with $Re_p > 300$. According to Jensen et al. (2014) the resistance coefficients $\alpha = 500$ and $\beta = 2.0$ performed best considering all flow regimes.

Three different sets of resistance coefficients have been created based on these three researches by Van Gent (1995); Losada et al. (2008); Jensen et al. (2014), as displayed in Table 4.3.

Table 4.3: Resistance coefficients.

Research	α	β
Van Gent (1995)	1000	1.1
Jensen et al. (2014)	500	2.0
Losada et al. (2008)	200	0.8

The porous zones which are defined by these resistance properties can be implemented into OpenFoam using porosityZones. The porosityZones have been applied in OpenFOAM on the location of the Grassblocks (Figs. 4.6 and 4.7). The porous zone starts at $X = 191.04$ m from the top of the waterside slope at a height of $Z = 8.95$ m. It ends at the toe of the landward slope, $X = 201.79$ m at a height of $Z = 6.2$ m. The porous zone has a depth of 36 mm over the whole layer, which is the same height as the open top part of the Grassblocks (see Appendix G).

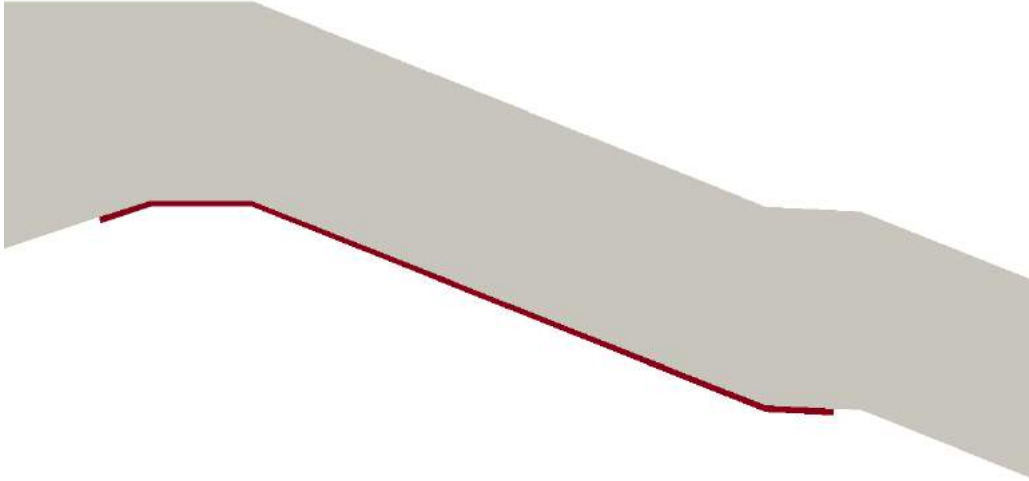


Figure 4.6: Section of the adapted dike geometry, shaded in red is the porosityZone.

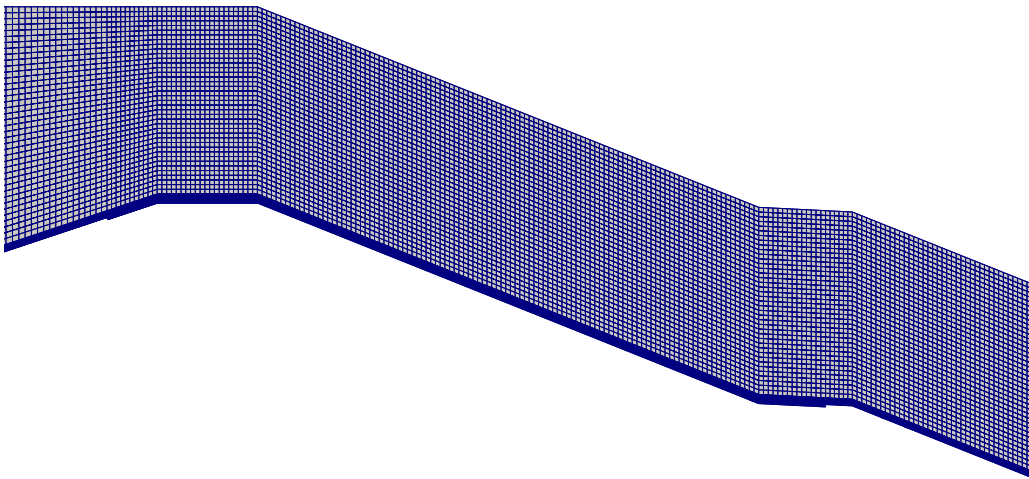


Figure 4.7: Section of the adapted generated mesh on dike geometry in OpenFOAM.

4.2.3 Calibration and Validation

The pressures and flow velocities have been measured in OpenFOAM using probes. These probes have been installed in OpenFOAM at the same locations as in the physical test (Table 3.1). Because Test02a and Test02b cannot be used, the choice has been made to use the first half of Test03 ($t = 0 - 170$ s) for calibration. The wave conditions from this test are used to run the three resistance coefficients sets as introduced in Table 4.3. For each set an OpenFOAM simulation has been done.

The peak flow velocity and peak pressure of each overtopping wave have been assessed, because the peak values of the flow velocity and pressure have the most influence on the dike cover. An overtopping wave is defined when a minimum pressure of 0.2 kPa and a minimum flow velocity of 0.5 m/s occurs. The modelled peak pressures and velocities of each run are compared with the peak pressures and velocities as measured in the physical test. The peak flow velocities are measured by PW1 and PW2, whereas the peak pressures have been measured by PS2 - PS5. Using the Nash-Sutcliffe Efficiency (NSE), introduced by Nash and Sutcliffe (1970), the performance of each resistance coefficients set has been determined (Eq. (4.11)). For the NSE, a value of 1 indicates a perfect fit between the modelled and observed data. Furthermore the Root Mean Square Error (RMSE) has also been used to indicate the difference between the modelled and observed peak values (Eq. (4.12)). For the RMSE a value of 0 indicates a perfect fit to the data. In these equations X_m is the modelled value and X_o the observed value, where \bar{X}_o is the mean of the observed values.

$$\text{NSE} = 1 - \frac{\sum_{t=1}^T (X_m^t - X_o^t)^2}{\sum_{t=1}^T (X_o^t - \bar{X}_o)^2} \quad (4.11)$$

$$\text{RMSE} = \sqrt{\frac{\sum_{i=1}^N (X_o - X_m)^2}{N}} \quad (4.12)$$

For the validation, the best performing resistance coefficient set is being used in Test01 and the second half of Test03 ($t = 170 - 350$ s). Only the pressures are validated for Test01, because the flow velocities have not been accurately measured in the physical test, as described in Section 3.4. The validated flow velocities and pressures are also assessed on their NSE and RMSE performance. The pressure time series in the calibration and validation phase have been moving averaged over a window of 1 s. This has been done for graphical simplification, because the pressure time series show a lot of fluctuations, which has also been indicated by Van Bergeijk et al. (2020). However, the original non-averaged pressure data has been used for the calibration and validation phase.

4.3 Hydrodynamic conditions on block revetments

4.3.1 Hydrodynamic conditions on Grassblock

The final phase in this research is determining the forces that occurred on the landward slope that caused the block revetments to collapse. As displayed in Fig. 4.8, the block revetments started to collapse at the toe of the landward slope after 300 s in Test03. The location where this occurred is [$X = 200.79$ m, $Z = 6.2$ m], as displayed in Fig. 4.9.

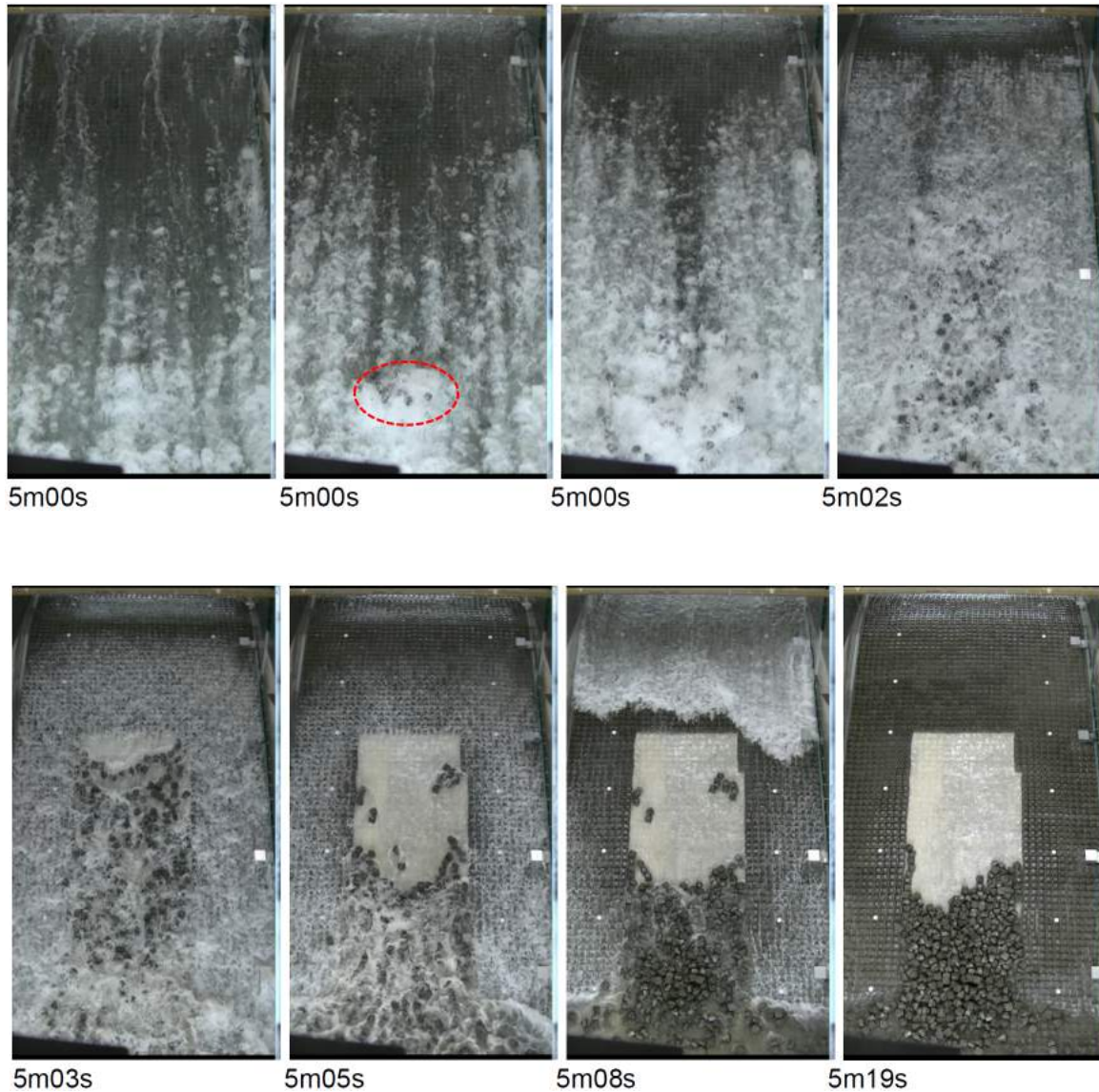


Figure 4.8: Impression of the occurrence of damage during Test T03, the red dashed circle indicates the location where damage occurred first (Van Steeg, 2017)

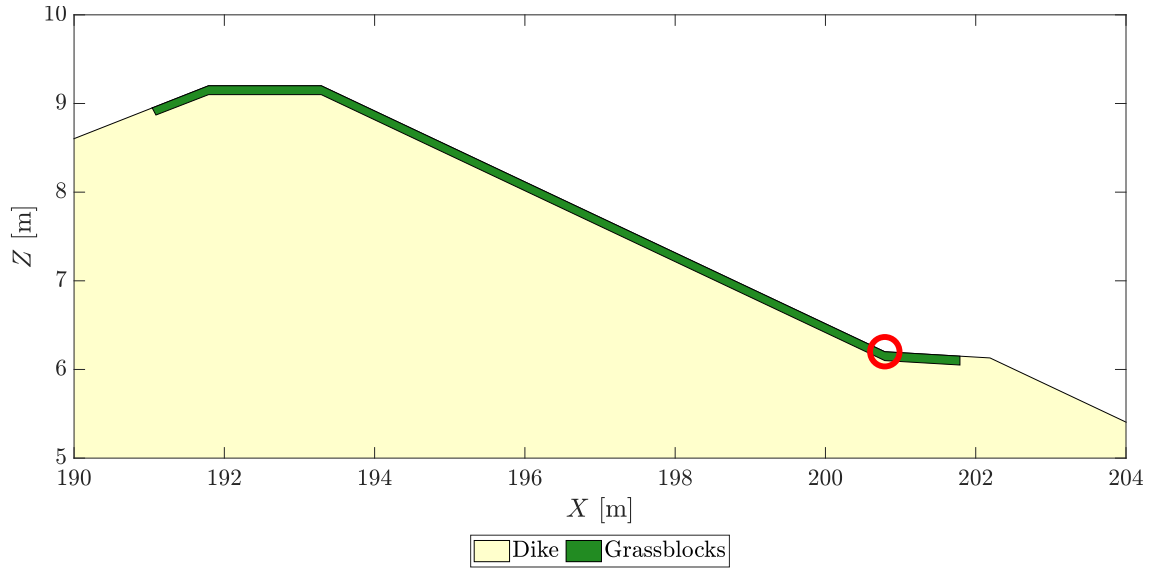


Figure 4.9: Location of occurrence of damage on block revetments (circled in red)

To determine what caused the formation of block revetments to collapse, it is important to determine the following forces on this location;

- Pressure p [kPa]
- Flow thickness h [m]
- Flow velocity u [m/s]
- Shear stress τ_s [m^2/s^2]

The calibrated and validated model has now been used to determine these forces on the location of failure in Test03. The probes have been installed on the bottom of the porous layer, which is 36 mm below the top of the blocks. The hydrodynamic conditions have been measured on a frequency of 100 Hz.

4.3.2 Sensitivity analysis of block revetment properties

Besides the Grassblock, the model can also be used to assess the effect of other types of block revetments. The variables porosity n and thickness of the porous zone have been adjusted to represent other types of block revetments. This can be a valuable tool for the design phase of improved block revetments. A sensitivity analysis has been done to assess the effect of changes in the porosity or the porous layer on the hydrodynamic conditions. The porosity has been run using five different values (Table 4.4), using the default porous layer thickness of 0.036 m. Subsequently, five separate runs have been done with different porous layer thicknesses (Table 4.5). For these runs the porosity has been kept at $n = 0.4$. The results of this sensitivity analysis can be used to determine which type of block performs best in reducing the hydrodynamic load. The probes measure with a frequency of 100 Hz and have been installed on the same location as Section 4.3.1, which is at 36 mm below the top of the blocks.

Table 4.4: Porosity n used for sensitivity analysis.

#	n [-]
1	0.2
2	0.3
3	0.4
4	0.5
5	0.6

Table 4.5: Porous layer thicknesses used for sensitivity analysis.

#	Porous layer thickness [m]
1	0.016
2	0.026
3	0.036
4	0.046
5	0.056

5 | Results

5.1 Coupling of hydrodynamic model

The results of the coupling of the hydrodynamic model consist of multiple criteria. First the results of the calibration of the wave characteristics are displayed. These wave characteristics are complemented with the free surface elevation and the wave energy density spectrum. Subsequently, the flow velocity and flow thickness have been verified according to empirical formulae (Schüttrumpf and Van Gent, 2003).

5.1.1 Wave Characteristics

The calibration of the free surface elevation has been done using the significant wave height and spectral wave period. Table 5.1 shows the comparison between the physical and simulated H_{m0} and $T_{m-1,0}$. Test01 has been calibrated based on a period of 500 s, whereas Test03 is calibrated on a period of 330 s, which is the full length of Test03 until damage on the Grassblocks occurred. With an inaccuracy of 0.001 m (+0.08%) for the significant wave height in Test01, the OpenFOAM model shows significant accuracy on the free surface elevation. The spectral wave period is slightly underestimated with 0.029 s (-0.62%). For Test03 the significant wave height is also almost equal with an overestimation of 0.001 m (+0.07%), whereas the spectral wave period is slightly overestimated with 0.206 s (+3.24%).

Table 5.1: Significant wave height and spectral wave period of physical test and OpenFOAM model for Test01 and 03

(a) Test01 ($t = 0 - 500$ s)			(b) Test03 ($t = 0 - 330$ s)		
	H_{m0} [m]	$T_{m-1,0}$ [s]		H_{m0} [m]	$T_{m-1,0}$ [s]
Physical	1.282	4.691	Physical	1.364	6.356
OpenFOAM	1.283	4.662	OpenFOAM	1.365	6.562

Fig. 5.1 shows the incoming propagation of the free surface elevation on the location of the first wave height meter ($X = 108.5$ m) between 200 and 250 s of Test01. Fig. 5.2 shows the free surface elevation for this time period in Test03. The full time series can be found in Appendix A, Fig. A.1 for Test01 and Fig. A.2 for Test03.

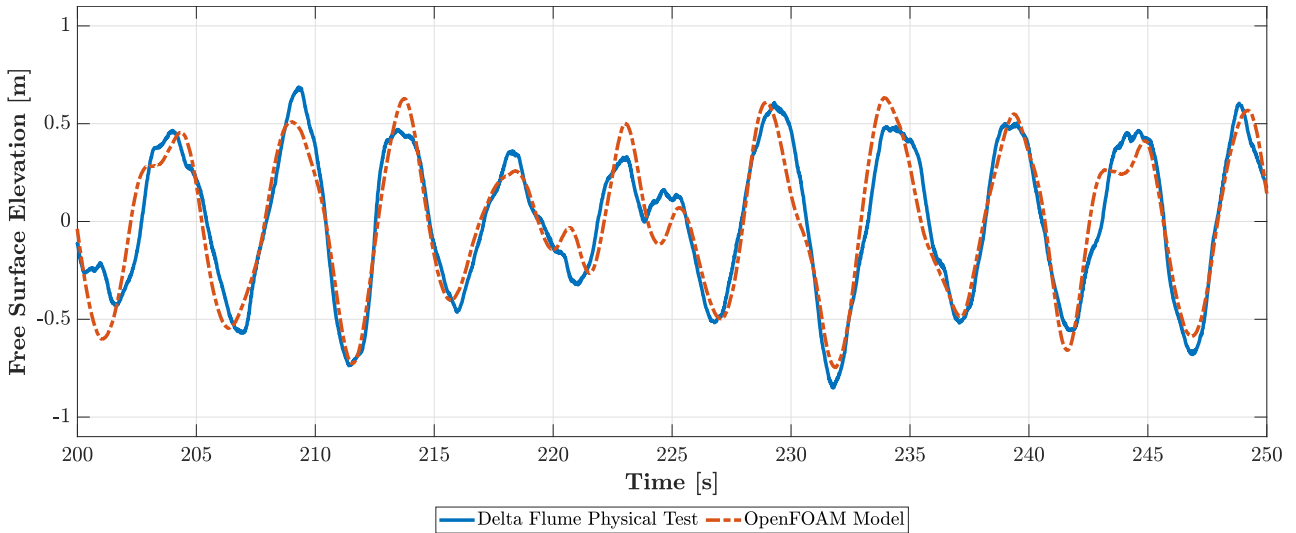


Figure 5.1: Free surface elevation of incoming waves at $X=108.5$ m from $t = 200 - 250$ s in Test01.

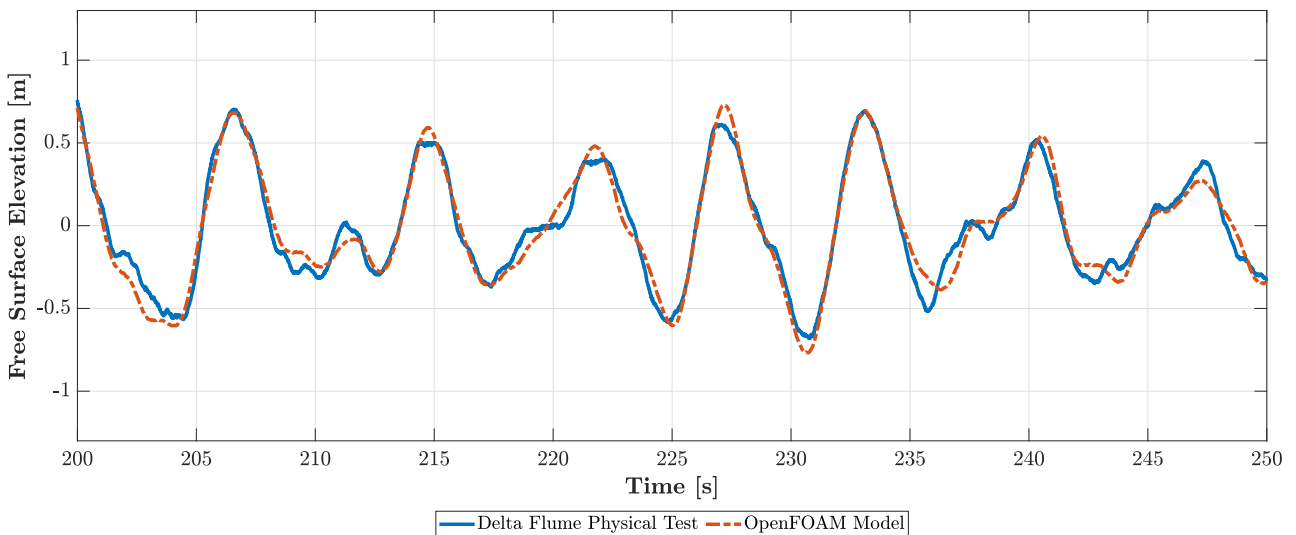


Figure 5.2: Free surface elevation of incoming waves at $X=108.5$ m from $t = 200 - 250$ s in Test03.

Fig. 5.3 shows the spectral density of the incoming waves at the location of WHM01. This shows that the peak energy density of $1.623 \text{ m}^2/\text{Hz}$ occurs at 0.21 Hz, which means the peak wave period is 4.79 s. It also shows that the model can generate the waves with frequencies lower than 0.22 Hz very accurately. Between the frequencies 0.22 Hz and 0.28 Hz the model slightly underestimates the energy of the waves, whereas for 0.28 Hz up to 0.38 Hz the model slightly overestimates the spectral density. Fig. 5.4 also shows the lower frequencies being accurately modelled. The peak energy density is $1.934 \text{ m}^2/\text{Hz}$ at 0.14 Hz, which matches well with the experimental results. From 0.19 Hz until 0.32 Hz the energy density of the waves is slightly underestimated. However, these higher frequencies have no significant influence on the wave

propagation and wave overtopping. The lowest frequencies are most important for the wave propagation and these are approximated well by the model.

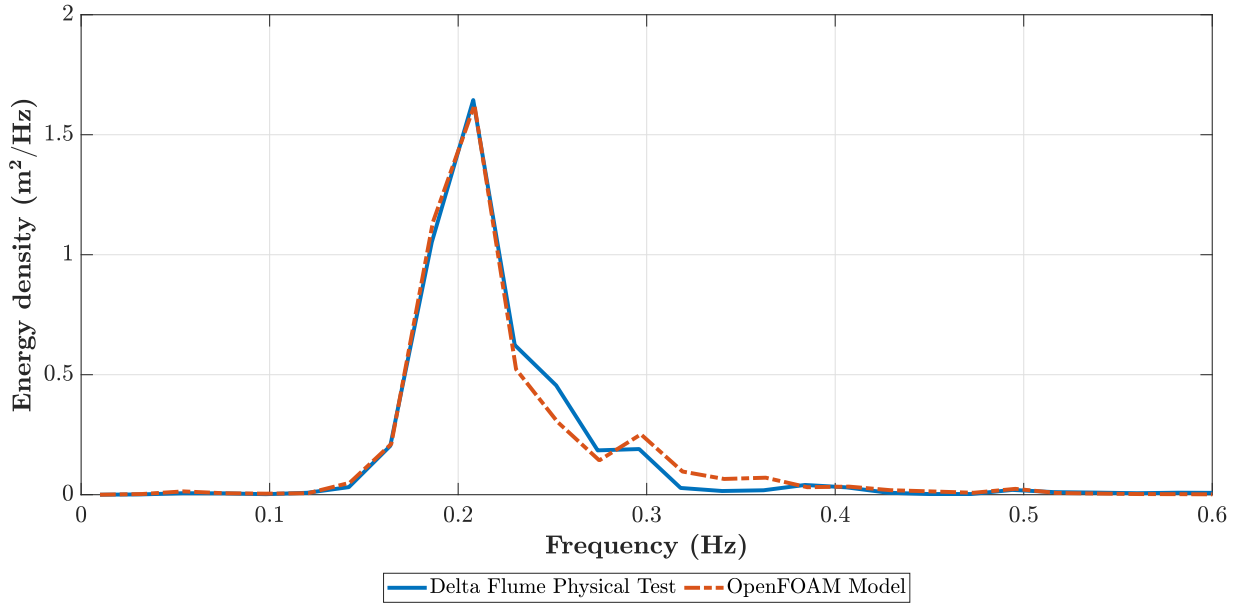


Figure 5.3: Energy density spectrum of incoming waves at X=108.5 m in Test01

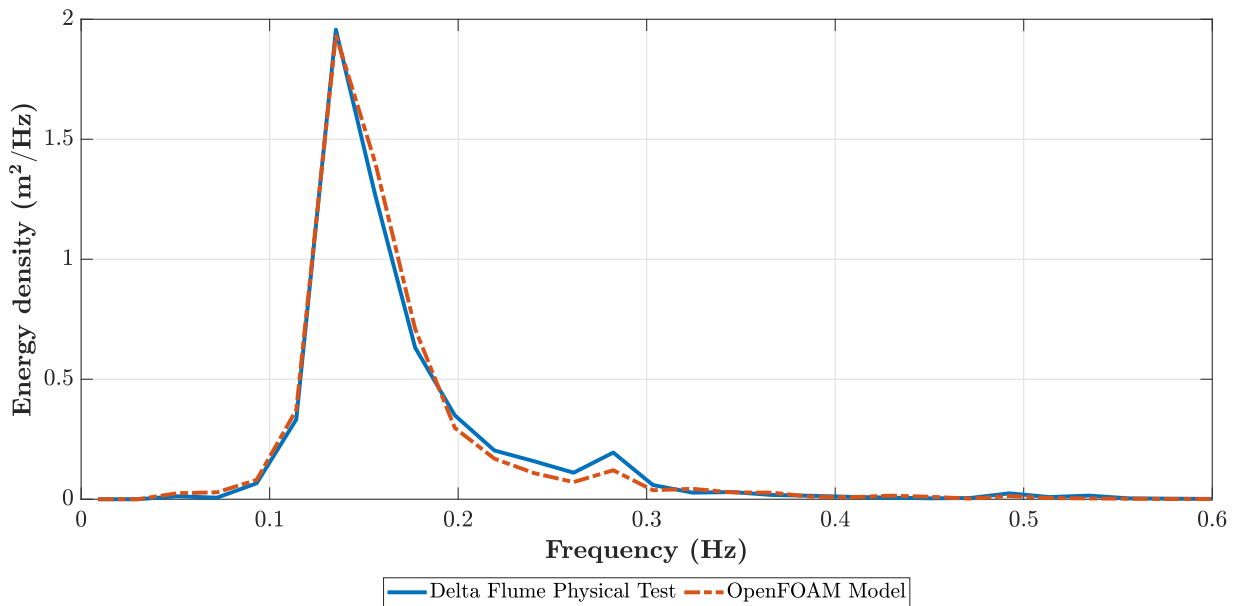


Figure 5.4: Energy density spectrum of incoming waves at X=108.5 m in Test03

5.1.2 Flow Velocity & Flow Thickness

Fig. 5.6 shows the modelled against the empirical 2% flow thickness and flow velocity, only exceeded by 2% of the incident waves. The empirical values have been calculated according to Schüttrumpf and Van Gent (2003) and are shown in Table B.1. The 2% modelled and empirical flow velocities are displayed in Fig. 5.6a. This shows that the model prediction of the flow velocities gets more accurate closer to the crest along the waterside slope. This could occur

due to the breaking of the waves. At P1, the deviation from the empirical values is the largest, with -1.466 m/s for Test01 and -0.491 m/s for Test03. Here the wave run-up could also be influenced by the breaking of the wave, whereas at P3 the flow velocity consists of

At P3 the flow velocities are slightly over-estimated with 0.477 m/s for Test01 and 0.237 m/s for Test03.

Fig. 5.6b shows the modelled 2% flow thickness against the empirical 2% flow thickness. This shows that both Test01 and Test03 predict the 2% flow thickness quite accurately. It also shows that at location P1 the model predicts the least accurate, similar to the 2% flow velocities. Further along the slope, at points P2 and P3, the modelled $h_{A,2\%}$ gets more similar to the empirical $h_{A,2\%}$. Especially at P3 the model is accurate, with a deviation of -0.018 m for Test01 and 0.016 m for Test03. Noticeable is that for Test01, the flow thickness at P1 is over-predicted in the model (deviation of $+0.063$ m), whereas in Test03 the flow thickness is a bit under-predicted at P1 (-0.124 m). The full time series of run-up flow thickness are displayed in Figs. B.3 and B.4.

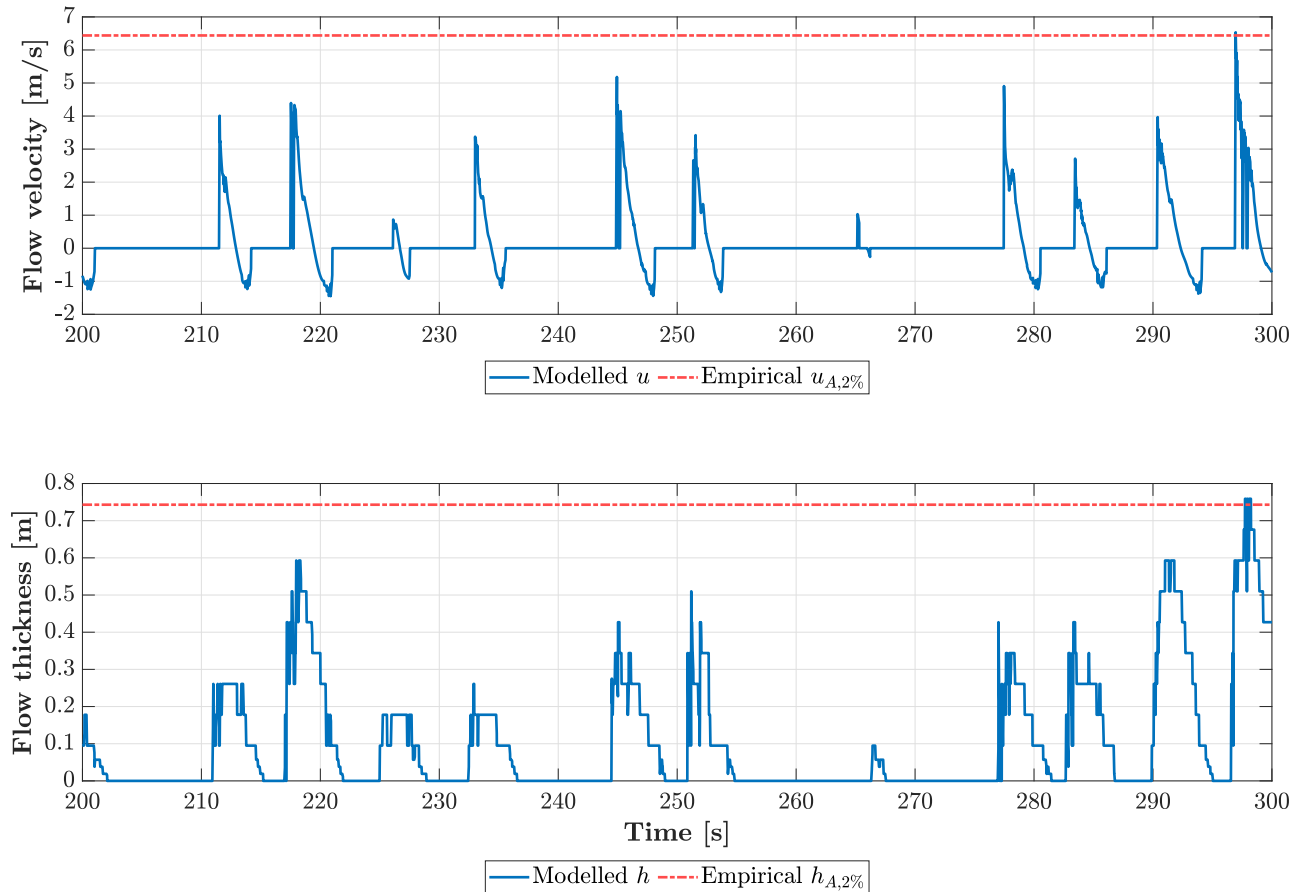
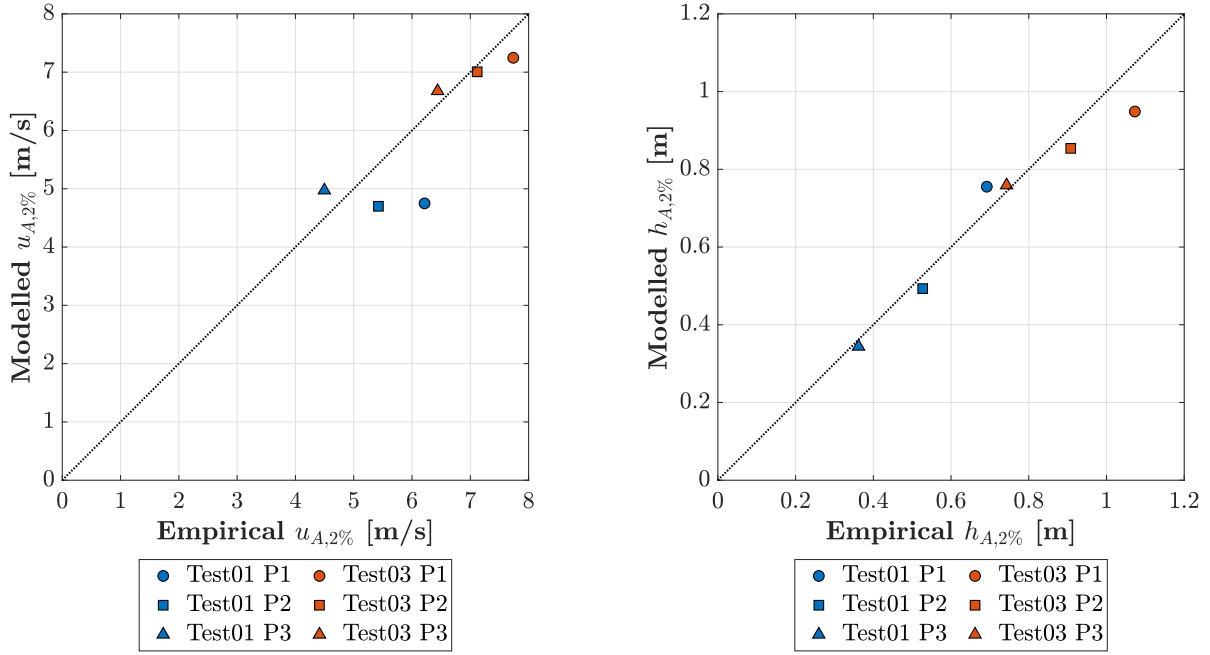


Figure 5.5: Modelled flow velocity and flow thickness between $t = 200 - 300$ s and empirical 2% values according to Schüttrumpf and Oumeraci (2005) at P3 in Test03.



(a) Modelled $u_{A,2\%}$ against empirical $u_{A,2\%}$.

(b) Modelled $h_{A,2\%}$ against empirical $h_{A,2\%}$.

Figure 5.6: Modelled against empirical 2% value of flow thickness $h_{A,2\%}$ and run-up flow velocity $u_{A,2\%}$ on the waterside slope.

5.1.3 Pressure

The modelled pressures have been compared to the measured pressures in the physical test at the location of PS1 (see Fig. 3.2). This has been done to compare the timing of the modelled and physical wave overtopping. Fig. 5.7 shows the modelled and physical pressures between 350 s and 380 s for Test01. Fig. 5.8 shows the modelled and physical pressures between 30 s and 60 s for Test03. The full time series for Test01 and Test03 can be seen in Figs. B.5 and B.6. This shows that the timing of wave overtopping is significantly better for Test03 than for Test01. This could occur due to the lower wave overtopping in Test01, which makes it more difficult for the pressure sensor to measure accurately. The only inaccuracy in Test03 occurs at approximately $t = 92$ s, where a large pressure is simulated, which did not occur in the physical test. Video analysis of Test03 showed that the wave at $t = 92$ s was close to overtopping on the crest, but the wave run-up did not reach the crest. The model overestimated this specific wave, which led to the modelled pressures, but the absence of observed pressures.

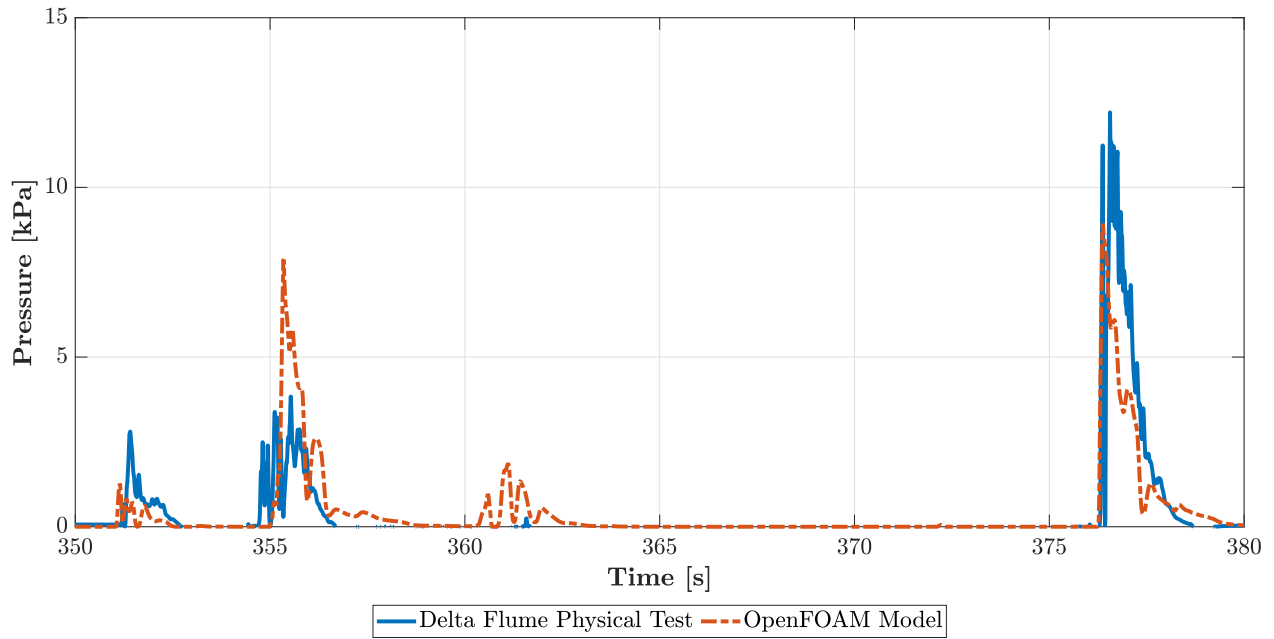


Figure 5.7: Pressure on the dike crest at location of PS1 between $t = 350 - 380$ s in Test01.

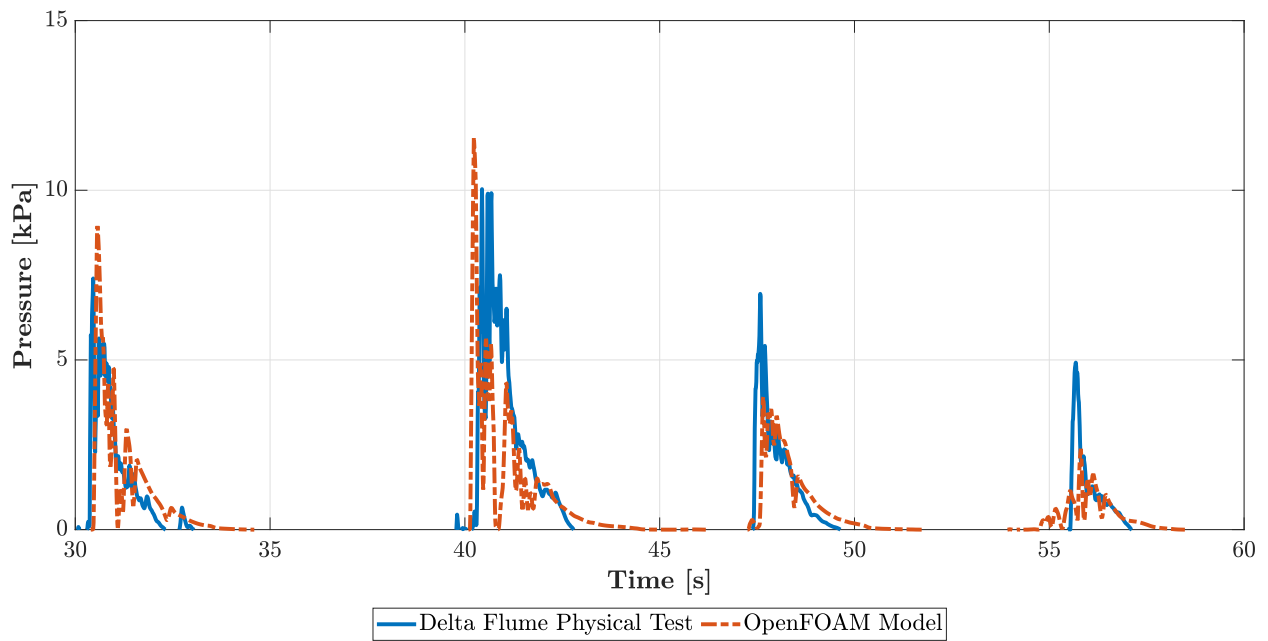


Figure 5.8: Pressure on the dike crest at location of PS1 between $t = 30 - 60$ s in Test03.

5.2 Implementation of block revetments

5.2.1 Calibration

The results of the implementation of the block revetments consist of a calibration and validation phase. In the calibration phase the three different resistance coefficients according to Van Gent (1995); Jensen et al. (2014); Losada et al. (2008) have been simulated using the wave conditions of Test03 between 0 and 170 s. The flow velocity and pressure have been determined on the same locations as in the physical test. Fig. 5.9 shows the flow velocity and the pressure measured at the same location, which is PW1 - PS3. Here it can be seen that the timing and the magnitude of the flow velocity of the overtopping waves are approximated well by all three model runs. The modelled pressures correlate accurately with the modelled flow velocities. This figure also shows the inaccuracies in the observed pressures, with peaks in flow velocities at approximately 150 s and 163 s, but no peak in the pressures. The full time series of the flow velocity results of the calibration are displayed in Figs. C.1 and C.2 and the pressure sensors results in Figs. C.3 to C.6.

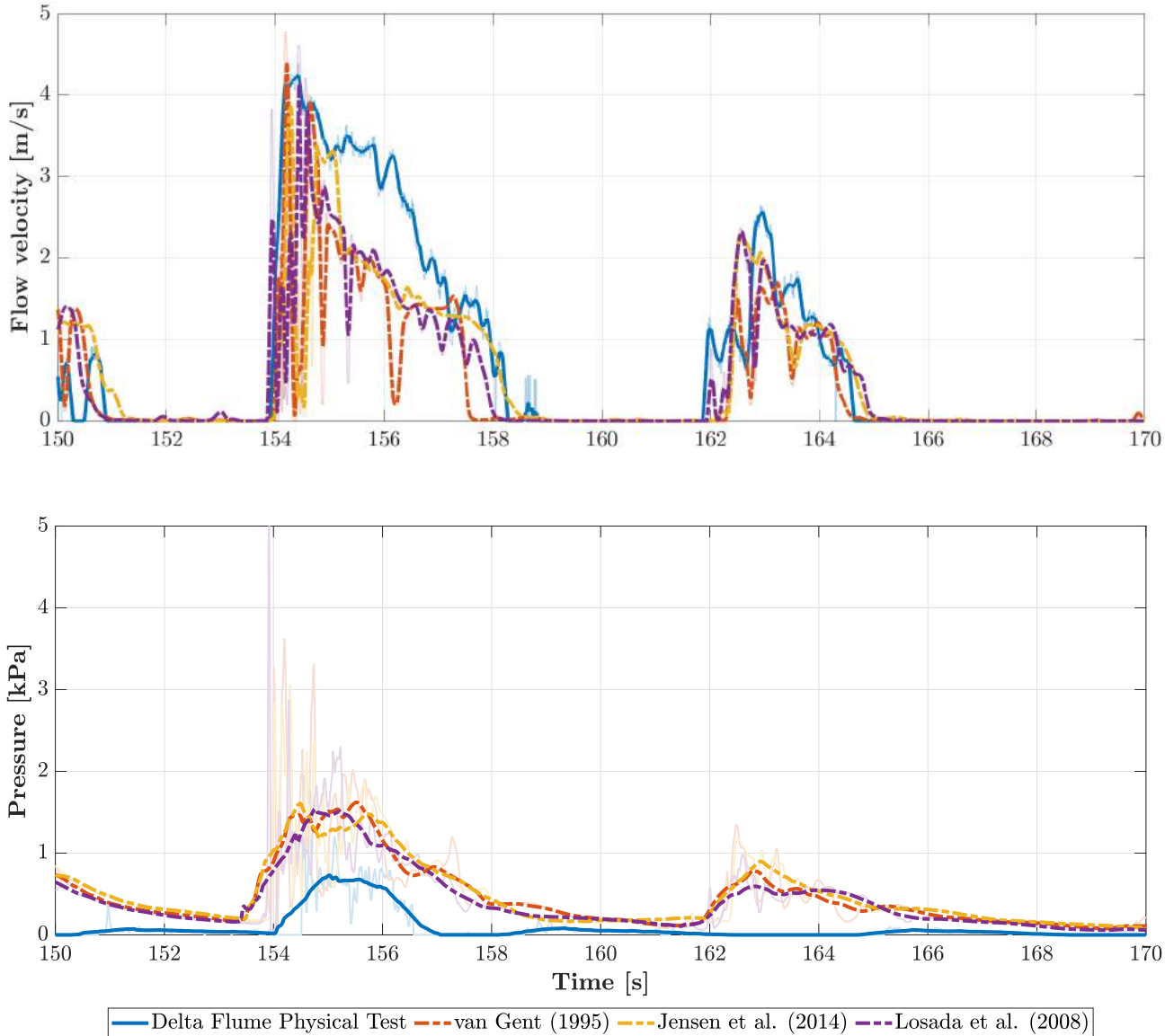
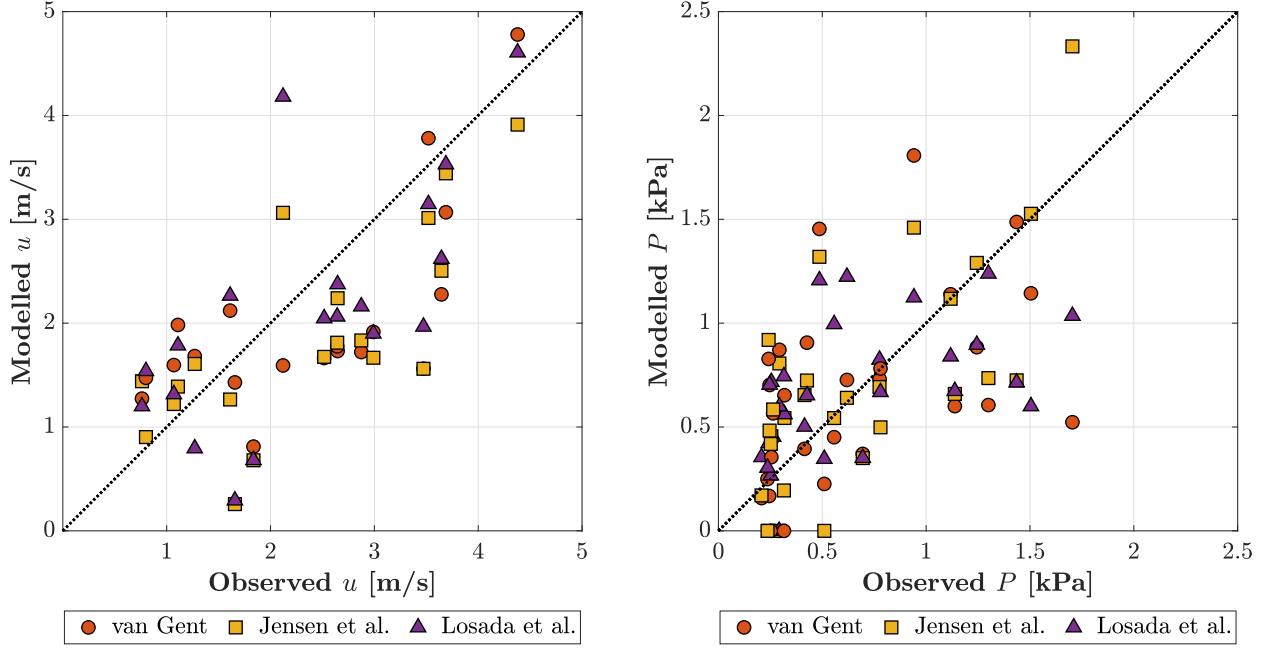


Figure 5.9: Flow velocity at PW1 and pressure at PS3 between $t = 150 - 170$ s in Test03 using resistance coefficients of Van Gent (1995); Jensen et al. (2014); Losada et al. (2008). Data of flow velocity has been moving-averaged over a window of 0.1 s and pressure over 1 s, faded lines represent the original data.

Fig. 5.10 shows the one-to-one comparison of the modelled peak flow velocities and peak pressures per overtopping wave during the calibration from $t = 0 - 170$ s in Test03. The peak flow velocities are measured by PW1 and PW2, whereas the peak pressures have been measured by PS2 - PS5. Fig. 5.10a shows that the three different resistance coefficients sets of Van Gent (1995); Jensen et al. (2014); Losada et al. (2008) all have similar performances. This can also be seen in the performance indicators of Table 5.2, where the NSE and RMSE all perform relatively equal. As can be seen in Fig. 5.10b, the modelled pressures are less accurate than the modelled flow velocities. Table 5.3 shows that Jensen et al. (2014) (NSE = 0.266) and Losada et al. (2008) (NSE = 0.225) both performed reasonably well, whereas Van Gent (1995) has trouble in modelling the pressures of the overtopping waves. A possible explanation is the inaccuracies in the measurements of the physical test. As displayed in Fig. 5.9 the OpenFOAM model predicts high pressures and flow velocities around 164 s, while the physical measurements

only show a peak in the flow velocity and no pressure was measured. These inaccurate pressure measurements have therefore influenced the performance indicators (NSE and RMSE) of the calibration and validation phase of this research. Due to the lesser amount of pressure peaks, the sample size for calibration was reduced.



(a) Modelled peak u [m/s] against observed peak u [m/s] of PW1 and PW2. (b) Modelled peak P [kPa] against observed peak P [kPa] of PS2 - PS5.

Figure 5.10: Modelled against observed peak flow velocity u and peak pressure P per overtopping wave during $t = 0 - 170$ s in Test03.

Table 5.2: Performance indicators of u .

Model	NSE	RMSE
Van Gent (1995)	0.332	0.874
Jensen et al. (2014)	0.315	0.885
Losada et al. (2008)	0.299	0.895

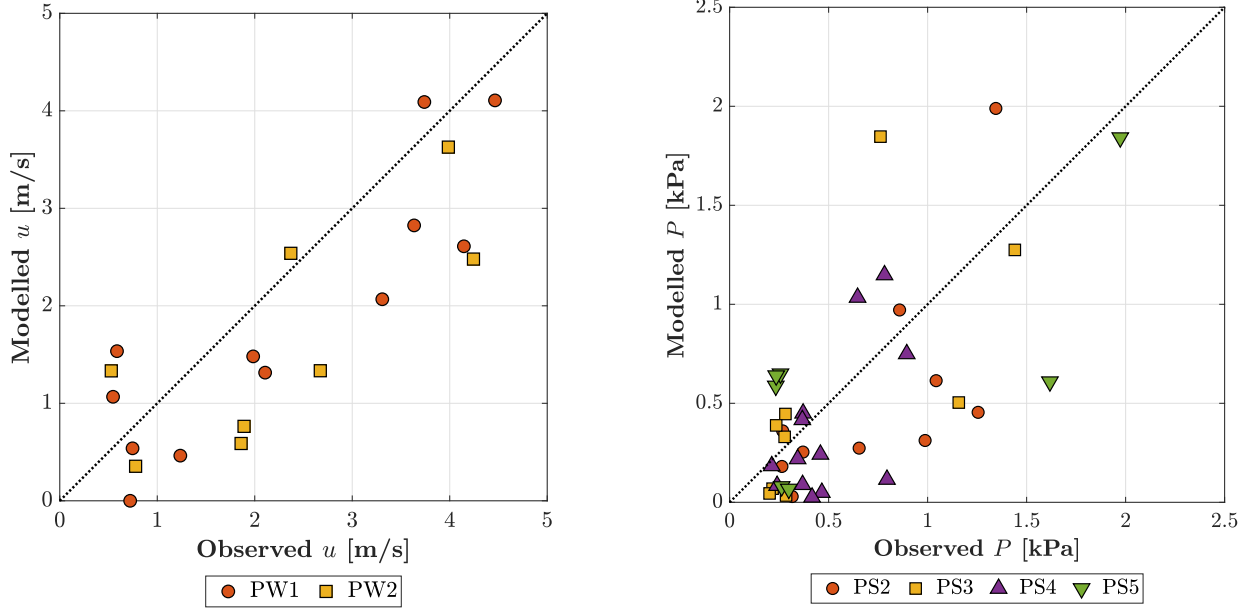
Table 5.3: Performance indicators of P .

Model	NSE	RMSE
Van Gent (1995)	-0.024	0.452
Jensen et al. (2014)	0.266	0.382
Losada et al. (2008)	0.225	0.393

5.2.2 Validation

Fig. 5.11 shows the one-to-one comparison of the modelled peak flow velocities and peak pressures per overtopping wave during the validation from $t = 170 - 350$ s in Test03 using resistance coefficients of Jensen et al. (2014) ($\alpha = 500, \beta = 2.0$). The modelled peak flow velocities are more accurate for PW1 (NSE = 0.681) than for PW2 (NSE = 0.502) (Table 5.4). With a total NSE of 0.606 the peak flow velocities are predicted accurately. The difference between the modelled and measured pressure is larger compared to the flow velocities with an NSE of 0.125 (Table 5.5). Furthermore, there is quite some variation between the pressure sensors, varying from -1.192 to 0.472. The model works well for the pressure of PS5, which is close to

the location of interest (toe of landward slope). The full time series of the flow velocities in Test03 are displayed in Figs. D.1 and D.2 and the pressures of Test03 in Figs. D.3 to D.6. The pressures of Test01 are displayed in Figs. D.7 to D.10



(a) Modelled u [m/s] against observed u [m/s].

(b) Modelled P [kPa] against observed P [kPa].

Figure 5.11: Modelled against observed peak flow velocity u and peak pressure P per overtopping wave during $t = 170 - 350$ s in Test03 using $\alpha = 500$ and $\beta = 2.0$.

Table 5.4: Performance indicators of u .

Sensor	NSE [-]	RMSE [-]
PW1	0.681	0.817
PW2	0.502	1.072
Total	0.606	0.935

Table 5.5: Performance indicators of P .

Sensor	NSE [-]	RMSE [-]
PS2	-0.251	0.443
PS3	-0.023	0.382
PS4	-1.192	0.312
PS5	0.546	0.472
Total	0.154	0.411

5.3 Hydrodynamic conditions on block revetments

Fig. 5.12 shows the flow velocity, shear stress, flow thickness and pressure measured at the location where damage occurred, which is at the toe of the landward slope. The flow parameters of the five largest peaks have been collected from these figures (Table 5.6).

Here it can be seen that at 300 s, the flow velocity is the second largest during the test with $u = 3.65$ m/s. The largest peak occurs at 220 s with $u = 3.76$ m/s. The largest shear stress occurs at 300 s, with $3.23 \times 10^{-2} \text{ m}^2/\text{s}^2$. The measured pressures show a clear peak at 300 s with 5.07 kPa. The second largest peak in pressure occurs at 155 s and is 2.67 kPa. This can also be seen in the flow thickness, which is largest at 300 s and second largest at 155 s.

This shows that at 300 s especially the pressure is larger than in other peaks in Test03. This is caused by the relatively high flow velocity and flow thickness occurring at the same time. The high flow velocities result in high dynamic pressures ($p_d = \frac{1}{2}\rho|\mathbf{u}|^2$) and the large flow thickness in high static pressures ($p_s = \rho gh$). These pressures combined result in a relatively large total pressure ($p_0 = p_s + p_d$), which exceeded the limit state of the Grassblock revetments.

Table 5.6: Peak flow characteristics for Grassblock in Test03 with the time t , flow velocity u , shear stress τ_s , flow thickness h and pressure P .

t [s]	u [m/s]	τ_s [m^2/s^2]	h [m]	P [kPa]
43	1.97	5.45×10^{-3}	0.31	0.83
155	2.87	8.09×10^{-3}	0.37	2.67
220	3.76	9.67×10^{-3}	0.25	1.35
246	2.36	2.10×10^{-2}	0.17	1.22
300	3.65	3.23×10^{-2}	0.41	5.07

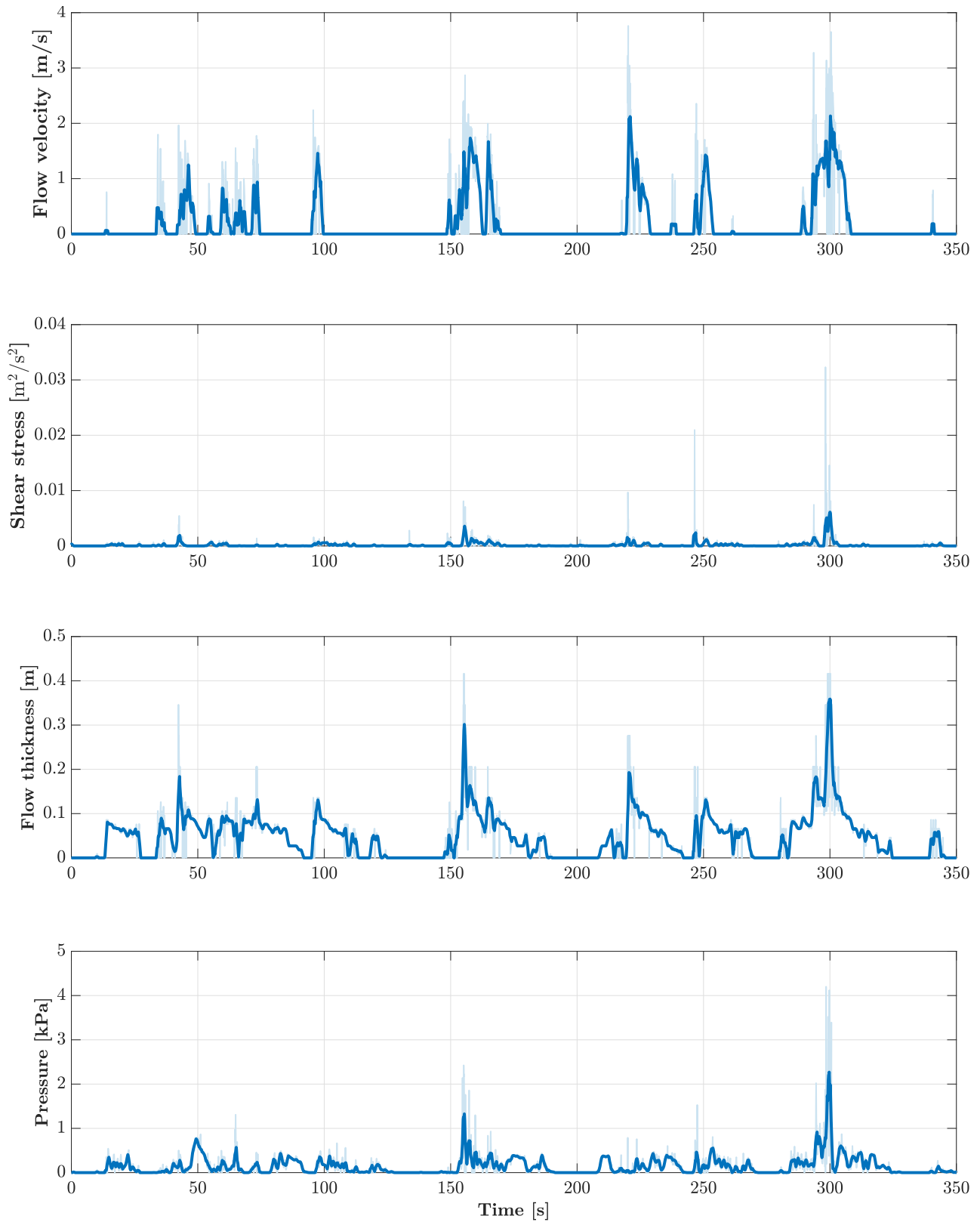
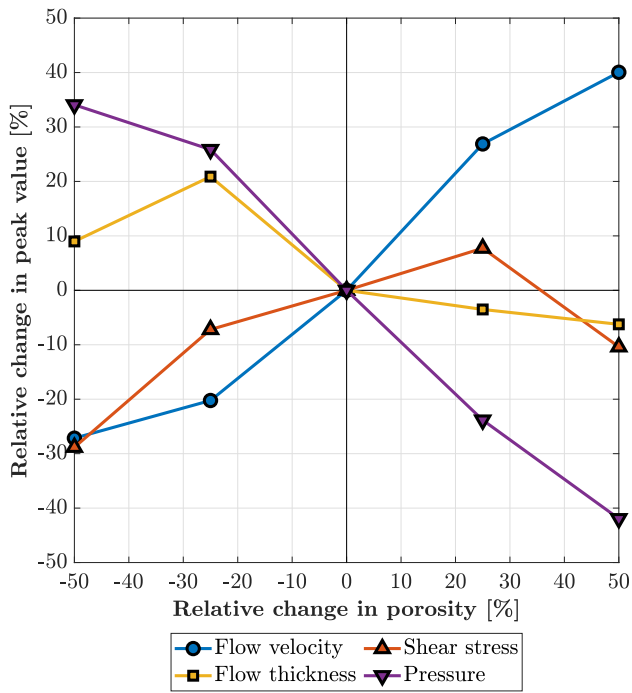


Figure 5.12: Modelled flow velocity, shear stress, flow thickness and pressure at toe of landward slope ($X = 200.79$ m, $Z = 6.2$ m) using Grassblocks during Test03. Data has been moving-averaged over a window of 1 s, faded lines represent the original data.

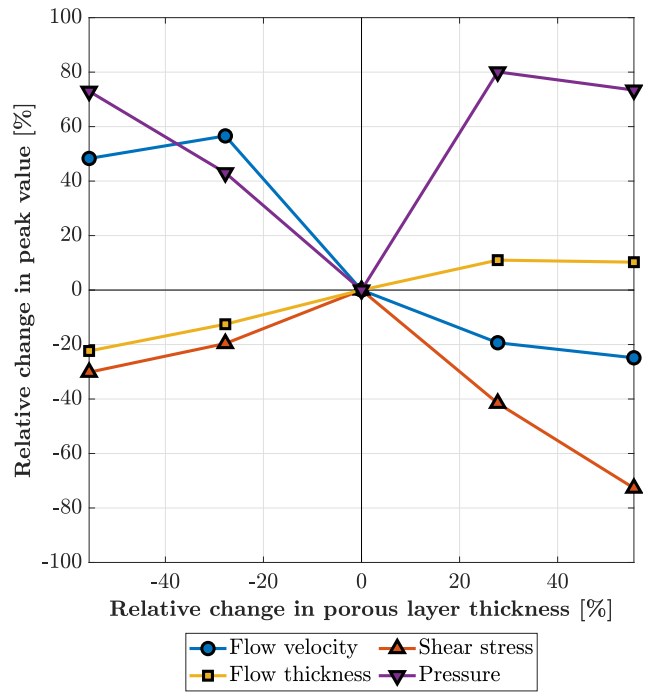
5.3.1 Sensitivity analysis of block revetment properties

The results of the porosity based sensitivity analysis are displayed in Figs. 5.13a and 5.14 using $n = 0.2$ up to $n = 0.6$. The peak flow velocity at approximately $t = 300$ s shows to be dependent on the porosity, where the peak flow velocity increases as the porosity increases. Furthermore, at a higher porosity the peak flow velocity occurs earlier than for a lower porosity. This can be explained by the water flowing faster through the porous layer at a higher porosity, which leads to the water reaching the toe of the landward slope earlier. The same effect also occurs in the shear stress, which is largely dependent on the flow velocity. The flow thickness decreases when the porosity increases. The only outlier in this case is $n = 0.3$, which has a larger flow thickness than $n = 0.2$. The pressure time series shows a large dependency on the porosity. Increasing the porosity leads lower peak pressures. As mentioned in Fig. 5.14, the pressure has been the most influential hydrodynamic condition on the block revetments. Therefore, the stability of the blocks can be improved by increasing the porosity of the block revetments.

The results of the sensitivity analysis based on the thickness of the porous layer using 16, 26, 36, 46 and 56 mm are displayed in Figs. 5.13b and 5.15. The flow velocity time series shows that the peak flow velocity decreases when the thickness of the porous layer increases. Increasing the porous layer thickness leads to more porous volume, which therefore can give more resistance to larger volumes of water, thus decreasing the flow velocity. The opposite effect occurs for the overtopping flow thickness, which increases as the porosity increases. However, this is influenced by a small amount of water that stays at the impermeable bottom of the landward slope in the model. This can be seen after the overtopping wave at approximately 310 s, where a certain layer of water remains and has been further explained in Chapter 6. Noticeable in the pressure time series is that the current porous layer thickness showed the smallest peak pressures. The porous layer thickness of 0.26 m caused the second highest peak pressure, whereas the other three porous layer thicknesses all performed equal.



(a) Relative change in peak values of the hydrodynamic conditions [%] against the relative change in porosity n [%] compared to the default $n = 0.4$.



(b) Relative change in peak values of the hydrodynamic conditions [%] against the relative change in porous layer thickness [%] compared to the default 36 mm.

Figure 5.13: Relative change in peak values of the hydrodynamic conditions [%] against the relative change in porosity n and porous layer thickness [%]. The peak values are based on the moving averaged time series between 290-310 s, as displayed in Figs. 5.14 and 5.15

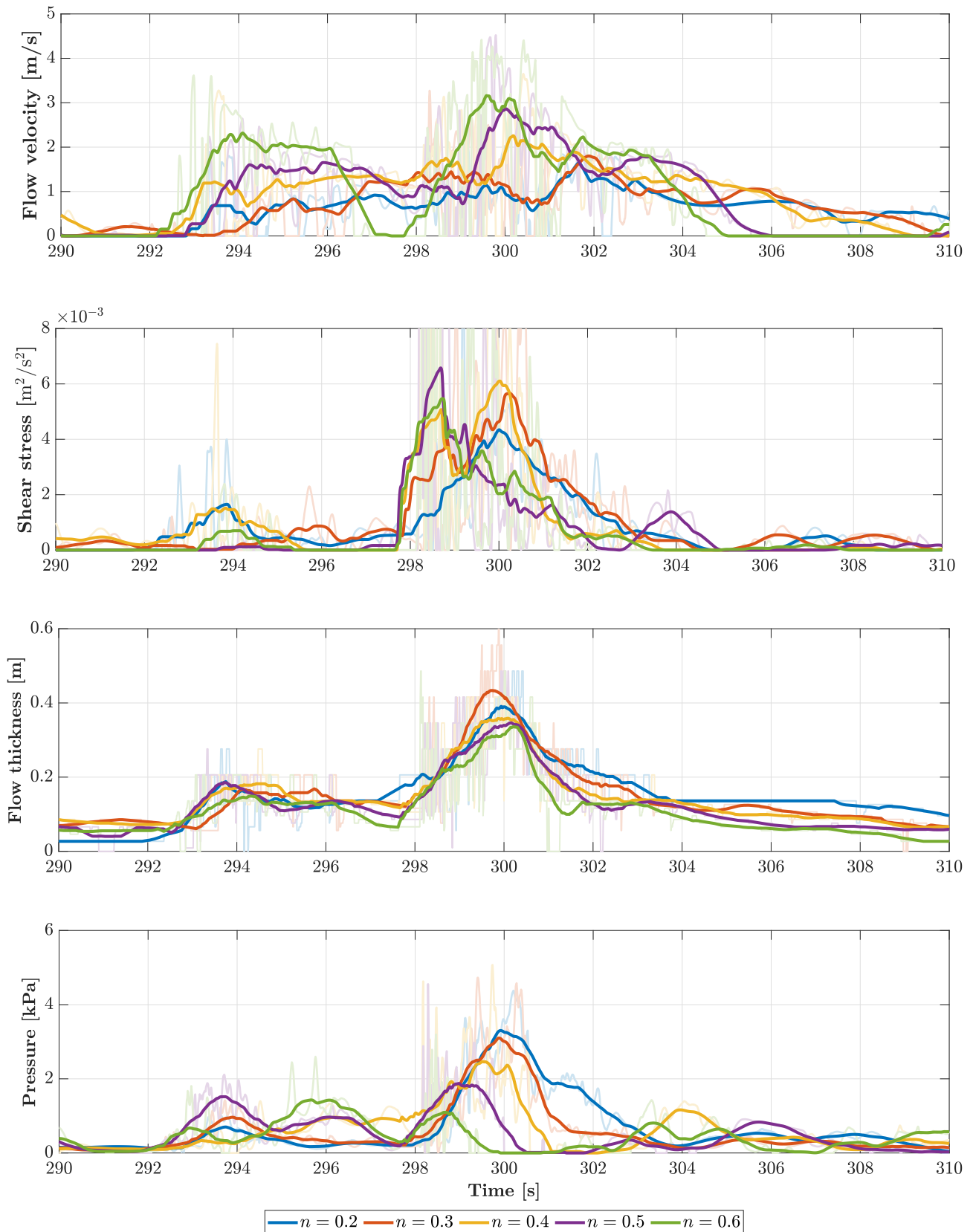


Figure 5.14: Modelled flow velocity, shear stress, flow thickness and pressure at toe of landward slope ($X = 200.79$ m, $Z = 6.2$ m) between $t = 290 - 310$ s in Test03 using various values of the porosity n . Data has been moving-averaged over a window of 1 s, faded lines represent the original data.

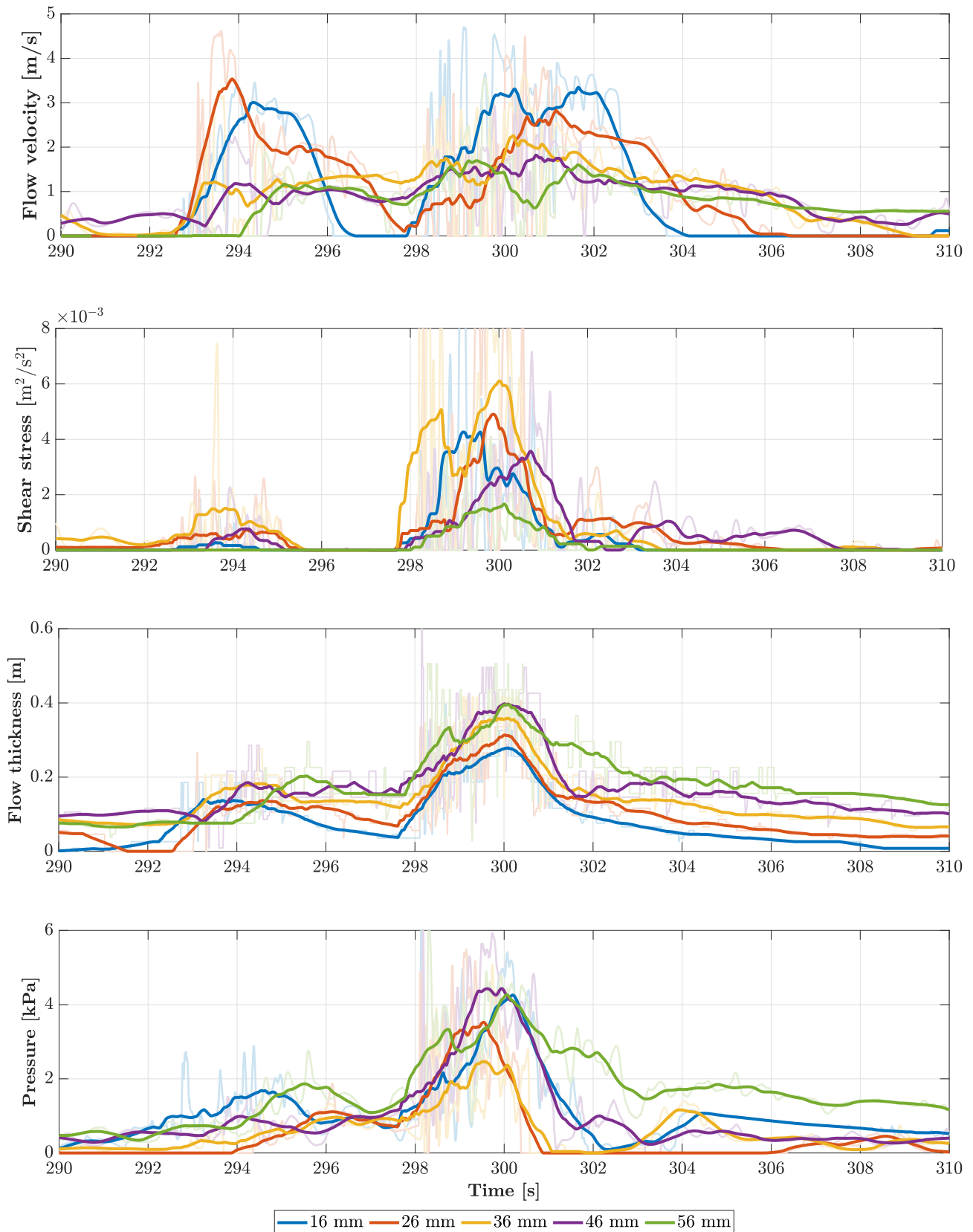


Figure 5.15: Modelled flow velocity, shear stress, flow thickness and pressure at toe of landward slope ($X = 200.79 \text{ m}$, $Z = 6.2 \text{ m}$) between $t = 290 - 310 \text{ s}$ in Test03 using various porous layer thicknesses. Data has been moving-averaged over a window of 1 s, faded lines represent the original data.

6 | Discussion

6.1 Physical Test Data

The measurements of the overtopping flow as done in the physical test at the Delta flume have proven to be difficult. Initially data of four different tests has been provided, which would be a sufficiently large dataset for calibration and validation of the model. However, early in the research it already showed that Test02a and Test02b could not be used due to non-matching modelled and observed time series of free surface elevation. Cross-correlation analysis between the modelled and observed time series of free surface elevation showed no correlation between the physical and modelled time series. This can be explained by the technical issues with the wave generator. Therefore, from this part of the research only the data of Test01 and Test03 could be used.

However, the flow velocity data of Test01 (Fig. 6.1) shows unrealistic results. Most of the peak flow velocities are only around 0.05 m/s, which is unrealistically low for water flowing down the landward slope. Furthermore, there are a few relatively larger, but still quite small peaks of 0.28 m/s at $t = 315$ s and 0.17 m/s at $t = 377$ s. However, what is noticeable on this figure is the non-correlation of the observed pressures and flow velocities. It shows that not all flow velocity peaks coincide with an increase in pressure. Therefore, this led to the conclusion that the flow velocities of Test01 are not sufficiently reliable to be used for model calibration and validation.

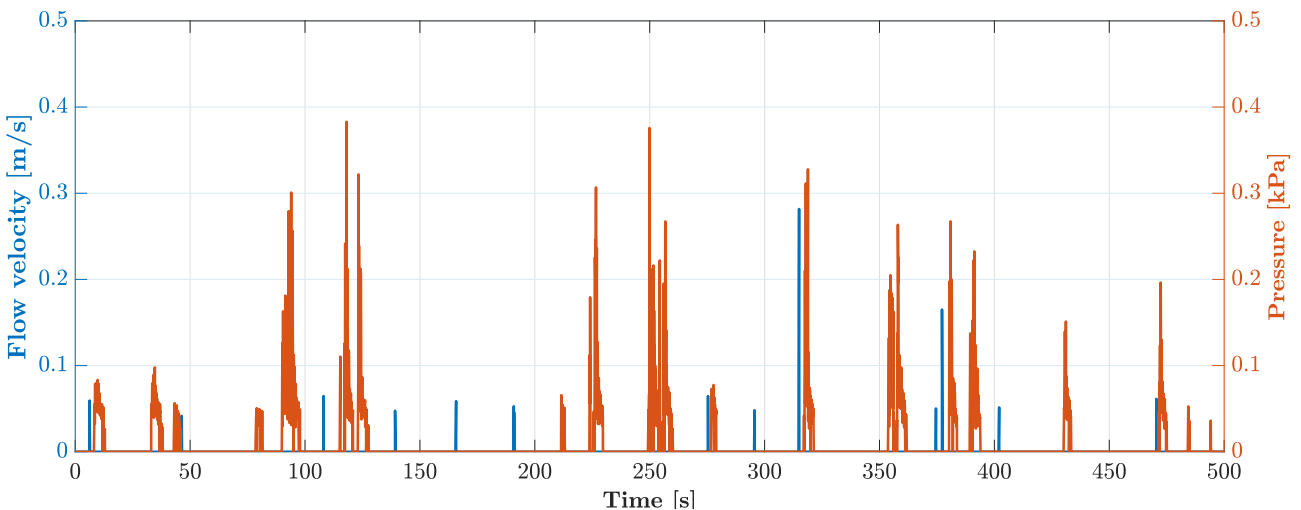


Figure 6.1: Observed flow velocity at PW1 (blue) and observed pressure at PS3 (red) between $t = 0 - 500$ s in Test01.

The inaccurate measurements in Test01 can be influenced by the wave overtopping volume. As displayed in Table 3.2, the specific overtopping discharge q in Test01 was 9.31/s/m. In Test02B the specific discharge was already 2.5 times as high with $q = 23.21$ /s/m. As displayed in Fig. 6.2, the flow velocities in this test are more realistic with values above 1 m/s and correlated to peaks in the pressure. This shows that the installed paddle wheels require a certain minimum flow thickness to function well. This is also because the paddle wheel is installed at 27 mm above the top of the Grassblocks (see Section 3.3).

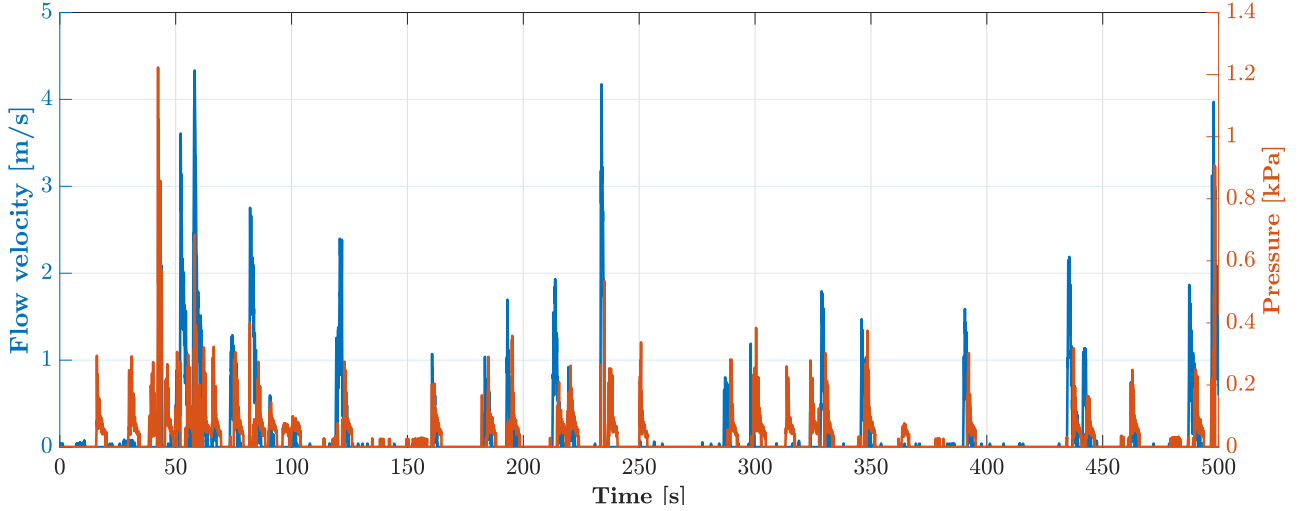


Figure 6.2: Observed flow velocity at PW1 (blue) and observed pressure at PS3 (red) between $t = 0 - 500$ s in Test02B.

This means that only the test data of Test03 could be fully used, besides the pressures of Test01. Although Test03 is the most important test where the block revetments reached its limit, it is unfortunate that the wave conditions of Test01 and Test02 could not be fully assessed in the model. This would have increased the confidence in the applicability of the model in other wave conditions.

6.2 Methodology

Because a model is a simplification of reality, certain assumptions have to be made. For computational benefits the model has been set up as an 2D-vertical model. In the physical test, the walls of the Delta flume create friction, which leads to 3D effects (Xie et al., 2019). This means that the flow velocity in the middle of the flume is larger than near the walls of the flume. The 2D-vertical model represents the middle of the flume, the location with the least wall friction. However, the measurement equipment has been installed 30 cm from the wall of the flume. This causes a timing and magnitude difference between the model output and physical test data. By installing the measuring equipment in the middle of the flume, the effect of wall friction is minimized. In the model wall friction from the side walls also does not occur, therefore it would be expected that this would improve the timing and magnitude of the modelled and observed data.

Table 3.2 also shows the specific wave overtopping discharges, which have been measured in the physical test. These values could have been used as further validation of the model by measuring the modelled wave overtopping discharge. However, the choice has been made to not

do this, because these specific wave overtopping discharges are averaged over the whole test period. The physical test of e.g. Test01 took 4183 s, which would have taken approximately 17 days to simulate, which is not feasible for this research.

Another assumption is the surface below the block revetments. In the physical test, the blocks are installed on a geotextile filter layer which is located on the subsoil (Fig. 2.4). In the OpenFOAM model the infiltration of the overtopping water into the dike has not been implemented. The additional calibration of the porosity and resistance coefficients of the filter layer, clay layer and sand layer would be too complex and computationally expensive for this research goal. Therefore, the porous block revetments in OpenFOAM are installed on the same type of surface as of the waterside slope, which is concrete. Although this concrete surface in OpenFOAM is impermeable, the geotextile filter layer as used in the physical test also has a low permeability with a hydraulic conductivity of 0.07 m/s at 20 °C (see Appendix I). Thus, although there is a difference in permeability between the physical and the modelled dike cover, it is a feasible approximation within this research. A follow-up research could implement this infiltration in the dike to assess the effect of the permeability of the dike.

The porous zone has a depth of 36 mm, which is the same height as the open top part of the Grassblocks (see Appendix G). This has been done to only implement the porous part of the Grassblocks as a porous layer in OpenFOAM. Furthermore, the porosity of $n = 0.4$ has been based on the ratio of void volume out of the total volume on the upper 36 mm of the Grassblock.

The resistance coefficients sets have been determined based on significant studies on this topic. Using these three different researches of Van Gent (1995); Jensen et al. (2014); Losada et al. (2008) gives a range for α and β . The resistance coefficients could have been further calibrated. However, this would be very time consuming in this already time demanding research. Therefore the choice has been made to run three simulations based on these three different sets of resistance coefficients.

6.3 Performance of the model

The results of Section 5.1 showed that the simulation of higher frequency waves is most difficult for the OpenFOAM model. This is also visible when we zoom in on the free surface elevation as plotted in Figs. 5.1 and 5.2. Here the data of the physical test shows very small changes in surface elevation within a wave. The OpenFOAM model does not model these small bumps in surface elevation and has a more general approximation. However, these minor changes in surface elevation have no significant influence on the wave propagation and wave overtopping. The peaks and the period of the surface elevation are most important and these are approximated well.

Although most of the overtopping waves in Test01 are predicted well, there are some inaccuracies in the timing of the modelled pressures. A probable cause of this is the measurement equipment. The pressure sensors have shown to be sensitive to the flow thickness and get less accurate at smaller flow thicknesses. In Test01 there was less wave overtopping, both in frequency and overtopping volume, resulting in less accurate pressure measurements. This is especially proven in Test03, where there was more wave overtopping and the pressure sensors functioned well. The results showed that the model performed best for Test03, which has the largest overtopping volumes.

In the results of Section 5.2, the modelled peak pressures showed less agreement with the measurements compared to the modelled flow velocities. A possible explanation is the inaccuracies in the measurements of the physical test. As displayed in Fig. 5.9 the OpenFOAM model predicts high pressures and flow velocities around 164 s, while the physical measurements only show a peak in the flow velocity and no pressure was measured. These inaccurate pressure measurements have therefore influenced the performance indicators (NSE and RMSE) of the calibration and validation phase of this research. Due to the lesser amount of pressure peaks, the sample size for calibration and validation was reduced, which was already significantly reduced due to Test02a and Test02b and the flow velocities of Test01 not being usable.

The determination of the forces at the moment and location where damage occurred, showed plausible flow conditions. This also proved the main applicability of the model, which is determining the forces on each location and time frame. The sensitivity analysis for porosity values showed that the porosity of $n = 0.6$ performed best. This coincides well with a sensitivity analysis on the porosity by Ren et al. (2014), which showed that the effective value of porosity for a submerged breakwater is in the range from $n = 0.4$ to 0.8. However, it should be noted that the range of porosity in the sensitivity analysis of this research was from 0.2 to 0.6, leaving out porosity values larger than 0.6.

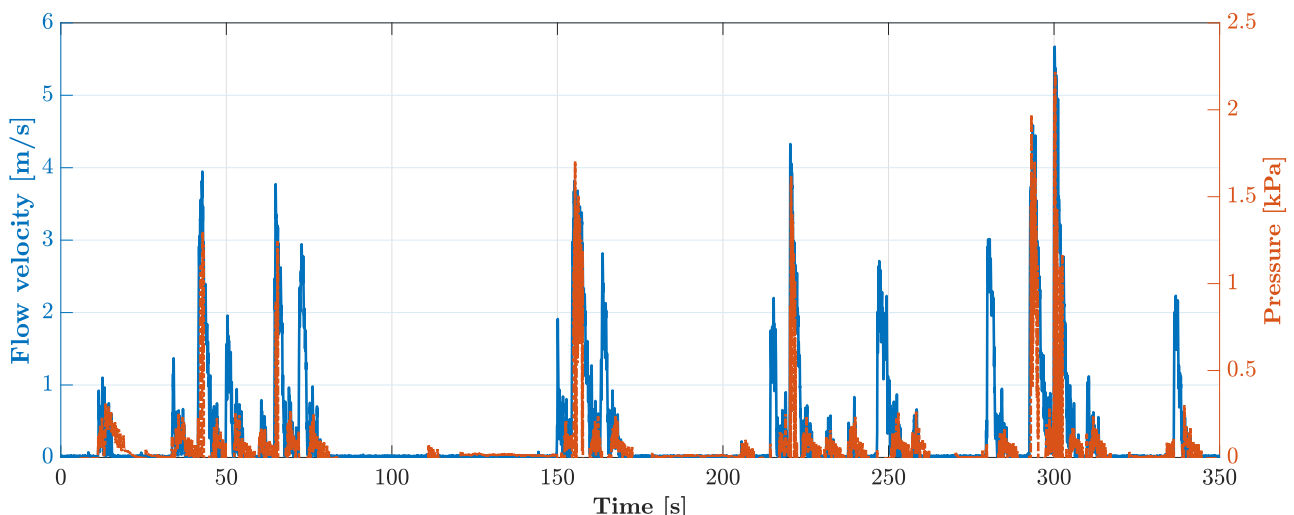


Figure 6.3: Observed flow velocity at PW2 (blue) and observed pressure at PS5 (red) between $t = 0 - 350$ s in Test03.

6.4 Application of the model

The model can be used to assess the different kinds of flow characteristics on each location on the slope over time. This can give more insight into which flow characteristics are the dominant factor. Furthermore, the dike geometry of the model can be adapted quite easily, assuming that the user has OpenFOAM experience. This can then be used to assess the effect of a different waterside slope, crest width or landward slope of the dike. Furthermore the wave conditions can be adjusted to determine how this affects the flow over the waterside slope, crest and landward slope.

The porous layer can also be used to represent other types of block revetments, although the flow over these blocks depend on the grading and shape of the permeable material (Jacobsen

et al., 2018). This could therefore require a calibration of the resistance coefficients α and β . However, the resistance coefficients of Jensen et al. (2014) have proven to function for different kinds of flow regimes and could be widely applicable.

Using the model, the hydrodynamic conditions on the dike cover can be determined. These hydrodynamic loads are important for two types of dike failure; erosion of the dike cover and block stability. Using the output of the model, the hydrodynamic flow conditions such as overtopping flow velocity (Van Bergeijk et al., 2019) that cause erosion of the dike cover can be determined. Furthermore the model can be used for the design of innovative covers leading to more reduction of the wave overtopping volume (waterside slope) or more erosion resistant covers (landward slope). The designs can be tested in the model and optimal specifications can be determined, which reduces the amount of physical testing and therefore is more time- and cost efficient.

7 | Conclusion

A RANS-based hydrodynamic model has been built using a coupling of waves2Foam and OpenFOAM by implementing the geometry and wave conditions from the physical tests conducted at the Delta flume of Deltares. The porous function of the Grassblocks on the crest and landward slope could be implemented into the model using a porous layer, where the porous function of this layer largely depend on the resistance coefficients α and β . Based on earlier research by Van Gent (1995); Losada et al. (2008); Jensen et al. (2014), different sets of resistance sets have been calibrated using a comparison of the modelled and observed peak flow velocities and pressures, which showed that the resistance coefficients of Jensen et al. (2014) performed best. The calibrated and validated model has then been used to determine the hydrodynamic conditions that led to failure of the block revetments, which showed that the pressure was the most influential hydrodynamic condition at the time of failure. The model has then been used to determine the influence of the porosity or the porous layer thickness on the hydrodynamic conditions, which showed that a porosity of $n = 0.6$ and the porous layer thickness of 36 mm reduced the pressure the most.

1. *How can the wave overtopping over the seaward slope, crest and landward slope be coupled into one hydrodynamic model?*

In this research a model was set up to simulate wave overtopping on the waterside and landward side of a dike. A dynamic coupling was made between the models of Van Bergeijk et al. (2020) and Chen et al. (2021). This part created the basic model set-up which has been expanded further in the research. This model had to be validated to guarantee that the model was set up well. The wave characteristics of the calibrated free surface elevation show that the waves as generated in the physical test are well approximated by the OpenFOAM model. The significant wave heights (mean absolute error of 0.001 m) and spectral wave periods (mean absolute error of 0.118 s) showed good agreement between the physical test and the numerical model.

The 2% values for flow velocity and flow thickness on the waterside slope provided a way to verify the model with empirical formulae. The measured 2% flow velocities (mean absolute error of 0.585 m/s) and 2% flow thicknesses (mean absolute error of 0.052 m) matched relatively well with the empirical values. This provided confidence in the modelled wave run-up over the waterside slope. Using the pressures as measured on the crest, the timing of the wave overtopping could be verified. Especially the results of Test03 were promising, where every overtopping wave from the physical test was captured by the OpenFOAM model. For Test01 the timing of the pressures were less accurately predicted.

Overall, the calibrated surface elevation, significant wave heights, spectral wave periods, 2% flow velocity, 2% flow thickness and the pressures provided a broad and complete insight in the functioning of the first set-up of the model. This provided confidence in the basic set-up of the model and a good foundation for the further research in this project.

2. *To what extent can a 2D vertical hydrodynamic model simulate the flow over a 3D block cover?*

The porous function of the Grassblocks on the crest and landward slope could be implemented into the model using a porous layer, a functionality of the waves2Foam toolbox. The porous function of this layer largely depend on the resistance coefficients α and β . The porous layer proved to be a good tool to simulate the porous function of the block revetments. Although the value of the resistance coefficients are still widely studied (Van Gent, 1995; Losada et al., 2008; Jensen et al., 2014), the comparison of the different resistance coefficients as used in literature provided a good way to calibrate the porous layer.

The measured peak pressures and peak flow velocities from the physical test were used to calibrate the model. Using the modelled peak values for flow velocity and pressure showed that the resistance coefficients of Jensen et al. (2014) delivered the most accurate modelled flow velocity (NSE = 0.315) and pressure (NSE = 0.266) over the block revetments. Noticeable was that the timing of the flow velocity peaks was more accurate than the pressures. This could have occurred due to the accuracy of the measuring equipment. The validation provided confidence in the modelled peak flow velocities (NSE = 0.606) and pressures (NSE = 0.154) based on the resistance coefficients of Jensen et al. (2014).

3. *What are the hydrodynamic conditions leading to failure of the block revetments?*

The determination of the forces at the toe of the landward slope of the dike proved the application of the model, where the flow conditions can be assessed on any location within the domain. This gave insight into the flow conditions that occurred on the time and location that the blocks collapsed. The flow conditions showed that both high flow velocities and large flow thicknesses occurred at 300 s at the toe of the landward slope. The high flow velocities resulted in high dynamic pressures ($p_d = \frac{1}{2}\rho|\mathbf{u}|^2$) and the large flow thickness in high static pressures ($p_s = \rho gh$). These pressures combined resulted in a relatively large total pressure ($p_0 = p_s + p_d$), which exceeded the limit of the blocks.

The sensitivity analysis showed that a higher porosity increases the flow velocity and shear stress and decreases the flow thickness and pressure. The porosity of $n = 0.6$ showed to reduce the peak pressure the most. An increase in the thickness of the porous layer leads to smaller flow velocities and a larger flow thickness. The porous layer thickness of 36 mm resulted in the smallest pressures.

The goal of this research has been

To determine the hydrodynamic conditions on the dike cover caused by the wave run-up on the waterside slope and by the overtopping flow over the crest and landward slope.

The hydrodynamic model has proven to be able to simulate the hydrodynamic conditions along the whole dike cover. Although the peak pressures and flow velocities have proven to be difficult to simulate, the validated model could especially approximate the peak flow velocity (NSE = 0.606) well, whereas the peak pressure (NSE = 0.154) have shown to be approximated reasonably well. The model also proved to be a valuable tool in the design phase of block revetments by assessing which hydrodynamic conditions caused the block revetments to fail. Furthermore, using the model the properties of the block that result in the most reduction of the hydrodynamic conditions such as flow velocity and pressure can be determined.

8 | Recommendations

8.1 3D model

Although the 2D-V model could give quite accurate results, it is still a simplification of the real physical flume test. A 3D model can give more insight in the turbulence and the effect of the block revetments by implementing the 3D blocks into the model. Although the 3D model has more possibilities, a large disadvantage of the 3D model is that it is computationally much more demanding. This would require powerful hardware and a longer project period, because it is not feasible to do such a research in a period of twenty weeks. Furthermore, the grid can be made coarser or the Courant number can be increased to reduce the computational time, although this would result in less accurate simulations.

8.2 Infiltration

This research did not include the infiltration of the run-up and overtopping water into the dike. In this research the bottom of the block revetments has been implemented as a concrete surface, but the whole dike could also be implemented as a porous layer in OpenFOAM. This was outside the scope of this research, but it would be interesting to assess the effect of the wave overtopping on the infiltration of the dike.

8.3 Physical testing

Further physical tests which will be used to calibrate and validate models require very accurate measurements, which can significantly improve the efficiency of the research. In the physical test it can be seen that 3D effects occurred where the water was flowing faster through the middle than near the walls of the Delta flume. Therefore, especially for 2D-V models, the measuring equipment is preferably installed on the center between both flume walls. This reduces the probability of 3D effects, which can increase the accuracy of the physical measurements. Furthermore, it would also be recommended to start the data logging of the measuring equipment at the same time as the wave paddle starts to move. A synchronized starting time for both the wave paddle and the measuring equipment would remove the step of finding the lag time between the modelled and observed test.

8.4 Computational Fluid Dynamics course

Lastly, from my own experiences, a recommendation for the Marine and Fluvial Systems group of the University of Twente would be to implement a Computational Fluid Dynamics based course in the Water Engineering and Management track. The possibilities of CFD are very broad and could have a very significant role in the future design of water engineering. Working with CFD software like OpenFOAM has quite a steep learning curve. If a student has already experienced working with this kind of software, it could significantly ease the start of a research such as a Master research. This would lead to more time that can be used for expanding the research.

Bibliography

- Altomare, C., Crespo, A. J. C., Domínguez, J. M., Gómez-Gesteira, M., Suzuki, T., and Verwaest, T. (2015). Applicability of Smoothed Particle Hydrodynamics for estimation of sea wave impact on coastal structures. *Coastal Engineering*, 96:1–12.
- Bezuijen, A., Klein Breteler, M., and Bakker, K. (1987). Design criteria for placed block revetments and granular filters. *Second International Conference on Coastal and Port Engineering in Developing Countries, Beijing 1987*, pages 1852–1866.
- Burcharth, H. F. and Andersen, O. K. (1995). On the one-dimensional steady and unsteady porous flow equations. *Coastal Engineering*, 24(3-4):233–257.
- Capel, A. (2015). Wave run-up and overtopping reduction by block revetments with enhanced roughness. *Coastal Engineering*, 104:76–92.
- Chen, W., Marconi, A., van Gent, M. R. A., Warmink, J. J., and Hulscher, S. J. M. H. (2020a). Experimental Study on the Influence of Berms and Roughness on Wave Overtopping at Rock-Armoured Dikes. *Journal of Marine Science and Engineering*, 8(6):446.
- Chen, W., van Gent, M. R., Warmink, J. J., and Hulscher, S. J. (2020b). The influence of a berm and roughness on the wave overtopping at dikes. *Coastal Engineering*, 156:103613.
- Chen, W., Warmink, J. J., Van Gent, M. R. A., and Hulscher, S. J. M. H. (2021). Modelling of wave overtopping at dikes using OpenFOAM. *Coastal Engineering 2020*, (36v):10.
- CIRIA; CUR; CETMEF (2007). The Rock Manual. The use of rock in hydraulic engineering (2nd edition). *C683, CIRIA, London*.
- De Winter, R. C., Sterl, A., De Vries, J. W., Weber, S. L., and Ruessink, G. (2012). The effect of climate change on extreme waves in front of the Dutch coast. *Ocean Dynamics*, 62(8):1139–1152.
- Engsig-Karup, A. P., Bingham, H. B., and Lindberg, O. (2009). An efficient flexible-order model for 3D nonlinear water waves. *Journal of Computational Physics*, 228(6):2100–2118.
- Geeraerts, J., Troch, P., De Rouck, J., Verhaeghe, H., and Bouma, J. J. (2007). Wave overtopping at coastal structures: prediction tools and related hazard analysis. *Journal of Cleaner Production*, 15(16):1514–1521.
- Gruwez, V., Altomare, C., Suzuki, T., Streicher, M., Cappiotti, L., Kortenhuis, A., and Troch, P. (2020). Validation of RANS modelling for wave interactions with sea dikes on shallow foreshores using a large-scale experimental dataset. *Journal of Marine Science and Engineering*, 8(9).

- Hu, K., Mingham, C. G., and Causon, D. M. (2000). Numerical simulation of wave overtopping of coastal structures using the non-linear shallow water equations. *Coastal Engineering*, 41(4):433–465.
- Hubbard, M. E. and Dodd, N. (2002). A 2D numerical model of wave run-up and overtopping. *Coastal Engineering*, 47(1):1–26.
- Jacobsen, N. G., Fuhrman, D. R., and Fredsøe, J. (2012). A wave generation toolbox for the open-source CFD library: OpenFoam®. *International Journal for Numerical Methods in Fluids*, 70(9):1073–1088.
- Jacobsen, N. G., van Gent, M. R. A., Capel, A., and Borsboom, M. (2018). Numerical prediction of integrated wave loads on crest walls on top of rubble mound structures. *Coastal Engineering*, 142:110–124.
- Jacobsen, N. G., van Gent, M. R. A., and Wolters, G. (2015). Numerical analysis of the interaction of irregular waves with two dimensional permeable coastal structures. *Coastal Engineering*, 102:13–29.
- Jensen, B., Jacobsen, N. G., and Christensen, E. D. (2014). Investigations on the porous media equations and resistance coefficients for coastal structures. *Coastal Engineering*, 84:56–72.
- Khayyer, A., Gotoh, H., Shimizu, Y., Gotoh, K., Falahaty, H., and Shao, S. (2018). Development of a projection-based SPH method for numerical wave flume with porous media of variable porosity. *Coastal Engineering*, 140:1–22.
- Klein Breteler, M. (2016). Vergelijkend onderzoek zetstenen voor dijken - Samenvattend rapport (in Dutch). Technical report, Deltares, Delft.
- Klein Breteler, M., Provoost, Y., Van Steeg, P., Wolters, G., Kaste, D., and Mourik, G. (2018). Stability comparison of 9 modern placed block revetment types for slope protections. *Coastal Engineering Proceedings 2018*, (36):75.
- Larsen, B. E. and Fuhrman, D. R. (2018). On the over-production of turbulence beneath surface waves in Reynolds-averaged Navier–Stokes models. *Journal of Fluid Mechanics*, 853:419–460.
- Lorke, S., Bornschein, A., Schüttrumpf, H., and Reinhard Pohl, H. (2012). Influence of wind and current on wave run-up and wave overtopping Final report. Technical report.
- Losada, I. J., Lara, J. L., Guanche, R., and Gonzalez-Ondina, J. M. (2008). Numerical analysis of wave overtopping of rubble mound breakwaters. *Coastal Engineering*, 55(1):47–62.
- Mansard, E. P. D. and Funke, E. R. (1980). The measurement of incident and reflected spectra using a least squares method. In *Coastal Engineering 1980*, pages 154–172, New York, NY. American Society of Civil Engineers.
- Menter, F. R. (1993). Zonal two equation κ - ω turbulence models for aerodynamic flows. In *AIAA 23rd Fluid Dynamics, Plasmadynamics, and Lasers Conference, 1993*. American Institute of Aeronautics and Astronautics Inc, AIAA.
- Miquel, A. M., Kamath, A., Chella, M. A., Archetti, R., and Bihs, H. (2018). Analysis of different methods for wave generation and absorption in a CFD-based numerical wave tank. *Journal of Marine Science and Engineering*, 6(2).

- Nash, J. E. and Sutcliffe, J. V. (1970). River flow forecasting through conceptual models part I - A discussion of principles. *Journal of Hydrology*, 10(3):282–290.
- OpenCFD Ltd. (2020). OpenFOAM User Guide. December:169.
- Paulsen, B. T., Bredmose, H., and Bingham, H. B. (2014). An efficient domain decomposition strategy for wave loads on surface piercing circular cylinders. *Coastal Engineering*, 86:57–76.
- Pedersen, J. R., Larsen, B. E., Bredmose, H. ., and Jasak, H. (2017). A New Volume-Of-Fluid Method in Openfoam. *MARINE 2017 Computational Methods in Marine Engineering VII*, pages 266–278.
- Pfister, M. and Chanson, H. (2014). Two-phase air-water flows: Scale effects in physical modeling. *Journal of Hydrodynamics*, 26(2):291–298.
- Ren, B., Wen, H., Dong, P., and Wang, Y. (2014). Numerical simulation of wave interaction with porous structures using an improved smoothed particle hydrodynamic method. *Coastal Engineering*, 88:88–100.
- Schüttrumpf, H. and Oumeraci, H. (2005). Layer thicknesses and velocities of wave overtopping flow at seadikes. *Coastal Engineering*, 52(6):473–495.
- Schüttrumpf, H., Van Der Meer, J., Kortenhaus, A., Bruce, T., and Franco, L. (2009). Wave run-up and wave overtopping at armored rubble slopes and mounds.
- Schüttrumpf, H. and Van Gent, M. R. A. (2003). Wave overtopping at seadikes. In *Coastal Structures 2003 - Proceedings of the Conference*, pages 431–443.
- Stanczak, G., Kortenhaus, A., and Oumeraci, H. (2009). Sea Dikes Breaching Initiated by Breaking Wave Impact. *FLOODsite*.
- Van Bergeijk, V. M., Warmink, J. J., and Hulscher, S. J. M. H. (2020). Modelling the wave overtopping flow over the crest and the landward slope of grass-covered flood defences. *Journal of Marine Science and Engineering*, 8(7):1–30.
- Van Bergeijk, V. M., Warmink, J. J., van Gent, M. R. A., and Hulscher, S. J. M. H. (2019). An analytical model of wave overtopping flow velocities on dike crests and landward slopes. *Coastal Engineering*, 149(October 2018):28–38.
- Van der Meer, J. W. (2002). Technical report wave run-up and wave overtopping at dikes. *Technical Advisory Committee on Flood Defence, Delft, The Netherlands*, page 43.
- Van der Meer, J. W., Allsop, N. W. H., Bruce, T., De Rouck, J., Kortenhaus, A., Pullen, T., Schüttrumpf, H., Troch, P., and Zanuttigh, B. (2018). *EurOtop, 2018. Manual on wave overtopping of sea defences and related structures. An overtopping manual largely based on European research, but for worldwide application.*
- Van Gent, M. R. A. (1995). Porous Flow through Rubble-Mound Material. *Journal of Waterway, Port, Coastal, and Ocean Engineering*, 121(3):176–181.
- Van Gent, M. R. A. (2001). Wave Runup on Dikes with Shallow Foreshores. *Journal of Waterway, Port, Coastal, and Ocean Engineering*, 127(5):254–262.

- Van Gent, M. R. A. (2014). Overview of physical modelling at Deltares, including the new Delta flume. *Coastlab 2014*.
- Van Steeg, P. (2016). Stabiliteit taludbekleding van Hillblock 2.0, Drainageblock en Grassblock (in Dutch). Technical report, Deltares, Delft, the Netherlands.
- Van Steeg, P. (2017). Stabiliteit van Grassblocks op de kruin en het binnentalud van een dijk (in Dutch). Technical report, Deltares, Delft, the Netherlands.
- Van Steeg, P., Klein Breteler, M., and Labrujere, A. (2014). Design of wave impact generator to test stability of grass slopes under wave attack. In *Coastlab 2014*.
- Wilcox, D. (2006). *Turbulence Modeling for CFD*. 3rd edition.
- Windt, C., Davidson, J., Schmitt, P., and Ringwood, J. V. (2019). On the assessment of numerical wave makers in CFD simulations. *Journal of Marine Science and Engineering*, 7(2).
- Xie, N., Hann, M., Pemberton, R., Iglesias, G., and Greaves, D. (2019). A numerical and experimental investigation of the effect of side walls on hydrodynamic model testing in a wave flume. *Ocean Engineering*, 186:106108.

A | Wave characteristics

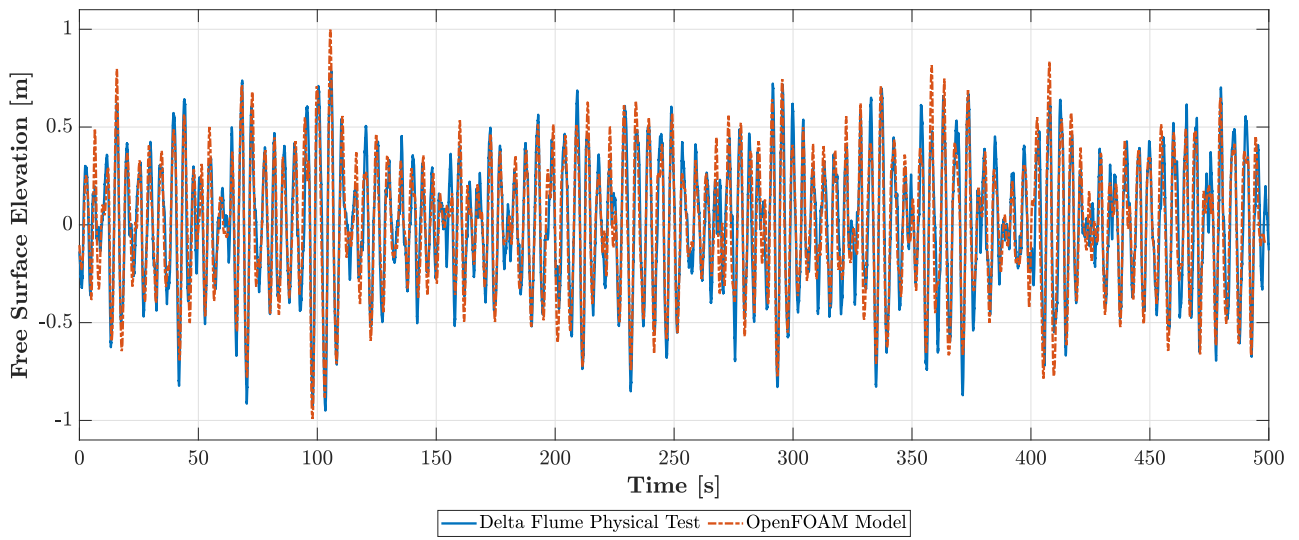


Figure A.1: Free surface elevation of incoming waves at X=108.5 m in Test01.

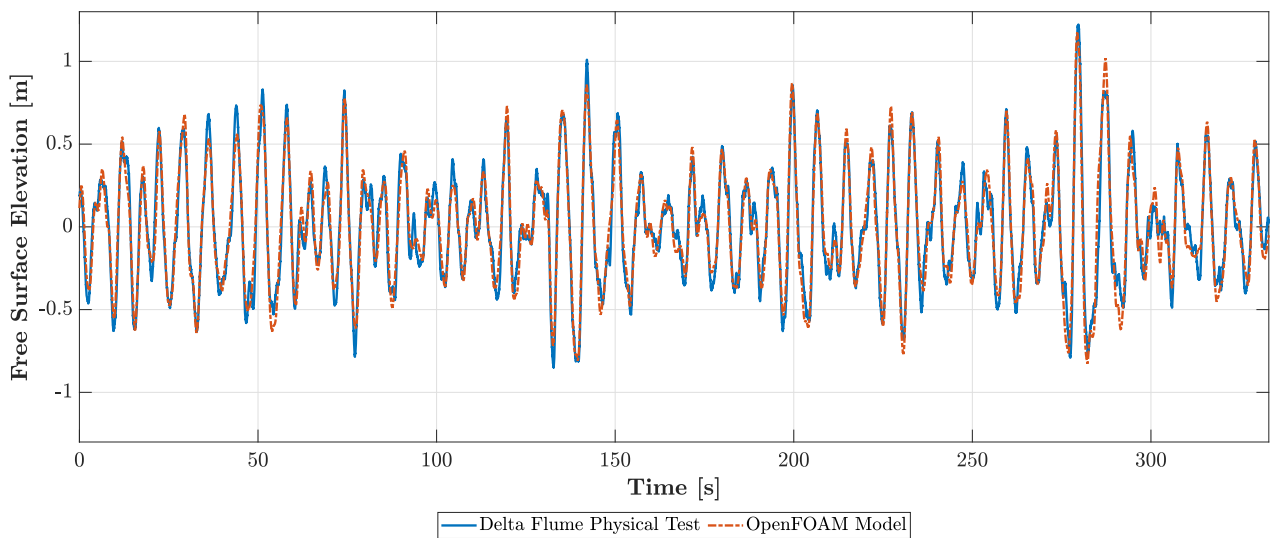


Figure A.2: Free surface elevation of incoming waves at X=108.5 m in Test03.

B | Model validation

Table B.1: Run-up velocity $u_{A,2\%}$ and flow thickness $h_{A,2\%}$ exceeded by 2% of the up-rushing waves calculated at three locations using Eqs. (2.7) and (2.8).

(a) $u_{A,2\%}$ [m/s].				(b) $h_{A,2\%}$ [m].			
	Test #				Test #		
	Test01	Test02	Test03		Test01	Test02	Test03
P1	6.21	6.84	7.74	P1	0.69	0.84	1.07
P2	5.42	6.13	7.12	P2	0.53	0.67	0.91
P3	4.50	5.32	6.44	P3	0.36	0.51	0.74

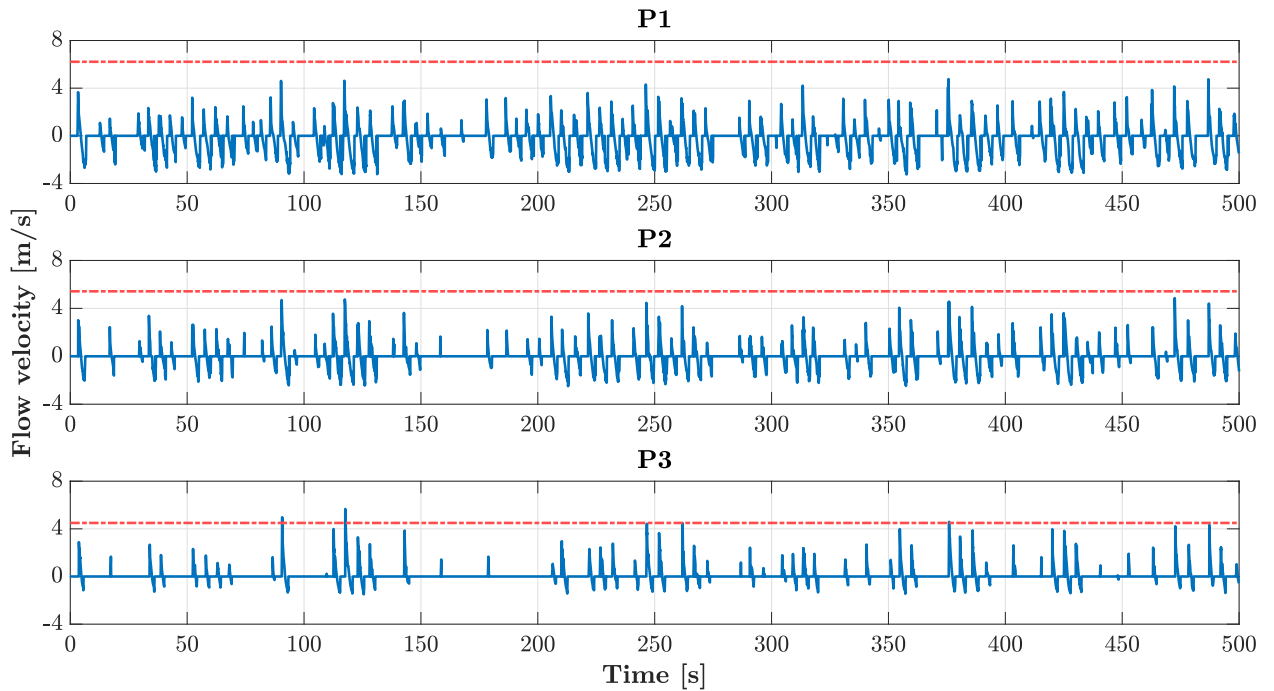


Figure B.1: Run-up flow velocity u [m/s] (blue solid line) and 2% run-up flow velocity $u_{A,2\%}$ (red dash-dot line) along the water side slope measured at three locations P1-P3 in Test01.

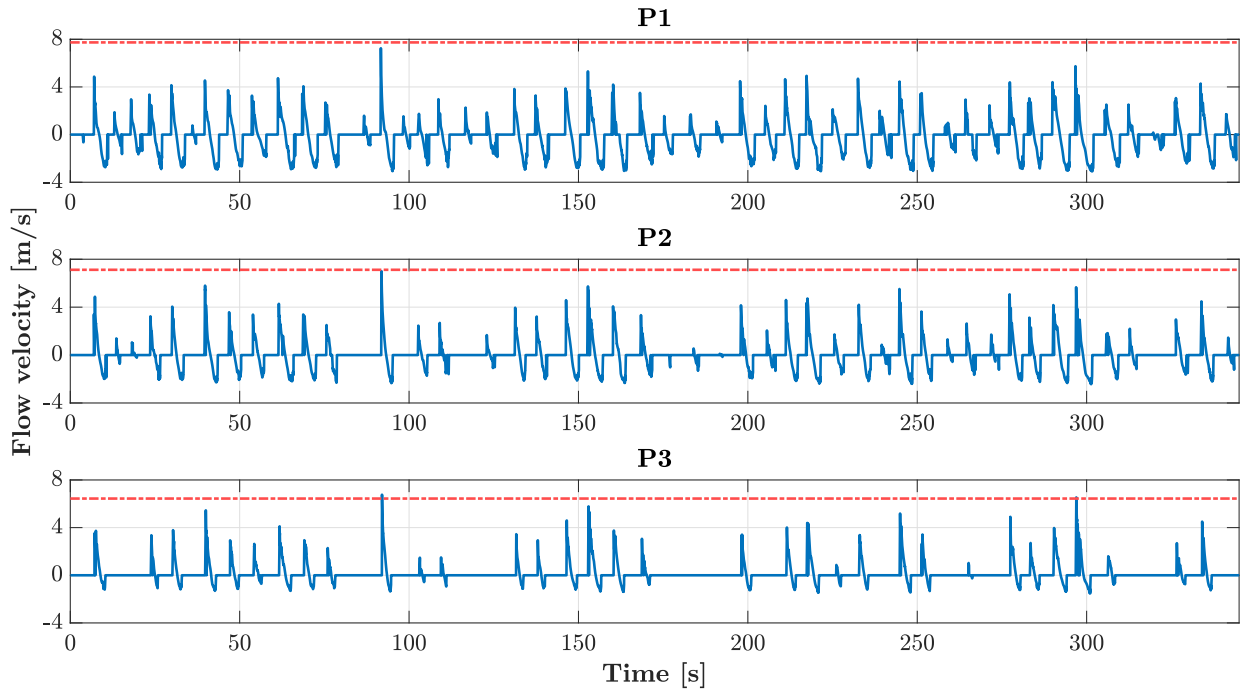


Figure B.2: Run-up flow velocity u [m/s] (blue solid line) and 2% run-up flow velocity $v_{A,2\%}$ (red dash-dot line) along the water side slope measured at three locations P1-P3 in Test03.

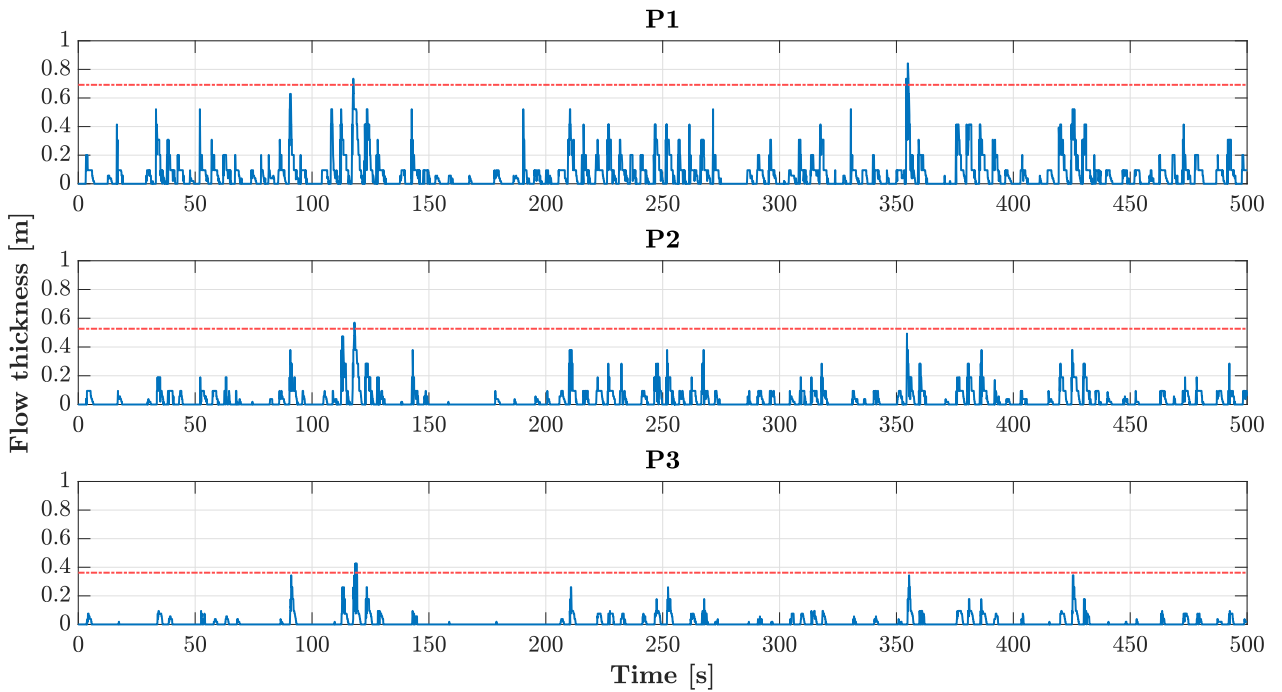


Figure B.3: Run-up flow thickness h [m] (blue solid line) and 2% run-up flow thickness $h_{A,2\%}$ (red dash-dot line) along the water side slope measured at three locations P1-P3 in Test01.

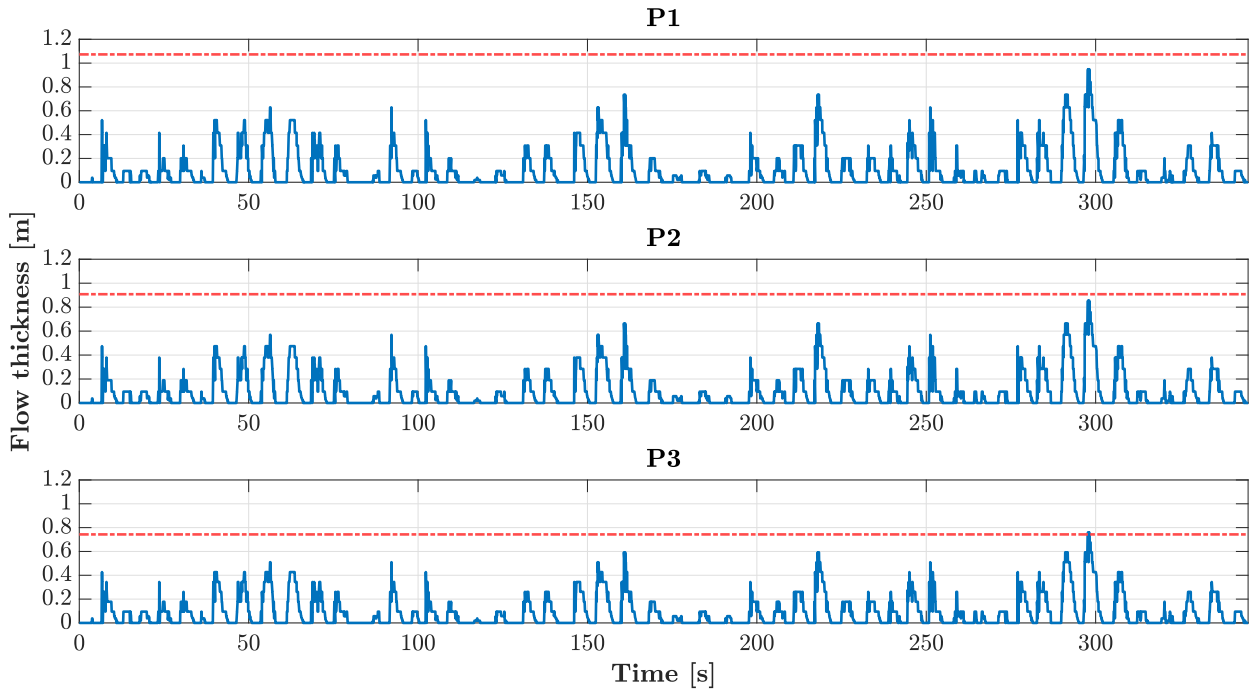


Figure B.4: Run-up flow thickness h [m] (blue solid line) and 2% run-up flow thickness $h_{A,2\%}$ (red dash-dot line) along the water side slope measured at three locations P1-P3 in Test03.

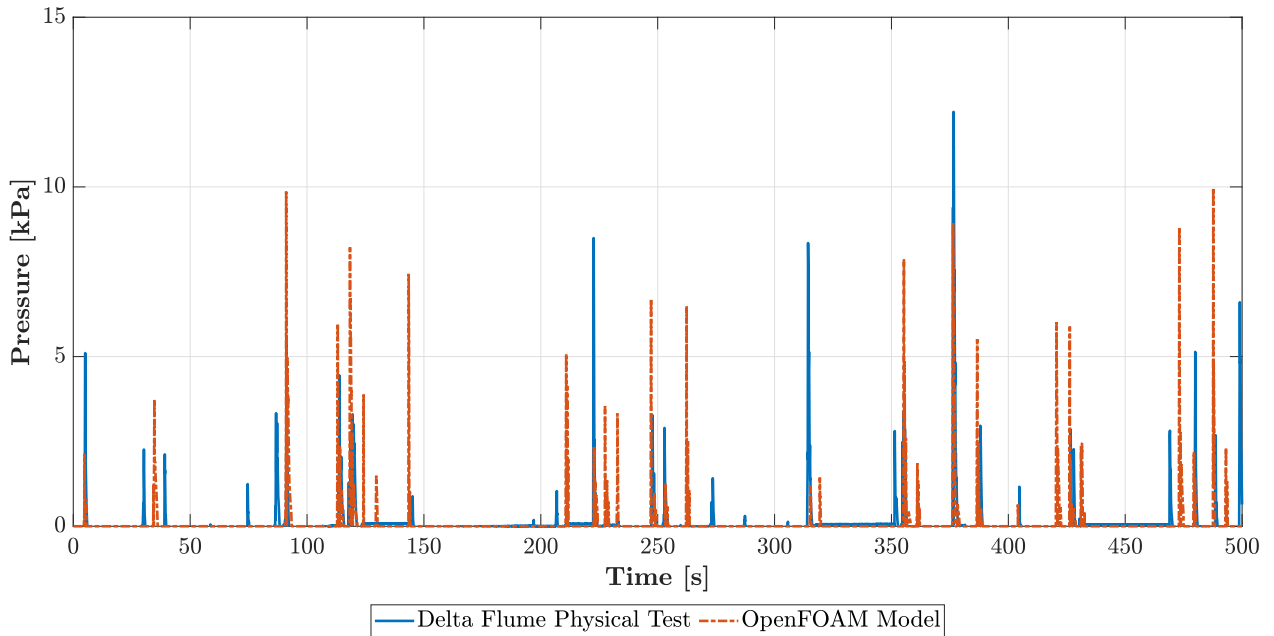


Figure B.5: Pressure on the dike crest as function of time at location of PS1 in Test01.

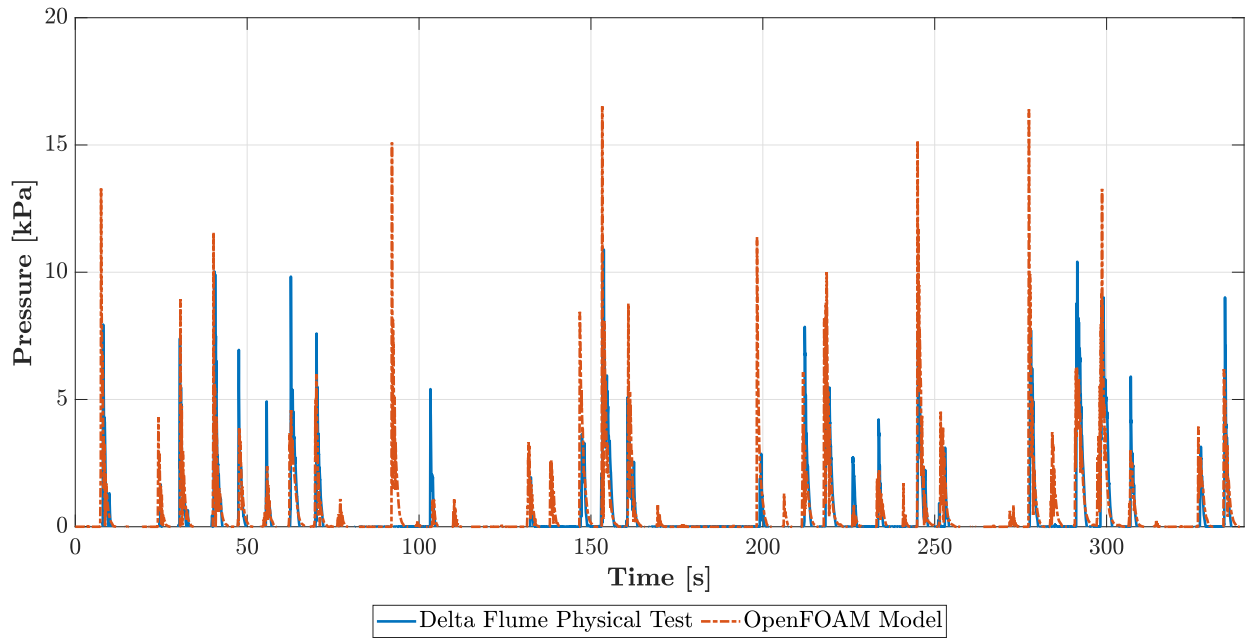


Figure B.6: Pressure on the dike crest as function of time at location of PS1 in Test03.

C | Calibration

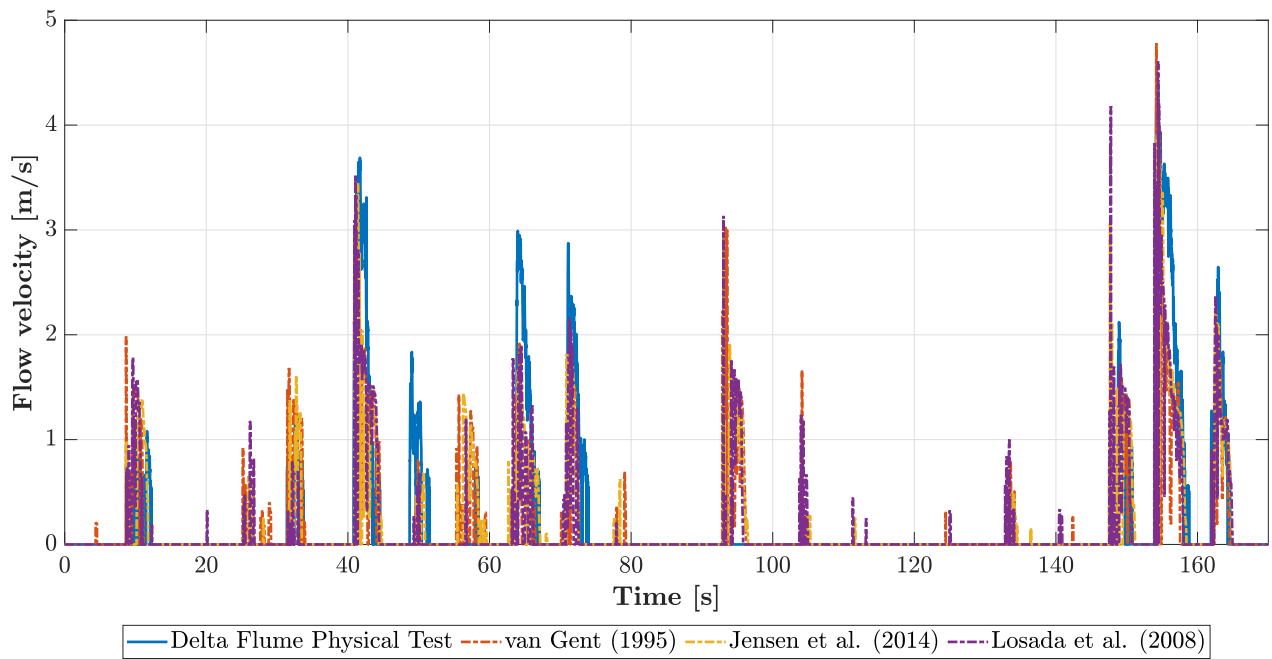


Figure C.1: Flow velocity on the landward slope at PW1 in Test03 using resistance coefficients of Van Gent (1995); Jensen et al. (2014); Losada et al. (2008).

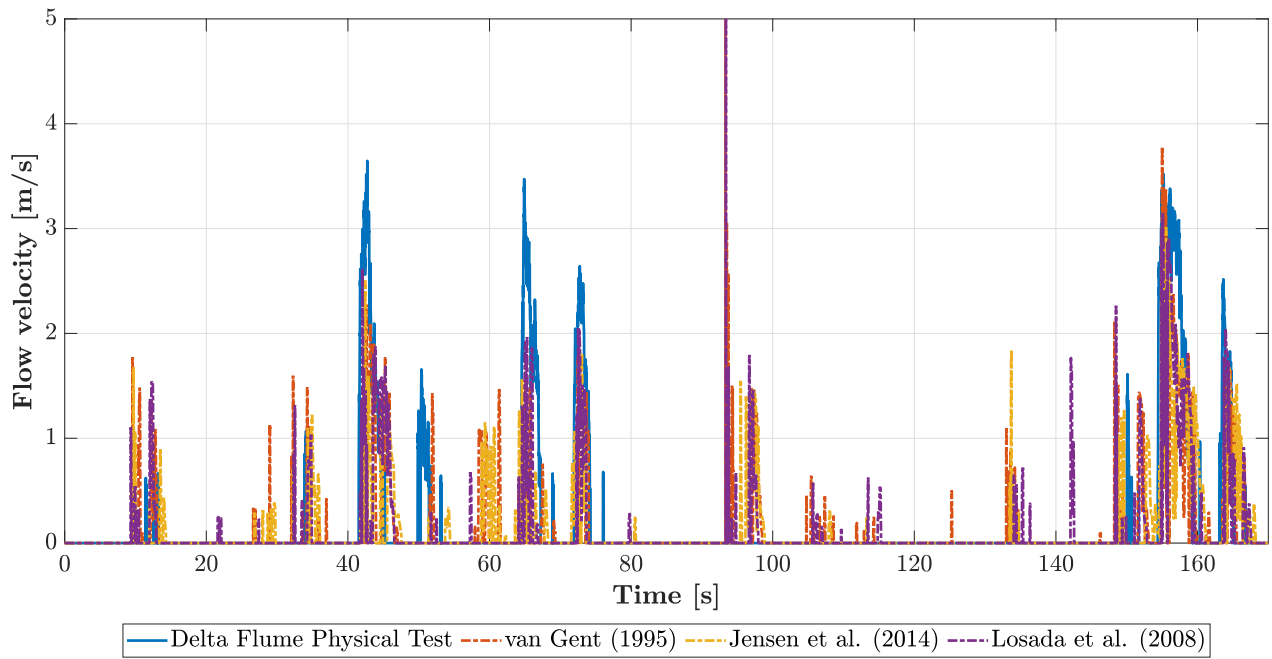


Figure C.2: Flow velocity on the landward slope at PW2 in Test03 using resistance coefficients of Van Gent (1995); Jensen et al. (2014); Losada et al. (2008).

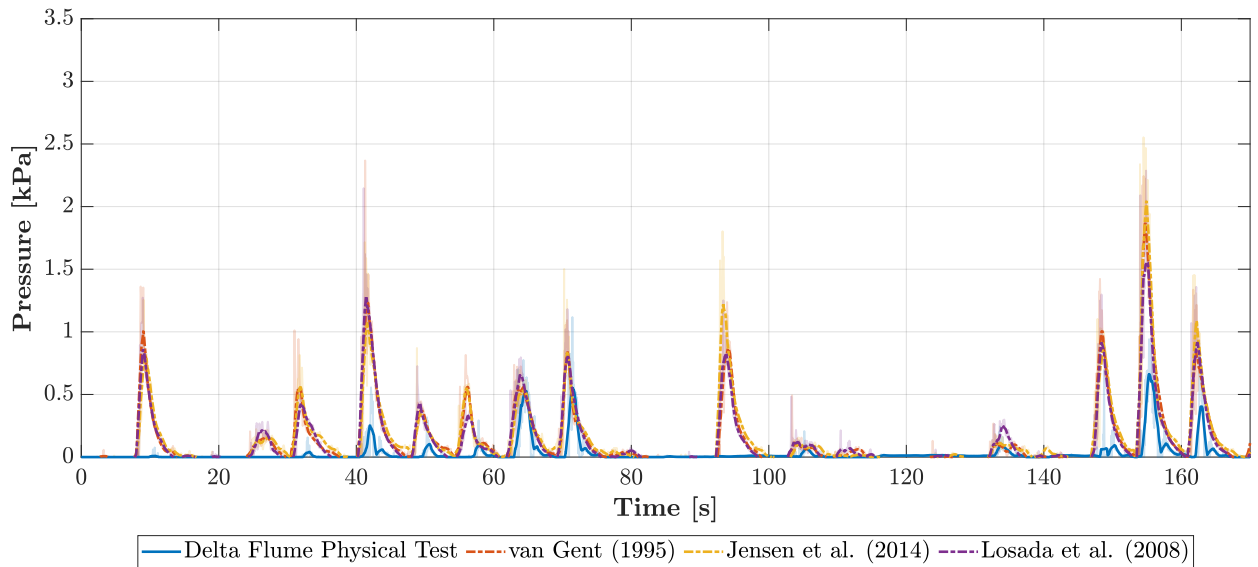


Figure C.3: Pressure on the landward slope at PS2 in Test03 using resistance coefficients of Van Gent (1995); Jensen et al. (2014); Losada et al. (2008). Data has been moving-averaged over a window of 1 s, faded lines represent the original data.

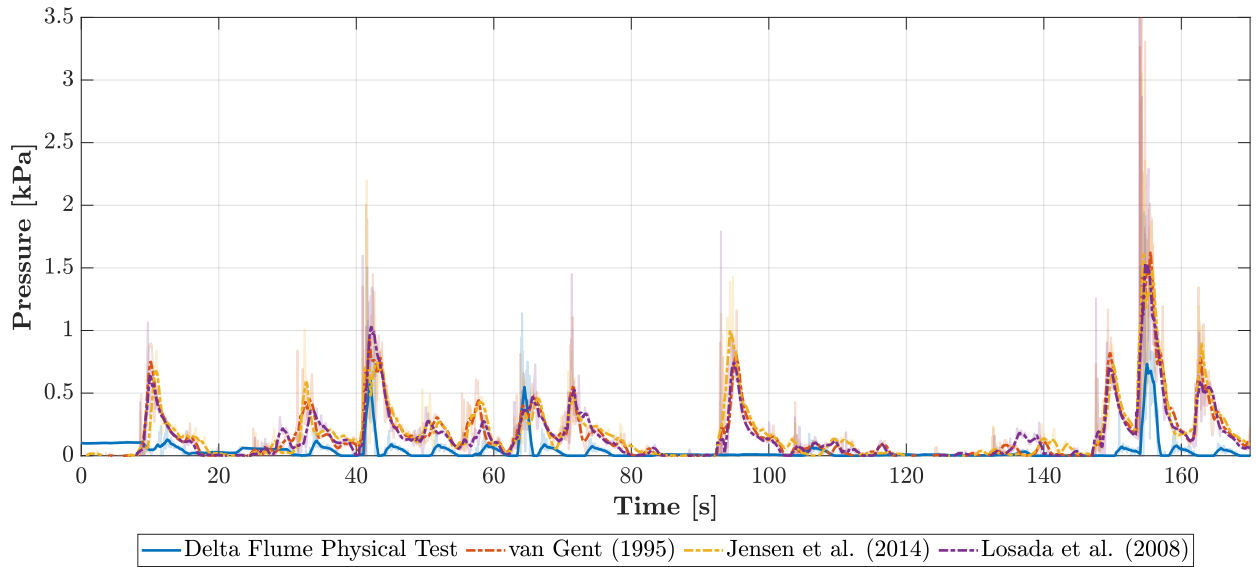


Figure C.4: Pressure on the landward slope at PS3 in Test03 using resistance coefficients of Van Gent (1995); Jensen et al. (2014); Losada et al. (2008). Data has been moving-averaged over a window of 1 s, faded lines represent the original data.

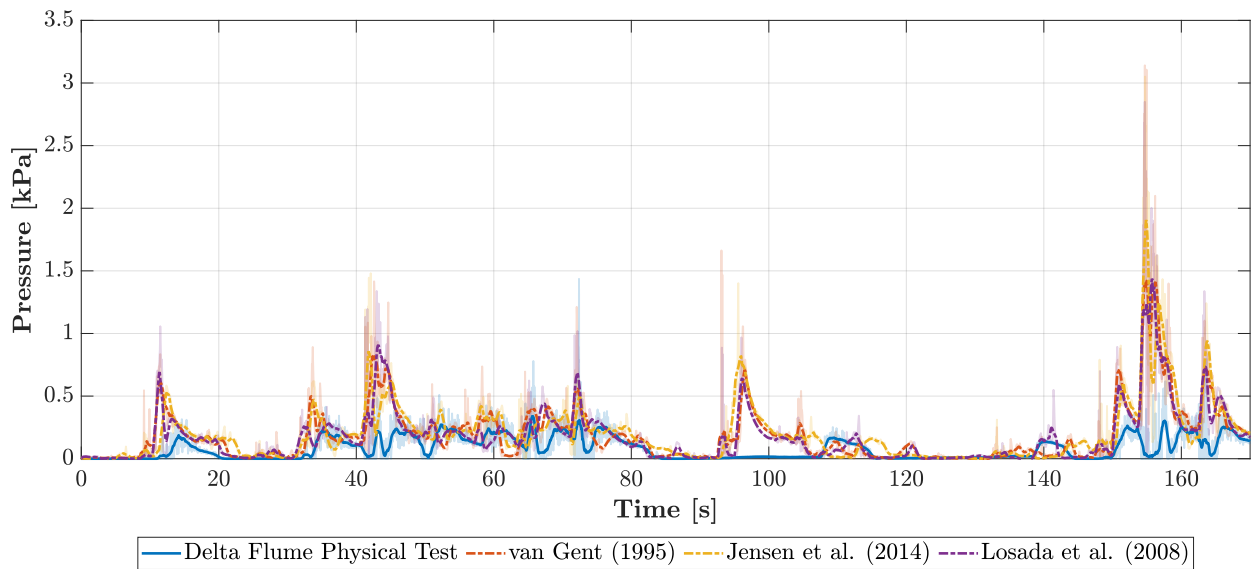


Figure C.5: Pressure on the landward slope at PS4 in Test03 using resistance coefficients of Van Gent (1995); Jensen et al. (2014); Losada et al. (2008). Data has been moving-averaged over a window of 1 s, faded lines represent the original data.

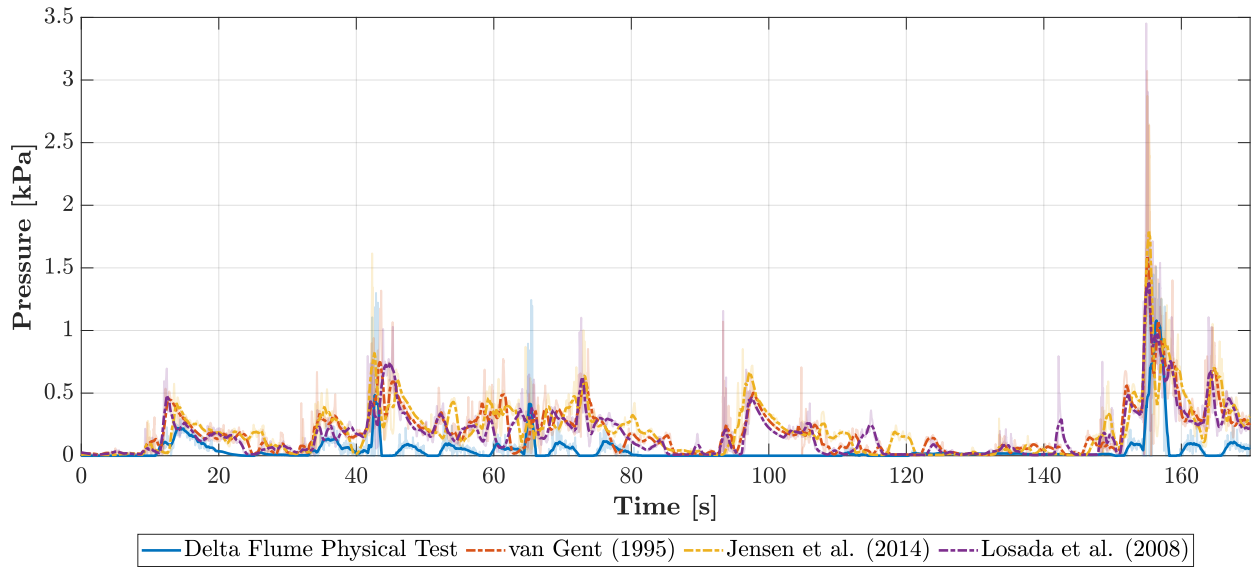


Figure C.6: Pressure on the landward slope at PS5 in Test03 using resistance coefficients of Van Gent (1995); Jensen et al. (2014); Losada et al. (2008). Data has been moving-averaged over a window of 1 s, faded lines represent the original data.

D | Validation

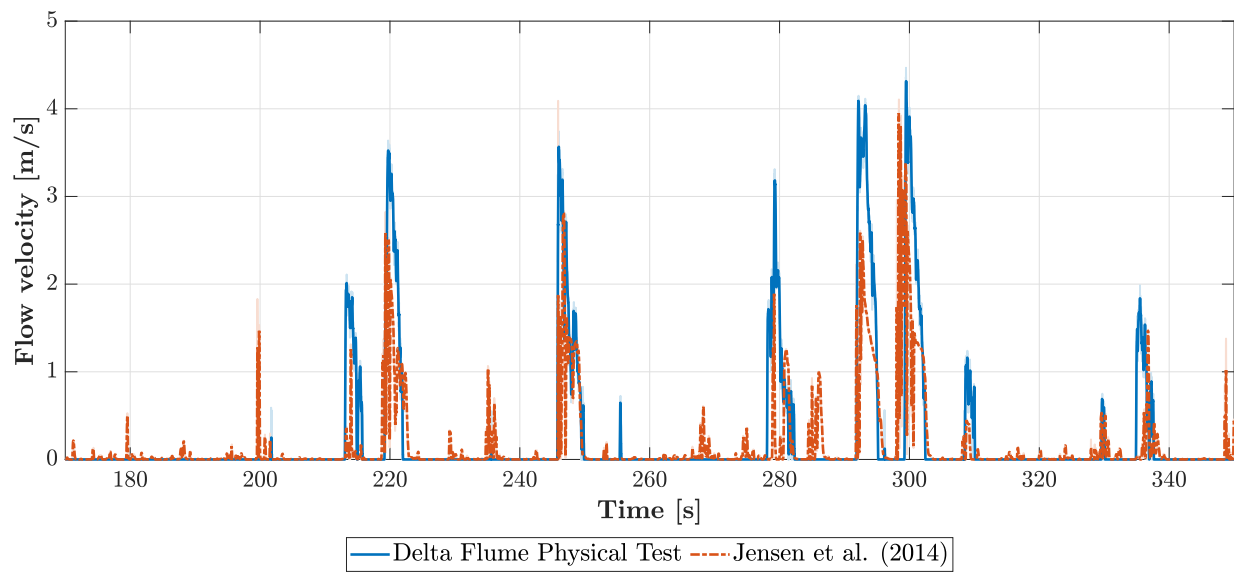


Figure D.1: Flow velocity on the landward slope at PW1 in Test03 using resistance coefficients of Jensen et al. (2014).

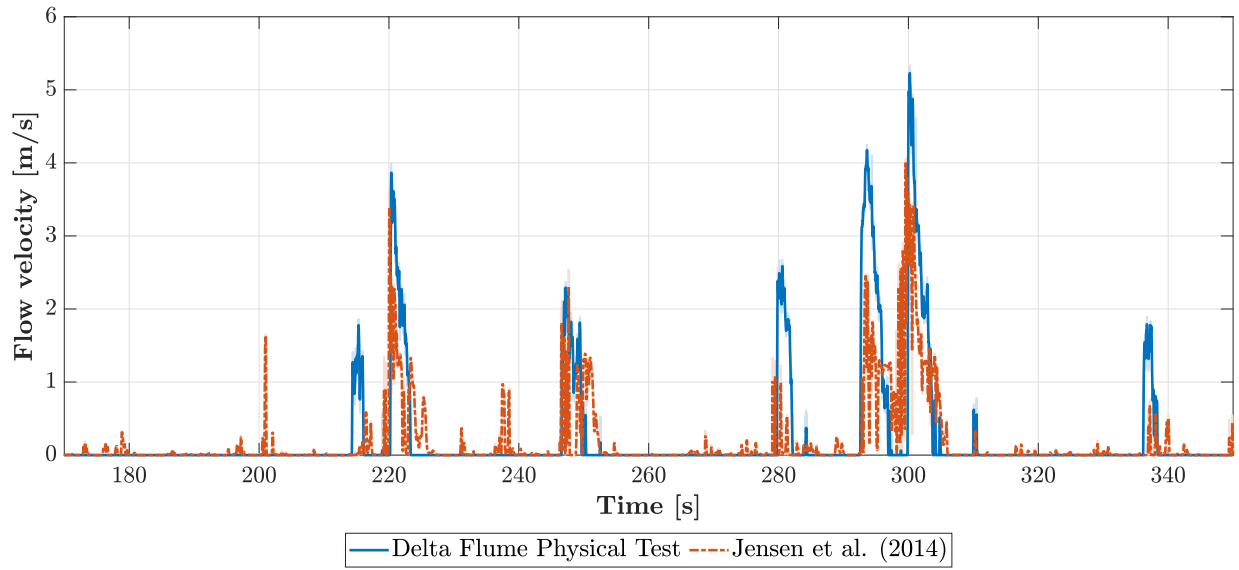


Figure D.2: Flow velocity on the landward slope at PW2 in Test03 using resistance coefficients of Jensen et al. (2014).

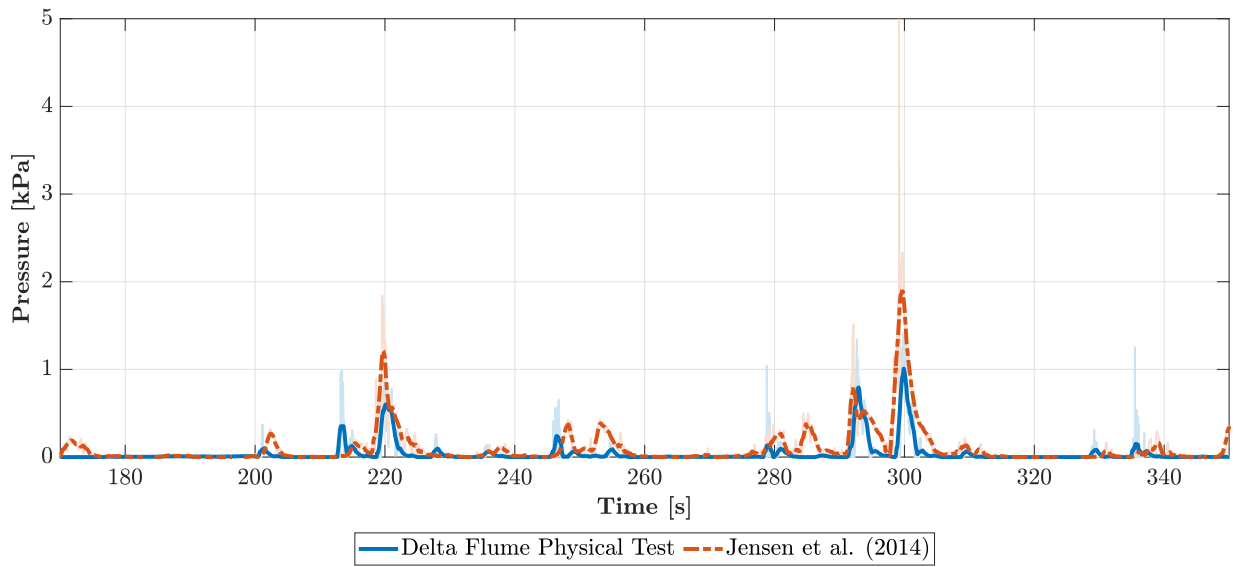


Figure D.3: Pressure on the landward slope at PS2 in Test03 using resistance coefficients of Jensen et al. (2014). Data has been moving-averaged over a window of 1 s, faded lines represent the original data.

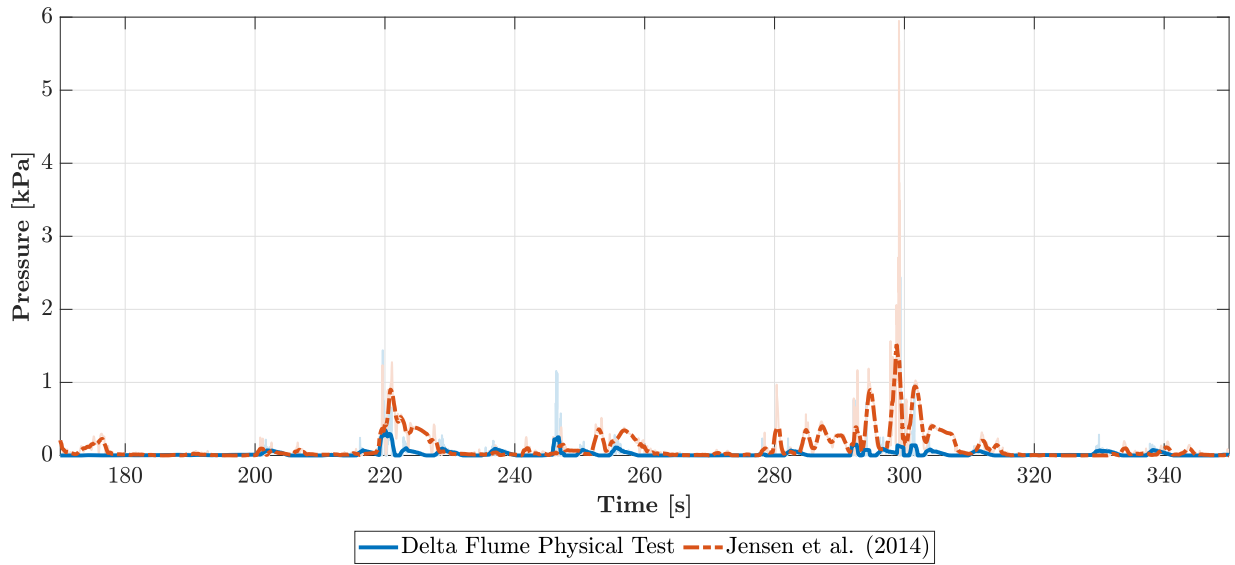


Figure D.4: Pressure on the landward slope at PS3 in Test03 using resistance coefficients of Jensen et al. (2014). Data has been moving-averaged over a window of 1 s, faded lines represent the original data.

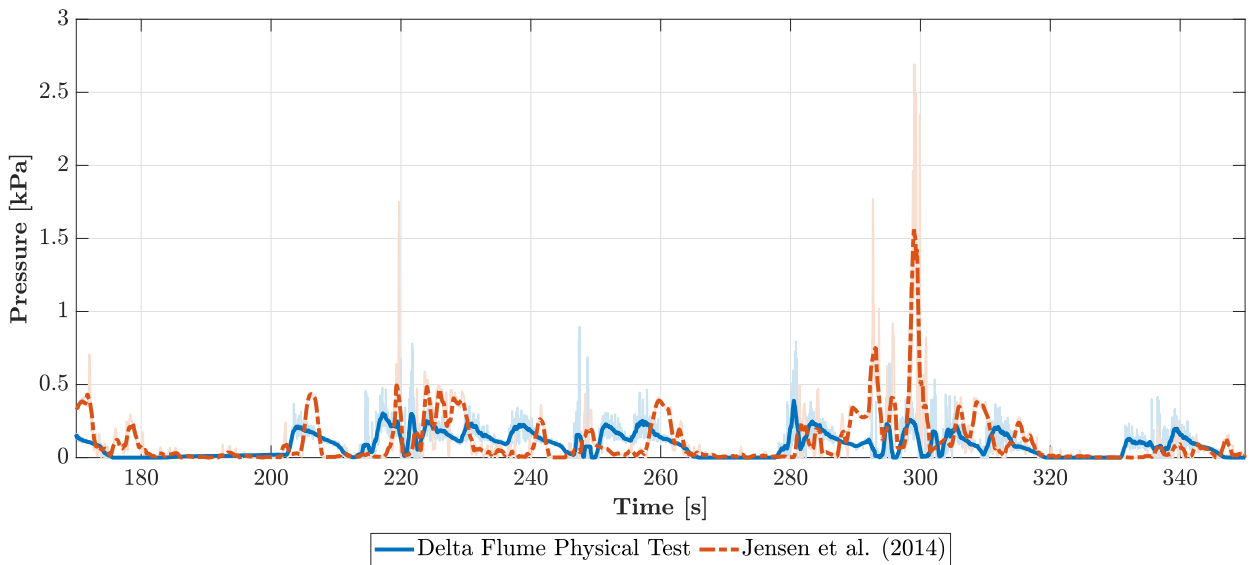


Figure D.5: Pressure on the landward slope at PS4 in Test03 using resistance coefficients of Jensen et al. (2014). Data has been moving-averaged over a window of 1 s, faded lines represent the original data.

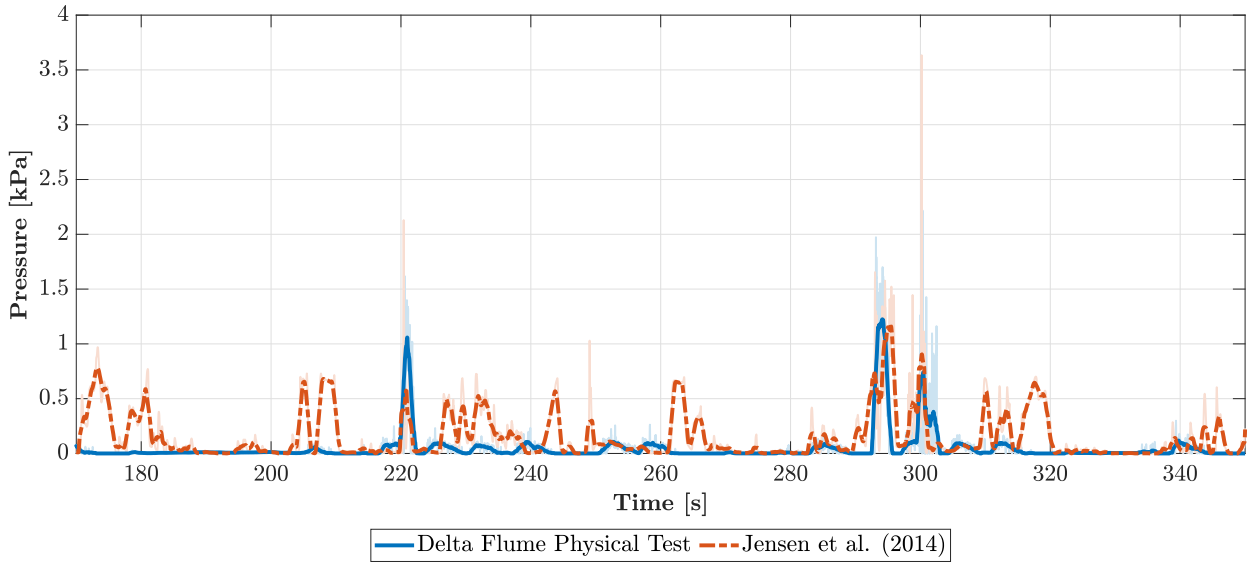


Figure D.6: Pressure on the landward slope at PS5 in Test03 using resistance coefficients of Jensen et al. (2014). Data has been moving-averaged over a window of 1 s, faded lines represent the original data.

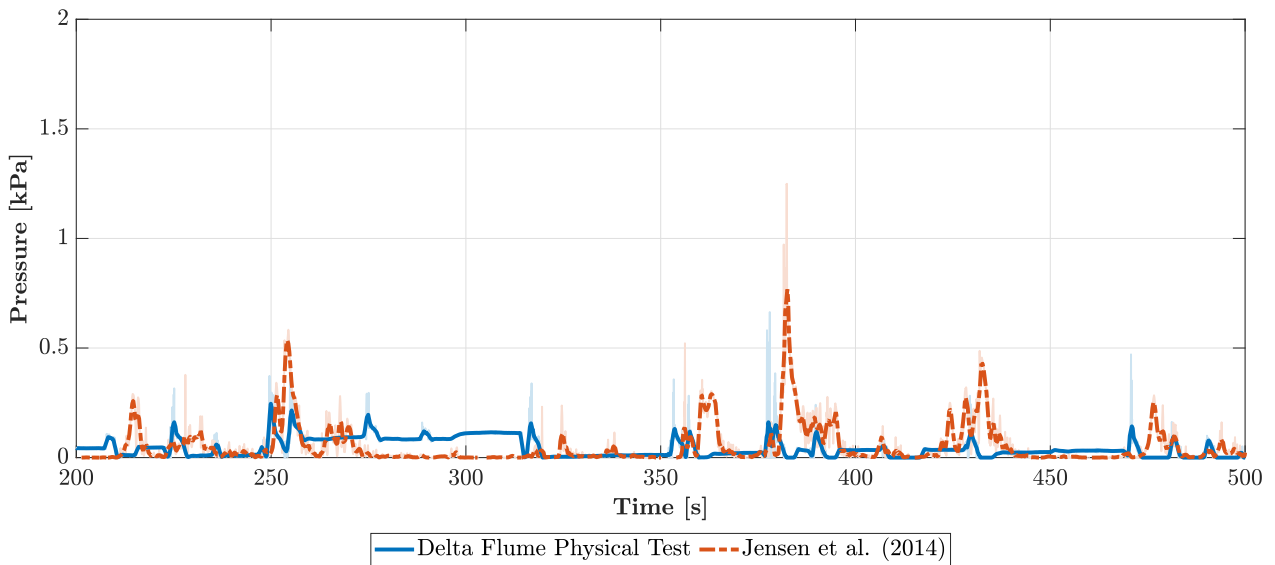


Figure D.7: Pressure on the landward slope at PS2 in Test01 using resistance coefficients of Jensen et al. (2014). Data has been moving-averaged over a window of 1 s, faded lines represent the original data.

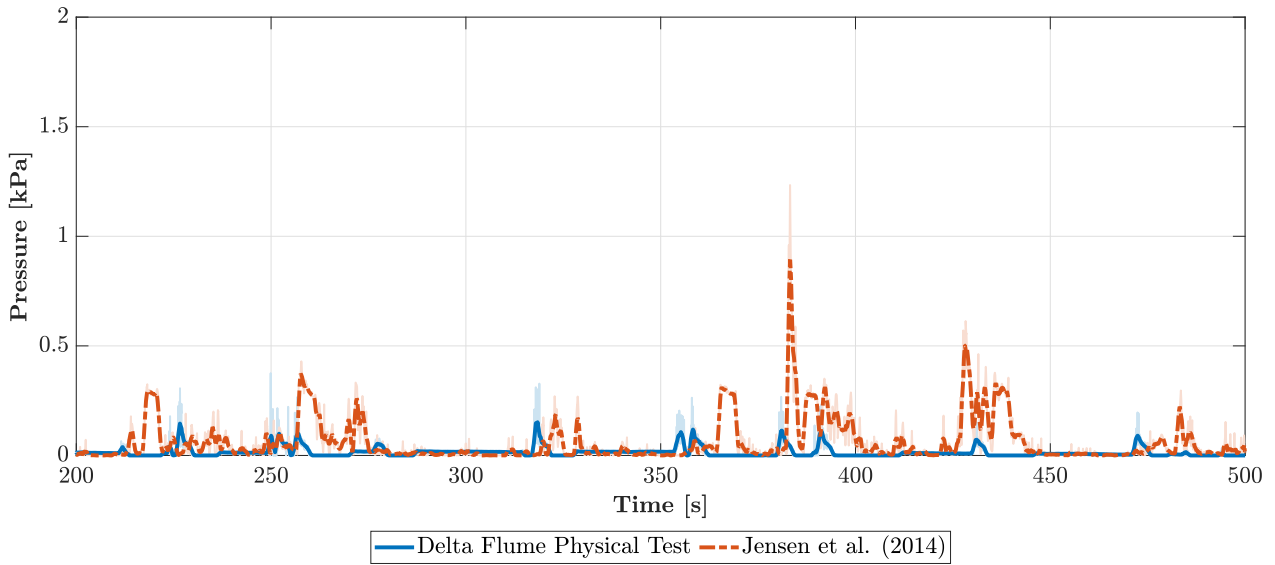


Figure D.8: Pressure on the landward slope at PS3 in Test01 using resistance coefficients of Jensen et al. (2014). Data has been moving-averaged over a window of 1 s, faded lines represent the original data.

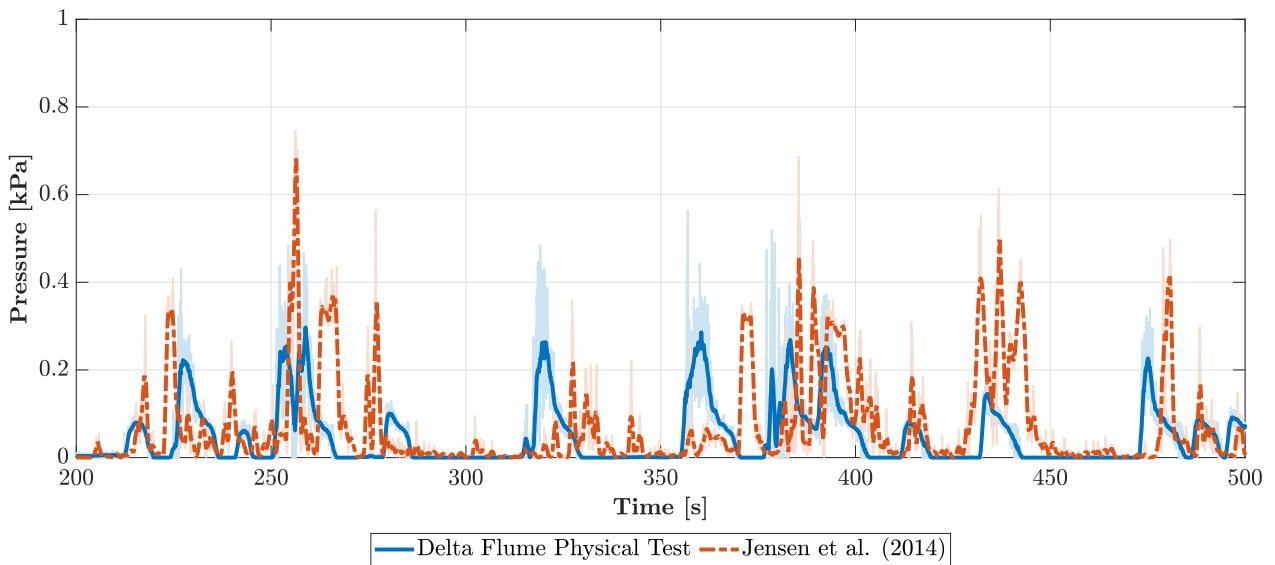


Figure D.9: Pressure on the landward slope at PS4 in Test01 using resistance coefficients of Jensen et al. (2014). Data has been moving-averaged over a window of 1 s, faded lines represent the original data.

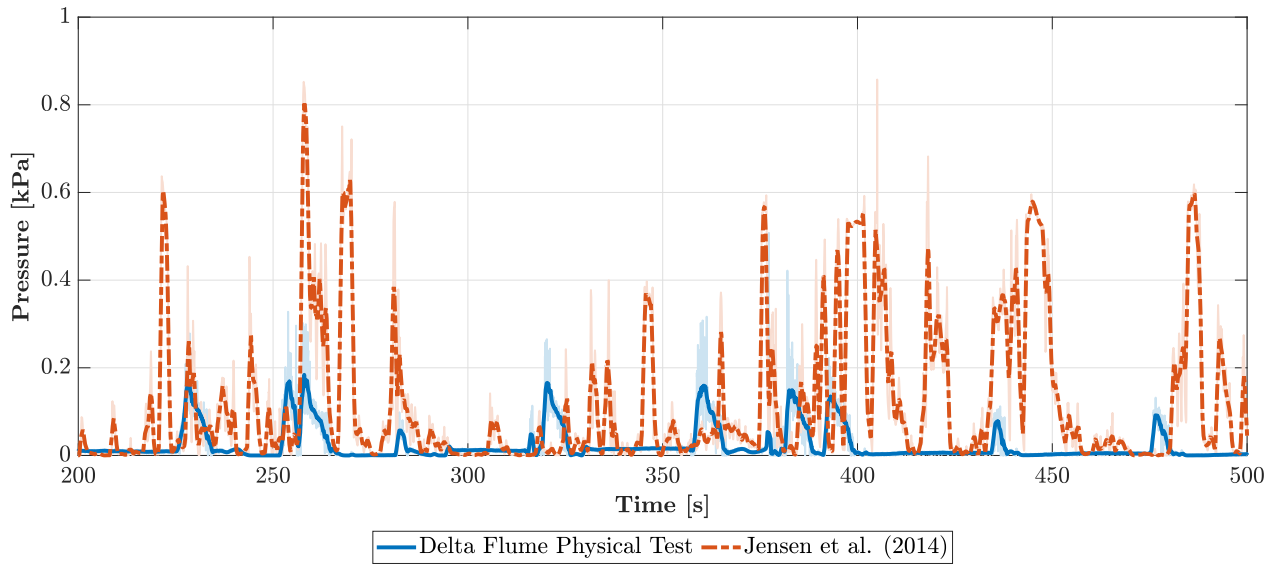


Figure D.10: Pressure on the landward slope at PS5 in Test01 using resistance coefficients of Jensen et al. (2014). Data has been moving-averaged over a window of 1 s, faded lines represent the original data.

E | Specifications of Paddle Wheel

TECHNICAL DATA



General

- Pipe Size Range: DN15 to DN600 (0,5" to 24")
Please refer to Installation Fittings section for more details
- Flow Rate Range: 0.15 to 8 m/s (0.5 to 25 ft./s)
- Linearity: $\pm 0.75\%$ of full scale
- Repeatability: $\pm 0.5\%$ of full scale
- Minimum Reynolds Number Required: 4500
- Enclosure: IP68 or IP65
- Wetted Materials:
 - sensor Body: C-PVC, PVDF or 316L SS
 - o-rings: EPDM or FPM
 - rotor: ECTFE (Halar®)
 - shaft: Ceramic (Al_2O_3)/316L SS (only for metal sensors)
 - bearings: Ceramic (Al_2O_3)

Specific for F3.00.H

- Supply voltage: 5 to 24 VDC $\pm 10\%$ regulated
- Supply current: $< 30\text{ mA @ }24\text{ VDC}$
- Output signal:
 - square wave
 - frequency: 45 Hz per m/s nominal (13.7 Hz per ft/s nominal)
 - type: transistor NPN open collector
 - output current: 10 mA max
- Cable length: 8 m (26.4 ft) standard, 300 m (990 ft) maximum

Specific for F3.00.C

- Supply voltage: 3 to 5 VDC regulated or 3.6 Volt Lithium battery
- Supply current: $< 10\ \mu\text{A max}$

Output signal:

- square wave
- frequency: 45 Hz per m/s nominal (13.7 Hz per ft/s nominal)
- min. input impedance: 100 K Ω
- Cable length: 8 m (26.4 ft) standard, 16 m (52.8 ft) maximum

Specific for F3.00.P

- Supply voltage: 12 to 24 VDC $\pm 10\%$ regulated
- Supply current: $< 30\text{ mA @ }24\text{ VDC}$
- Output signal:
 - square wave
 - frequency: 45 Hz per m/s nominal (13.7 Hz per ft/s nominal)
 - type: Push-Pull (for connection to NPN and PNP inputs)
 - output current: 20 mA max
- Cable length: 8 m (26.4 ft) standard, 300 m (990 ft) maximum

Standards & Approvals

- Manufactured under ISO 9001
- Manufactured under ISO 14001
- CE
- RoHS Compliant
- GOST R

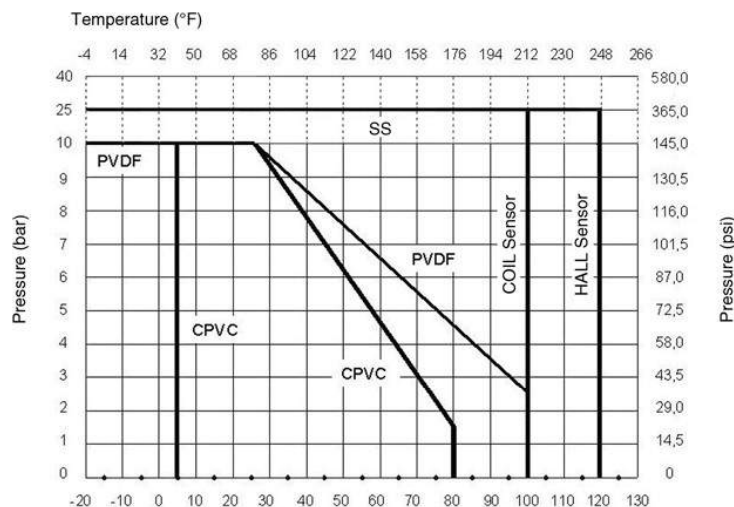
Maximum Operating Pressure / Temperature (25 years lifetime)

F3.00.H or F3.00.P Sensor

- C-PVC body:
 - 10 bar (145 psi) @ 25°C (77°F)
 - 1,5 bar (22 psi) @ 80°C (176°F)
- PVDF body:
 - 10 bar (145 psi) @ 25°C (77°F)
 - 2,5 bar (36 psi) @ 100°C (212°F)
- SS body:
 - 25 bar (363 psi) @ 120°C (248°F)

F3.00.C Sensor

- C-PVC body:
 - 10 bar (145 psi) @ 25°C (77°F)
 - 1,5 bar (22 psi) @ 80°C (176°F)
- PVDF body:
 - 10 bar (145 psi) @ 25°C (77°F)
 - 2,5 bar (36 psi) @ 100°C (212°F)
- SS body:
 - 25 bar (363 psi) @ 100°C (212°F)



F | Specifications of Pressure Sensor



MINIATURE HIGH PRESSURE PRESSURE TRANSDUCER

HKM-375 (M) SERIES

- Excellent Stability
- All Welded Construction
- Silicon on Silicon Integrated Sensor **VIS**[®]
- Robust Construction
- High Natural Frequencies
- 3/8-24 UNJF or M10 X 1 Thread
- Intrinsically Safe Applications Available (i.e. IS-HKM-375)



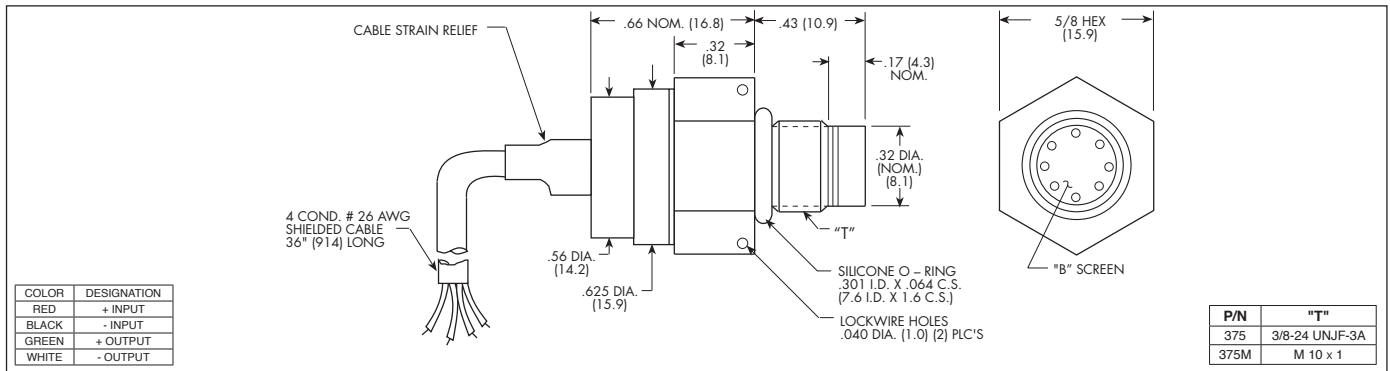
The HKM-375 is a miniature threaded pressure transducer. The hexagonal head and o-ring seal make it easy to mount and simple to apply.

The HKM-375 utilizes a flush metal diaphragm as a force collector. A solid state piezoresistive sensing element is located immediately behind this metal diaphragm which is protected by a metal screen. Force transfer is accomplished via non-compressible silicone oil. This sensing sub assembly is welded to a stainless steel body.

This advanced construction results in a highly stable, reliable and rugged instrument with all the advantages of significant miniaturization, excellent repeatability, low power consumption, etc. The miniaturization process also yields a marked increase in the natural frequencies of the transducers, making them suitable for use even in shock pressure measurements.



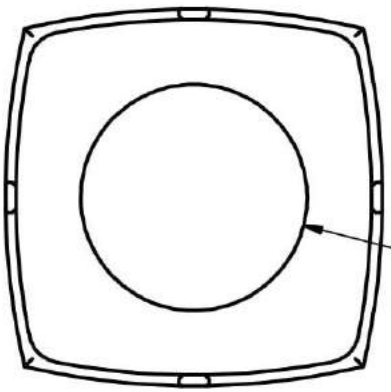
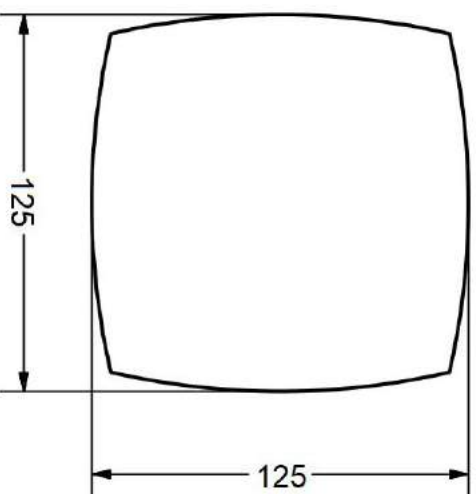
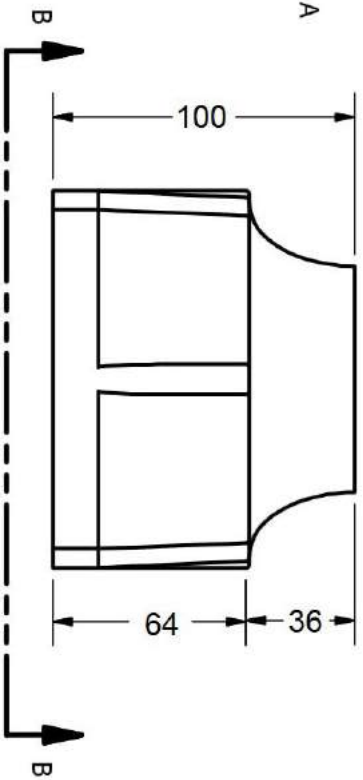
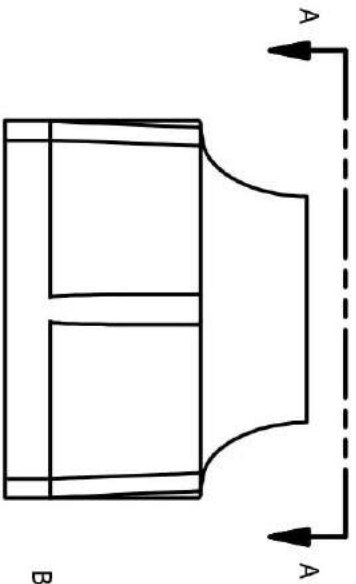
Kulite recommends the **KSC Series** of signal conditioners to maximize the measurement capability of the HKM-375 transducer.



	7 100	17 250	35 500	70 1000	170 2500	350 5000	700 10000	1400 BAR 20000 PSI
INPUT								
Pressure Range								
Operational Mode	Absolute, Sealed Gage							
Over Pressure	2 Times Rated Pressure to 1000 PSI (70 BAR) 1.5 Times Rated Pressure Above 1000 PSI to a Max. of 25000 PSI (1724 BAR)							
Burst Pressure	3 Times Rated Pressure to a Max. of 25000 PSI (1724 BAR)							
Pressure Media	Any Liquid or Gas Compatible With 15-5 PH or 316 Stainless Steel (All Media May Not Be Suitable With O-Ring Supplied)							
Rated Electrical Excitation	10 VDC/AC							
Maximum Electrical Excitation	12 VDC/AC							
Input Impedance	1000 Ohms (Min.)							
Output Impedance	1000 Ohms (Nom.)							
Full Scale Output (FSO)	100mV (Nom.)							
Residual Unbalance	± 5 mV (Typ.)							
Combined Non-Linearity, Hysteresis and Repeatability	± 0.1% FSO BFSL (Typ.), ± 0.5% FSO (Max.)							
Resolution	Infinitesimal							
Natural Frequency of Sensor Without Screen (KHz) (Typ.)	Greater Than 400 KHz							
Acceleration Sensitivity % FS/g Perpendicular	2.0x10 ⁻⁴	2.2x10 ⁻⁴	1.1x10 ⁻⁴	6.2x10 ⁻⁵	2.6x10 ⁻⁵	1.5x10 ⁻⁵	1.3x10 ⁻⁵	8.0x10 ⁻⁶
Insulation Resistance	100 Megohm Min. @ 50 VDC							
ENVIRONMENTAL								
Operating Temperature Range	-65°F to +250°F (-55°C to +120°C)							
Compensated Temperature Range	+80°F to +180°F (+25°C to +80°C) Any 100°F Range Within The Operating Range on Request							
Thermal Zero Shift	± 1% FS/100° F (Typ.)							
Thermal Sensitivity Shift	± 1% /100° F (Typ.)							
Linear Vibration	10-2,000 Hz Sine, 100g. (Max.)							
Mechanical Shock	20g half Sine Wave 11 msec. Duration							
PHYSICAL								
Electrical Connection	4 Conductor 26 AWG Shielded Cable 36" Long							
Weight	17 Grams (Max.) Excluding Cable							
Pressure Sensing Principle	Fully Active Four Arm Wheatstone Bridge Dielectrically Isolated Silicon on Silicon							
Mounting Torque	80 Inch-Pounds (Max.) 9 Nm							

Note: Custom pressure ranges, accuracies and mechanical configurations available. Dimensions are in inches. Dimensions in parenthesis are in millimeters. All dimensions nominal. (Q) Continuous development and refinement of our products may result in specification changes without notice. Copyright © 2014 Kulite Semiconductor Products, Inc. All Rights Reserved. Kulite miniature pressure transducers are intended for use in test and research and development programs and are not necessarily designed to be used in production applications. For products designed to be used in production programs, please consult the factory.

G | Dimensions of scaled Grassblock

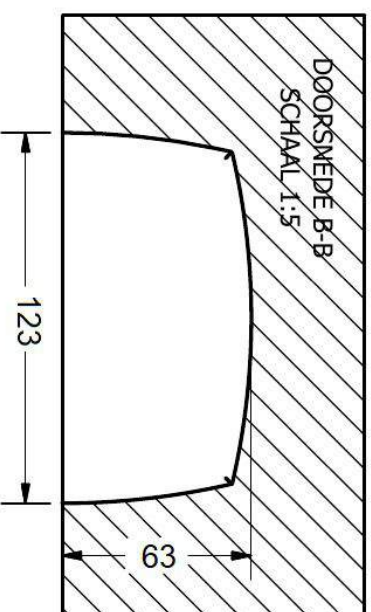
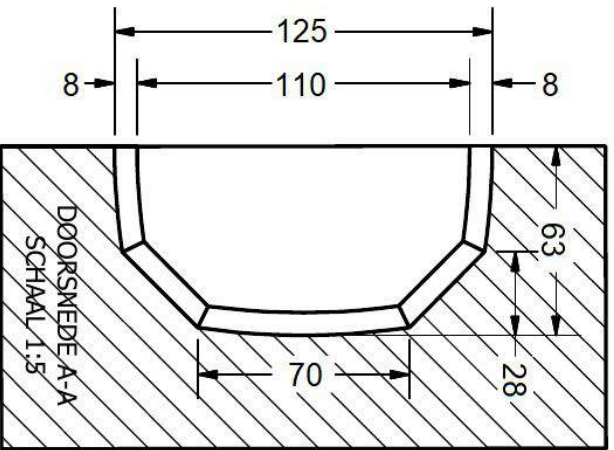
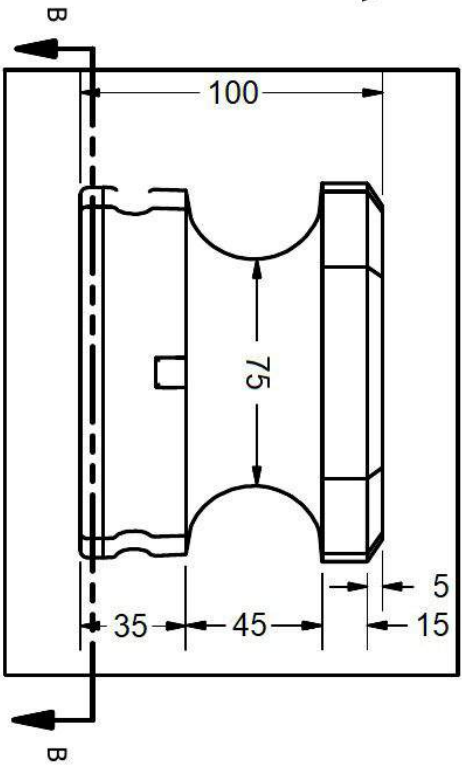
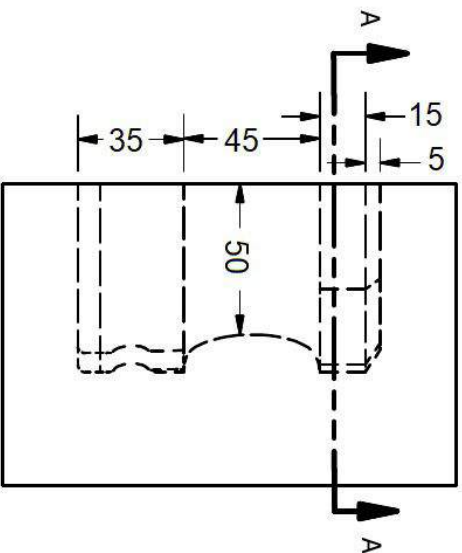


VIEW A-A
SCALE 1:5

VIEW B-B
SCALE 1:5

GETEKEND	AM	29-10-2015	Hillblock BV		
CONTROLÉ					
GOEDGEKEURD			Grassblock 200		
STATUS					
Voorlopig			MODEL		
			AFM	TEK NR.	REV
			A4	Grassblock 200 V7.0	
			SCHAAL 1:5	MATEN IN MM	BLAD 1 VAN 1

H | Dimensions of scaled Hillblock 2.0



GETEKEND		07-Nov-17		Hillblock BV	
AM					
CONTROLE					
GOEDGEKEURD		10-Nov-17		Hillblock 200	
MODEL					
AFM					
SCHAAL 1:5		MATEN IN MM		BLAD 1 VAN 1	
A4		TEK NR.		REV	
Hillblock 200 (maj) V2.0A 10-11-2017				A	

I | Specifications of Geotextile



Certificaat: 0338-CPD-689

test	test methode	eenheid	Geopex NW 270 (S22NW) Type 1	Tolerantie
Materiaal			genaaldrukt/ thermisch gebonden PP vlies	
Gewicht (Areeke massa)	EN-985	gram per m ²	270	±20
Dikte (2 kN/m ²)			1,8	0,3
Treksterkte machinerichting	EN-ISO 10319	kN/m ¹	22	±2,5
dwarsrichting		kN/m ¹	22	±2,5
Rek bij breuk machinerichting		%	55	±10
dwarsrichting		%	55	±10
C.B.R. Test				
Doordrukkracht	EN-ISO 12238	kN	3,8	±0,4
Kegelvalproef				
gatdiameter	EN 918	mm	16	±4
Zanddichtheid				
Ø 90 (natte zeefest)	EN ISO 12 956	mu	0,07	±10
Waterdoorlaatbaarheid				
V-Index (20°C)	EN ISO 11 058	m/s	0,07	
debiet bij 5 cm waterkolom		l/m ² .sec	70	±20
Permittiviteit		sec ⁻¹	1,4	
Weerstand tegen verouderen	ENV 13438		Verwachte levensduur > 50 jaar in natuurlijke grond met 4 < pH < 9 pH en een grondtemperatuur van < 25°C	
De reststerkte (RV) na 56 dagen beproeving in % van de aanvangsterkte.	ENV 13438	%	> 90	
Low Leach stabilisatoren			Hals stabilisatoren	
Rollbreedte		cm	540	
Rollengte		m	100	

Toepassing en gebruik niet geweven geotextielen



EN 13249	EN 13250	EN 13251	EN 13252	EN 13253	EN 13254	EN 13255	EN 13257	EN 13265
F	F	F	F	F	F	F	F	F
R	R	R	D	R	R	R	R	R
F+S	F+R							
R+S	R+S	R+S	F+D	R+S	R+S	R+S	R+S	
F+R	F+R	F+R	F+S+D	F+R	F+R	F+R	F+R	
F+R+S	F+R+S	F+R+S		F+R+S	F+R+S	F+R+S	F+R+S	

Alle Geopex PP geotextielen worden extern gecontroleerd en dragen het CE keurmerk.
De productie van de Geopex NW geotextielen is gecertificeerd volgens ISO 9001:2000.
Bovengenoemde waarden zijn gemiddelde waarden, verkregen met behulp van standaard testmethoden



GEOPEX PRODUCTS (EUROPE) B.V.

Postbus 20, 2830 AA GOUDERAK
Middelblok 164, 2831 BR GOUDERAK
Tel: (0182) 377 327
Fax: (0182) 377 329
E-mail: europe@geopex.com
Internet: www.geopex.com

Geotextiel	1220668	
	Deltares	Fig. B.4